

Aus dem Josef Lissner Laboratory for Biomedical Imaging
des Instituts für Klinische Radiologie
der Ludwig-Maximilians-Universität München

Direktor: Prof. Dr. med Dr. h.c. Maximilian F. Reiser, FACR, FRCR

Voxel-based assessment of disease progression in
articular cartilage with MRI follow-up examinations
of the T_2 relaxation time

Dissertation zum Erwerb des Doktorgrades der Humanbiologie an der Medizinischen
Fakultät der Ludwig-Maximilians-Universität zu München

vorgelegt von
José María Raya García del Olmo
aus
Sevilla (Spanien)

2009

Mit Genehmigung der Medizinischen Fakultät der Universität München

Berichterstatter: Prof. Dr. med. Dr. h.c. Maximilian F. Reiser, FACR, FRCR
Prof. Dr. med. Dipl. Ing. Volkmar Jansson

Mitberichterstatter: Prof. Dr. med. Claus Belkar
Priv.-Doz. Dr. med. Reinhold Tiling

Mitbetreuung durch die promovierten Mitarbeiter: Prof. Dr. med. Dr. h.c. Maximilian F. Reiser, FACR, FRCR
Priv.-Doz. Dr. med. Christian Glaser
Dr. rer. nat. Olaf Dietrich

Dekan: Prof. Dr. med. Dr. h.c. Maximilian F. Reiser, FACR, FRCR

Tag der mündlichen Prüfung: 07.10.2009

Contents

| | |
|--|-----------|
| Zusammenfassung | 1 |
| 1 Introduction | 5 |
| 2 Anatomy and physiology of the articular cartilage | 9 |
| 2.1 Anatomy | 9 |
| 2.1.1 Composition | 10 |
| 2.1.2 Structure | 12 |
| 2.2 Physiology | 14 |
| 2.3 Osteoarthritis | 17 |
| 2.3.1 Pathogenesis | 17 |
| 2.3.2 Risk factors | 18 |
| 2.3.3 Diagnosis | 18 |
| 2.3.4 Prevalence and incidence | 19 |
| 2.3.5 Therapy | 20 |
| 2.3.6 Socio-economical aspects of OA | 20 |
| 3 MRI of articular cartilage | 21 |
| 3.1 MRI of the proteoglycans | 21 |
| 3.1.1 Sodium MRI | 22 |
| 3.1.2 Delayed Gadolinium enhanced MRI of the cartilage (dGEMRIC) | 23 |
| 3.1.3 $T_{1\rho}$ imaging | 24 |
| 3.2 MRI of the collagen network | 26 |
| 3.2.1 T_2 relaxation time | 26 |
| 3.3 MRI methods sensitive to proteoglycan and collagen | 32 |
| 3.3.1 Quantitative measurements of cartilage morphology | 32 |
| 3.3.2 Diffusion tensor imaging (DTI) | 34 |
| 3.4 Emerging techniques | 36 |
| 3.4.1 Ultra-short echo time MRI | 36 |
| 3.4.2 gagCEST MRI | 36 |
| 4 T_2 calculation in conditions of low SNR | 39 |
| 4.1 Theory | 40 |

| | | |
|----------|--|-----------|
| 4.2 | Methods | 42 |
| 4.2.1 | MRI measurement protocol | 42 |
| 4.2.2 | Calculation of the T_2 relaxation time | 42 |
| 4.2.3 | Calculation of the SNR | 43 |
| 4.2.4 | Numerical simulations | 43 |
| 4.2.5 | Accuracy and precision | 43 |
| 4.2.6 | Phantom measurements | 44 |
| 4.2.7 | In vivo measurements | 45 |
| 4.3 | Results | 45 |
| 4.3.1 | Numerical simulations | 45 |
| 4.3.2 | Phantom measurements | 47 |
| 4.3.3 | In vivo measurements | 48 |
| 4.4 | Discussion | 49 |
| 4.4.1 | The ft methods | 50 |
| 4.4.2 | Numerical simulations | 53 |
| 4.4.3 | Phantom measurements | 54 |
| 4.4.4 | In vivo measurements | 56 |
| 4.5 | Conclusions | 57 |
| 5 | Voxel based reproducibility of T_2 with a new registration algorithm | 59 |
| 5.1 | Theory | 59 |
| 5.1.1 | Transformation Model | 59 |
| 5.1.2 | Measure of alignment | 60 |
| 5.1.3 | Optimization method | 60 |
| 5.1.4 | Comparison of registered datasets | 61 |
| 5.2 | Methods | 61 |
| 5.2.1 | Numerical simulations | 61 |
| 5.2.2 | In vitro measurement | 62 |
| 5.2.3 | In vivo measurements | 63 |
| 5.3 | Results | 64 |
| 5.3.1 | Numerical simulations | 64 |
| 5.3.2 | Role of the overlap volume | 65 |
| 5.3.3 | In vitro measurements | 66 |
| 5.3.4 | In vivo measurements | 66 |
| 5.4 | Discussion | 68 |
| 5.4.1 | The registration algorithm | 68 |
| 5.4.2 | Validation of the registration algorithm | 70 |
| 5.4.3 | Reproducibility of cartilage T_2 | 71 |
| 5.5 | Further applications of the registration algorithm | 73 |
| 5.5.1 | Reproducibility of cartilage thickness | 73 |
| 5.5.2 | Cartilage deformation after exercise | 74 |
| 5.5.3 | Interindividual model using clustering | 75 |
| 5.6 | Conclusion | 76 |

| | | |
|----------|---|------------|
| 6 | Application to disease monitoring | 79 |
| 6.1 | Methods | 80 |
| 6.1.1 | MRI measurement protocol | 80 |
| 6.1.2 | Volunteers | 80 |
| 6.1.3 | Calculation of the T_2 errors | 80 |
| 6.1.4 | 2σ -significance map | 81 |
| 6.1.5 | Evaluation in MACT patients | 81 |
| 6.2 | Results | 83 |
| 6.2.1 | Calculation of the T_2 errors | 83 |
| 6.2.2 | 2σ -significance chart | 84 |
| 6.2.3 | Evaluation on MACT patients | 84 |
| 6.3 | Discussion | 86 |
| 6.3.1 | Calculation of the T_2 errors | 86 |
| 6.3.2 | 2σ -significance chart | 88 |
| 6.3.3 | Evaluation on MACT | 89 |
| 6.4 | Conclusion | 91 |
| 7 | Conclusions | 93 |
| A | Cramér-Rao lower bound (CRLB) | 95 |
| B | Noise-corrected exponential for images acquired with multi-channel coils | 97 |
| C | Derivation of the theoretical 2σ-significance chart | 99 |
| | Bibliography | 119 |
| | Index of Notation | 121 |
| | Acknowledgments | 125 |

List of Figures

| | | |
|-----|---|----|
| 2.1 | Anatomy of the knee | 9 |
| 2.2 | Water content map measured at 17.6 T | 10 |
| 2.3 | Collagen zonal architecture | 14 |
| 2.4 | Safranin-O stained histological cuts | 15 |
| 2.5 | Example of examination of the articular cartilage at 17.6 T under indentation | 16 |
| 2.6 | Prevalence of knee OA | 19 |
| 3.1 | Example of Na maps | 23 |
| 3.2 | Follow-up dGEMRIC examinations of a patient with a posterior cruciate ligament tear | 24 |
| 3.3 | Example of $T_{1\rho}$ maps | 26 |
| 3.4 | Sequence diagram of a MSME sequence | 29 |
| 3.5 | Example of T_2 follow-up examinations of a MACT patient | 31 |
| 3.6 | Example of ADC and FA on a healthy sample | 35 |
| 3.7 | Example of an UTE image of the patellar cartilage | 37 |
| 4.1 | Example of the noise-free and noise-corrected exponentials | 42 |
| 4.2 | Example of simulated, phantom and in vivo MR images | 46 |
| 4.3 | Accuracy and precision of the T_2 values in simulated MR data | 47 |
| 4.4 | Examples of T_2 maps of phantom measurements | 49 |
| 4.5 | Accuracy and precision of the T_2 values in phantom measurements | 50 |
| 4.6 | Example of in vivo T_2 maps showing the differences of the four fit methods | 51 |
| 4.7 | Relative accuracy and precision of the T_2 values in vivo | 52 |
| 4.8 | Accuracy and precision of the three-parameter method | 54 |
| 5.1 | Distribution of the registration errors | 65 |
| 5.2 | T_2 profiles from the BCI to the AS of all volunteers | 66 |
| 5.3 | Regional mean CV of T_2 reproducibility | 68 |
| 5.4 | Regional distribution of the voxel-based reproducibility of T_2 | 69 |
| 5.5 | Regional distribution of the voxel-based reproducibility of thickness | 74 |
| 5.6 | Example of depression areas in one volunteer after squall | 76 |
| 5.7 | Interindividual model of the cartilage based on T_2 | 77 |
| 6.1 | Construction of the 2σ -significance map | 82 |
| 6.2 | Histogram of T_2 values in healthy and OA-diseased volunteers | 83 |

| | | |
|-----|---|----|
| 6.3 | Measured and theoretical T_2 error | 84 |
| 6.4 | Calculated 2σ -significance chart | 85 |
| 6.5 | Example of the 2σ -significance chart | 86 |
| 6.6 | 2σ -significance map of an ACT patient | 87 |
| 6.7 | Follow-up T_2 changes in ACT patients | 89 |
| 6.8 | Number of chondrocytes versus the cumulative ΔT_2 | 90 |

List of Tables

| | | |
|-----|---|----|
| 3.1 | Summary of the MRI methods for the knee | 22 |
| 4.1 | Gd-DTPA concentration, true T_2 times and SNR_0 values for the phantoms. | 44 |
| 4.2 | Accuracy and precision for different T_2 and SNR_0 values. | 48 |
| 4.3 | Relative errors in σ_{T_2} for different sample sizes | 56 |
| 5.1 | Mean and maximum registration errors | 64 |
| 5.2 | Overlap volume before and after registration of in vivo images | 67 |
| 6.1 | Regions in the 2σ -significance chart | 83 |
| 6.2 | Summary of the results of the IKDC form and histology | 86 |
| 6.3 | Summary of the T_2 changes in ACT patients | 88 |

Zusammenfassung

Arthrose (OA) ist eine degenerative, schmerzhafte und funktionell einschränkende Gelenkserkrankung, in deren Verlauf ein progressiver Verlust des Gelenkknorpels, Eburnation der subchondralen Knochen und Entzündungen der Gelenkkapsel auftreten. Durch die hohe Inzidenz und das Fehlen einer effektiven Therapie stellt OA eine große sozioökonomische Last in den meisten Industrieländern dar (Kapitel 2). Eine beträchtliche Einschränkung bei der Beurteilung neuer Therapien und Medikamente gegen OA ist das Fehlen einer robusten nichtinvasiven Methode zur Evaluation des Krankheitsverlaufs.

Da degenerative Veränderungen in der Kollagenmatrix als Ausgangspunkt irreversibler Gelenkschädigungen angesehen werden, stellt der Gelenkknorpel eine sehr wichtige Entität für die frühzeitige Diagnose von OA dar. In den letzten Jahrzehnten war es der Gegenstand intensiver Forschungen MRI-Methoden zur nichtinvasiven Darstellung der Integrität der extrazellulären Knorpelmatrix zu entwickeln (ein detaillierter Überblick findet sich in Kapitel 3). Die Relaxationszeit T_2 ist, neben anderen quantitativen MRI-Parametern, besonders zur Diagnose von OA geeignet, weil sie der einzige leicht zugängliche MR-Parameter ist, der hauptsächlich von der Struktur der Kollagenmatrix abhängig ist.

Obwohl in der Vergangenheit bereits gezeigt wurde, dass T_2 sensitiv auf den Abbau des Gelenkknorpels ist [Dardzinski97, Mosher00, Mosher04b], hat sich die T_2 -Messung in der klinischen Routine noch nicht etabliert. Das liegt zum einen an den langen Akquisitionszeiten und der Notwendigkeit der Bildnachverarbeitung, zum anderen aber auch an Schwierigkeiten bei der Interpretation der T_2 -Maps. Wie in Figur 6.2 gezeigt, ist die Verteilung von T_2 in gesunden und OA-erkrankten Probanden sehr ähnlich, so dass globale Werte wie der Mittelwert oder die Standardabweichung von T_2 weder sensitiv noch spezifisch zwischen gesundem und bereits erkranktem Knorpel unterscheiden können. Nur in Anwesenheit einer fokalen Lesion mit hohen T_2 -Werten kann eine T_2 -Map leicht interpretiert werden; tatsächlich wurde gezeigt, dass quantitative T_2 -Maps eine höhere Sensitivität für die Identifizierung fokaler Läsionen aufweisen als das Standard-MRI-Protokoll [Hannila07].

T_2 hat ein großes Potential für den Vergleich sukzessiver Untersuchungen, das mangels geeigneter Vergleichsmethoden bis jetzt weitgehend ungenutzt bleibt. In T_2 Langzeitstudien wurden bisher T_2 -Werte, die entweder über den ganzen Gelenkknorpel [Blumenkrantz04, Stahl07] oder über eine auf einer Läsion definierten ROI [Trattinig07a, Welsch08a, Domayer09, Welsch09] gemittelt wurden, für die Evaluierung des Krankheitsverlaufs benutzt. Zwar ist der Mittelwert von T_2 leicht zu berechnen, hat aber den Nachteil, dass er nur eine grobe Abschätzung bietet und nicht sehr sensitiv auf etwaige Veränderungen im Knorpel reagiert. Zudem verwirft man durch die Mittelung wertvolle Informationen über Vorgänge, die sich auf einer kleineren Skala abspielen.

Die ideale Methode zur Auswertung von Nachfolgeuntersuchungen sollte in der Lage sein, Verän-

Zusammenfassung

derungen auf der kleinstmöglichen Längenskala (d.h. auf Voxelbasis) nachzuweisen. Die Entwicklung einer solchen Methode erfordert eine akkurate Berechnung der T_2 -Werte in jedem Voxel, eine Methode zur Registrierung von auseinander folgenden Messungen und eine genaue Charakterisierung des Messfehlers, um statistisch signifikante Veränderungen der T_2 -Werte identifizieren zu können. Basierend darauf ist es nun möglich einen Zusammenhang zwischen signifikanter T_2 -Änderungen und physiologischen Veränderungen herzustellen.

Ziel dieser Doktorarbeit war die Entwicklung einer Methode, die es erlaubt, in Longitudinalstudien anhand der Bestimmung von T_2 den Krankheitsverlauf im Gelenkknorpel auf Voxel Ebene darzustellen. Dieses Ziel wurde in vier Schritten erreicht:

1. **Genauigkeit und Präzision der T_2 -Werte:** Im Allgemeinen wird T_2 gemessen, indem eine Exponentialfunktion an mit verschiedenen Echozeiten (TE) gemessene Daten angefitet wird. Wegen der kurzen T_2 -Zeiten im Gelenkknorpel, der nötigen hohen Ortsauflösung und der beschränkten Akquisitionszeit leiden diese Daten unvermeidlich an einem niedrigen Signal-zu-Rauschen-Verhältnis (signal to noise ratio, SNR). Charakteristisch für die Verteilung des Rauschens in MR-Bildern ist der nichtverschwindende Mittelwert in Abwesenheit eines Signals. Deswegen geht das gemessene Signal bei langen TE-Zeiten nicht auf Null zurück. Wenn nun eine Exponentialfunktion an solche Daten gefittet wird, folgt daraus unausweichlich eine Überschätzung der T_2 -Zeit.

In Kapitel 4 werden zwei neue Fitmethoden vorgeschlagen, die die statistische Verteilung des Rauschens berücksichtigen: der Fit an eine rauschkorrigierte Exponentialfunktion und der Fit an eine Exponentialfunktion des quadrierten Signals abzüglich der doppelten Varianz des Rauschens. Genauigkeit und Präzision dieser Methoden wurden in Simulationen und Phantommessungen bestimmt. Konventionelle Fitmethoden (Lineare Regression und nichtlinearer Fit zu einer Exponentialfunktion) führten zu einer niedrigen Genauigkeit bei kurzen T_2 -Zeiten mit Überschätzungen um bis zu 500%. Die neu eingeführten Fitmethoden erzielten eine sehr hohe Genauigkeit für alle T_2 -Werten und SNR-Verhältnisse. Zudem resultierte der Fit mit einer rauschkorrigierten Exponentialfunktion in Präzisionen, die an die bestmögliche Präzision (bestimmt mit der Cramér-Rao lower bound Methode) heranreichen. Die Bedeutung der Fitmethode für in-vivo Messungen wurde in 7 Nachfolgeuntersuchungen des Patellaknorpels in sechs gesunden Probanden demonstriert.

2. **Entwicklung eines Algorithmus zur starren 3D-Registrierung:** Die Beobachtung des Krankheitsverlaufes erfordert den Vergleich von zu verschiedenen Zeitpunkten aufgenommenen Datensätzen. Voraussetzung dazu ist eine räumliche Registrierung der Datensätze mit einem Fehler, der kleiner als die räumliche Auflösung sein muss. In Kapitel 5 wird ein neuer Algorithmus zur starren 3D-Registrierung vorgestellt, der auf der Maximierung des überlappenden Volumens der zu registrierenden Datensätze beruht. Der Algorithmus wurde mit numerischen Simulationen und mit in-vitro Untersuchungen validiert. Dabei wurde gezeigt, dass der Fehler weniger als 25% der Voxelgröße betrug. Mit diesem Algorithmus wurde die voxelweise Reproduzierbarkeit von jeweils sieben T_2 -Messungen in sechs Probanden überprüft. Andere Anwendungen werden ebenfalls in Kapitel 5 vorgestellt.
3. **Bestimmung der T_2 -Messfehler in Nachfolgeuntersuchungen:** Das Konzept des "Messfehlers" wird hier sehr weit gefasst und berücksichtigt alle Fehlerquellen, die beim Vergleich zwei-

er Datensätze auftreten können (Kapitel 6). Abgesehen vom SNR, das die größte Fehlerquelle darstellt, fallen darunter auch der ‘Magic-Angle-Effect’, die Registrierungsmethode, die Segmentierung sowie die Interpolation. Eine unkomplizierte und überschaubare Methode zur Bestimmung der Messfehler basiert auf wiederholten Messungen in gesunden und OA-erkrankten Probanden. Da kurzfristig keine physiologischen Änderungen des Knorpels zu erwarten sind, reflektieren Änderungen im T_2 -Wert ausschließlich den Messfehler. Kennt man den Messfehler, so können die signifikanten Veränderungen des T_2 -wertes in Follow-up-Untersuchungen identifiziert werden.

4. **Zusammenhang zwischen T_2 -Änderungen und Physiologische Änderungen:** Zur Interpretation von T_2 -Änderungen wird in Kapitel 6 ein 2σ -significance chart eingeführt. Dieser erlaubt eine direkte Klassifizierung von T_2 -Änderungen, die in aufeinanderfolgenden Messungen auftreten können. Diese Klassifizierung unterscheidet sieben verschiedene Fälle und stellt damit vielfältige diagnostische Informationen bereit. Diese sieben Fälle können als farbkodierte Parameterkarten dargestellt werden und erleichtern dadurch die visuelle Analyse von Follow-up-Untersuchungen. Als globales Maß für die T_2 -Änderungen wird die mittlere signifikante Änderung ΔT_2 vorgeschlagen, die nur die Voxel berücksichtigt, deren Wert sich signifikant geändert hat.

Um den Nutzen dieser Methode zu demonstrieren, wurde eine kleine Patientengruppe ($n=5$), die mit MACT behandelt wurde, zufällig aus einer Population aus einer in unserem Institut laufenden MACT Studie ausgewählt. T_2 -Maps dieser Patienten wurden 1,5, 3, 6 und 12 Monate nach dem Eingriff gemessen. Die mittlere signifikante Änderung von T_2 korrelierte signifikant ($r^2=0.72$) mit dem Kniezustand, der mit dem subjektiven Knieformular der International Knee Documentation Committee (IKDC) bestimmt wurde. Interessanterweise, zeigte die mittlere signifikante Änderung von T_2 außerdem eine hohe Korrelation ($r^2=0.92$) mit der Anzahl der Chondrozyten im transplantierten Scaffold, was auf die Relevanz der Zellanzahl für den Erfolg der Therapie hindeutet.

Chapter 1 Introduction

“El agua no tiene huesos”
 (“Water has no bones”)
Spanish proverb

Osteoarthritis (OA) is a degenerative, painful and functionally limiting disease of the joint, which involves progressive loss of articular cartilage, eburnation of subchondral bone and inflammation of the joint capsule. Due to the high incidence of OA and the lack of an effective therapy, OA represents an enormous socioeconomic burden in most industrialized countries (see Chapter 2). A considerable limitation in the assessment of new therapies and drugs for OA is the absence of robust non-invasive methods for monitoring the progression of joint disease.

Articular cartilage is a very important entity in the diagnostic workup of OA, since degenerative changes of the collagenous network in the cartilage matrix are considered to be an entry point in the process of irreversible joint degradation. In the last decades, much effort has been invested in developing magnetic resonance imaging (MRI) methods to non-invasively assess the integrity of the cartilage extracellular matrix (see Chapter 3 for a detailed review). Among other quantitative MRI parameters, the relaxation time T_2 is especially suitable for diagnosis of OA, since it is the only easily accessible MRI parameter that is mainly sensitive to the organization of the collagen matrix.

Although T_2 has demonstrated to be sensitive to the degradation of the collagen matrix of the articular cartilage [Dardzinski97, Mosher00, Mosher04b], its use in the clinical routine has not yet become established. This is partially caused by the long acquisition times of the sequences for T_2 measurement, the necessity of image processing and more principally by difficulties in the interpretation of the T_2 maps. As can be seen in Fig. 6.2, the distribution of T_2 in healthy and OA-diseased volunteers is very similar, so that global T_2 estimators, such as the bulk mean or standard deviation, cannot sensitively and specifically discriminate healthy from early-OA cartilage. Only if a focal lesion with high T_2 values is present, the T_2 maps can be easily interpreted. Indeed, quantitative T_2 mapping has been revealed to be more sensitive for the detection of focal lesions than the standard MRI protocol [Hannila07].

T_2 has a great potential for comparison of successive examinations, which has been poorly exploited due to the lack of adequate tools for comparison of T_2 maps. Long-term studies of T_2 in articular cartilage used mean T_2 values to evaluate disease progression. These mean T_2 values are calculated either over the complete cartilage [Blumenkrantz04, Stahl07], or over a region of interest (ROI) defined on a lesion [Trattinig07a, Welsch08a, Domayer09, Welsch09]. Although the mean T_2 has the advantage of being straightforward to calculate, it is a coarse and not very sensitive measure of the changes undergoing in cartilage. Even more, the use of the averaged T_2 values means discarding the information of what is happening at a scale lower than the region where it is averaged.

Ideally, a method for comparison of follow-up examinations should be able to detect changes at the lowest scale, i.e. on a voxel basis. Developing such a method requires an accurate calculation of the T_2 values at each voxel to be as sensitive as possible, a method for registration of datasets acquired in different imaging sessions and an exact characterization of the measurement errors in T_2 to discriminate statistically significant changes in T_2 . Furthermore, it is possible to establish a connection between the significant changes in T_2 and the physiological changes undergoing in the cartilage.

This PhD thesis is devoted to the development of a method for the voxel-based assessment of disease progression in the articular cartilage with MRI follow-up examinations of the T_2 relaxation time. This objective was achieved in four steps:

1. **Accuracy and precision of T_2 values:** T_2 is usually measured by fitting data acquired at different echo times (TE) to an exponential function. In the articular cartilage the low T_2 times, the high resolution necessary to resolve the cartilage layers and the limited acquisition times unavoidably result in low signal-to-noise ratio (SNR) images for T_2 calculation. A characteristic of the noise distribution in MR images is that in absence of signal intensity it has a non-vanishing mean. As a consequence, at larger TEs the measured signal intensity does not decay towards zero. Therefore, if the measured signal intensity is fitted to an exponential function, which decays to zero, overestimation in T_2 will occur.

Two new voxel-wise fit methods are proposed in Chapter 4, which consider the distribution of noise: fit to a noise-corrected exponential and fit to an exponential function of the squared signal intensity minus two times the variance of noise. Accuracy and precision have been analyzed in simulations and in phantom measurements. Traditional fit methods (linear regression and nonlinear fit to an exponential) led to a poor accuracy for low T_2 with overestimations of the exact T_2 up to 500%. The noise-corrected fit methods demonstrated a very good accuracy for all T_2 values and SNR. Even more, the fit to a noise-corrected exponential resulted in precisions comparable with the best achievable precisions (Cramér-Rao lower bound). The importance of the fit method for in vivo T_2 calculation was assessed in 7 repetitive acquisitions of the patellar cartilage in 6 healthy volunteers.

2. **Development of a 3D rigid registration algorithm:** Monitoring disease is based on the comparison of cartilage datasets acquired at different time points during disease progression. This requires spatial registration of the datasets with an error lower than the voxel size. In Chapter 5, a new rigid 3D registration algorithm is introduced, which is based on the maximization of the overlap volume of the datasets to be registered. The registration algorithm was validated with numerical simulations and in vitro examinations demonstrating a registration error lower than 25% of the voxel size. The registration algorithm was used to investigate the voxel-based reproducibility of T_2 in 7 repeatedly acquisitions of the patellar cartilage in 6 healthy volunteers. Other applications of the registration algorithm are also presented in Chapter 5.
3. **Calculation of T_2 measurement errors in follow-up examinations:** The concept of measurement errors is used here in a broad sense including all source of errors involved in the process of the comparison of two datasets (Chapter 6). Additionally to the SNR, which is the most important source of T_2 measurement errors, sources of errors are, among others, the magic-angle effect, the registration method, the segmentation and the image interpolation. A straightforward

method to assess the measurement errors in T_2 is based on repeated acquisitions of healthy and OA-diseased volunteers. Since in short-term acquisitions no physiologic change in the cartilage is expected, the differences in T_2 are a consequence of the measurement errors only. The characterization of the errors allows identifying significant changes in T_2 in follow-up, since for each measured T_2 the range of expected T_2 values in follow-up is known a priori. Deviations from this range likely indicate a true change in T_2 .

4. **Relationship between the changes in T_2 and physiological changes in cartilage:** To interpret the changes in T_2 a 2σ -significance chart is introduced (Chapter 6). The 2σ -significance chart allows for straightforward classification of changes in T_2 that occur between two acquisitions of the same subject. This classification differentiates between 7 possible outcomes, thus providing manifold diagnostic information. Color-encoded maps of the outcomes represent a great simplification in the interpretation of follow-up examinations. As a global measurement of the changes that occurred in T_2 , the mean significant change, ΔT_2 , is proposed, which only considers those voxels whose T_2 has significantly changed in follow-up.

To test the usefulness of the method, a small cohort of patients ($n = 5$) who had undergone matrix-associated autologous chondrocyte transplantation (MACT) was randomly selected from the MACT patients included in an ongoing study in our department. T_2 maps of the patients were acquired in follow-up examinations 1.5, 3, 6 and 12 months after surgery. The mean significant change in T_2 was significantly ($r^2 = 0.72$) correlated with the knee condition as assessed with the subjective knee evaluation form of the International Knee Documentation Committee (IKDC). More interesting, the mean significant change in T_2 showed a high correlation ($r^2 = 0.92$) with the number of chondrocytes in the transplanted scaffold, thus indicating the relevance of the number of cells in the success of therapy.

Chapter 2 Anatomy and physiology of the articular cartilage

2.1 Anatomy

Hyaline cartilage is a highly structured connective tissue, which covers the contact surfaces of bones in joints. Other locations of hyaline cartilage are in the nose, the larynx and between the ribs and the sternum. Healthy hyaline cartilage is a translucent bluish-white tissue with stiff mechanical properties. Functions of the hyaline articular cartilage are the reduction of friction between bones in the joint, distribution of the load to the bony ends and to a less extent absorption of mechanical shocks.

The subject of this thesis is the articular cartilage of the knee. The knee is the largest and one of the most complex joint in the human body (Fig. 2.1). The knee presents a very thick cartilage, which due to the high load bearing of the knee is very commonly affected by OA (see Section 2.3).

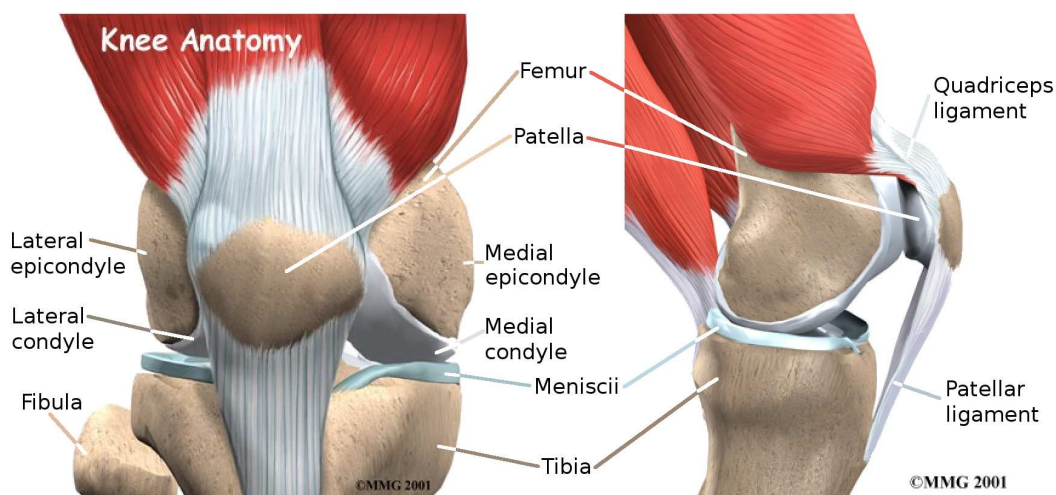


Figure 2.1: Schematic representation of the anatomy of the knee.

2.1 Anatomy

2.1.1 Composition

The articular cartilage consists of a gel solution of proteoglycans (PG) and other ionic components (especially Na^+), trapped in a network of collagen fibrils. The collagen network also nests the chondrocytes, which are the only cellular component of the hyaline cartilage. In the following the different constituents of the cartilage matrix are described in order of their abundance in cartilage.

1. **Water:** Water is the principal component of articular cartilage. Laboratory measurements in healthy cartilage revealed that water content decreases with age from $(75 \pm 1.1)\%$ at ages of 3–19 y to $(69.6 \pm 0.6)\%$ at ages of 60–90 y [Venn77, Maroudas80]. Water does not have a uniform distribution in cartilage. Typically, the water content decreases from 75% at the articular surface to 67% near to the bone-cartilage interface [Venn77, Maroudas80].

Since MRI bases on the detection of ^1H , which is mostly bound in water molecules, the water volume fraction (WVF)¹ can be measured with MRI. In a separate study not included in this thesis [Raya08a, Raya08b], we performed in vitro measurements of the WVF at 17.6 T in patellar cartilage. In the healthy patellar cartilage WVF showed a continuous decrease from the articular surface to the bone-cartilage interface (Fig. 2.2). An increase in WVF with the OA grade has been also observed [Raya08a, Raya08b]. Averaged water volume fraction was $(74 \pm 5)\%$ in healthy cartilage, $(77 \pm 5)\%$ in moderate OA and $(80 \pm 5)\%$ in severe OA.

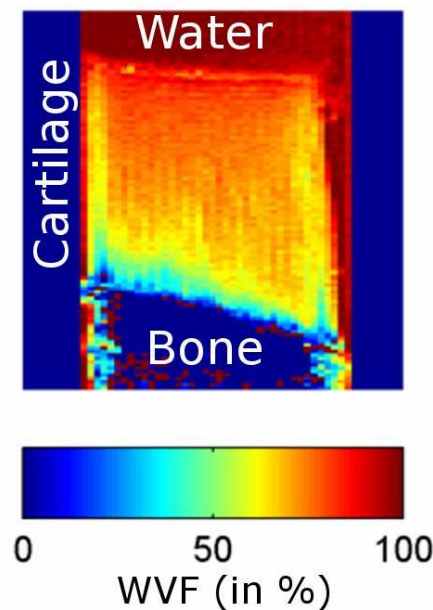


Figure 2.2: Example of a map of water volume fraction measured at 17.6 T on a healthy sample extracted from the patellar cartilage of a 23-year-old donor.

¹Water content is defined as the fraction of water mass to the total wet mass of the sample. However, in MRI only the volumetric water content is determined (also known as the water volume fraction). The transformation of the volumetric water content into the mass water content involves the dry density of the sample.

2 Anatomy and physiology of the articular cartilage

- Collagen:** The collagen represents approximately two thirds of the dry weight of the human articular cartilage. The collagen content decreases with age from 18.5% of the wet weight at ages of 3–19 y to 16.9% at the ages of 60–90 y [Muir70, Maroudas80]. Collagen distributes nonuniformly in cartilage, decreasing from the articular surface (21%) to the middle zone (15%) and then increasing again towards the bone-cartilage interface (19%) [Muir70, Venn77, Maroudas80].

There are more than 28 types of collagen described in literature, but in cartilage only the collagen types II, IX and XI are significantly present. Type II collagen represents more than 90% of collagen in mature human articular cartilage [Buckwalter98b]. Also present, although in small extents, are the collagen type IX (1%) and XI (3%) [Eyre02]. Collagen appears in fibrils of thin (≈ 30 nm) and thick (≈ 100 nm) diameters [Muir70, Clarke71, Ratcliffe84, Glaser02, Kadler08]. Although the process of formation of fibrils (fibrillogenesis) is not completely understood, it seems plausible that collagen type XI, which is only found in thin fibrils [Keene95], acts as a nucleator initiating the collagen fibrillogenesis [Kadler08]. In the process of maturation (thickening) of the fibril, the collagen type IX and XI are progressively removed and substituted by type II collagen [Eyre02, Kadler08].

A relevant property of the collagen molecules with important consequences for the relaxation time T_2 in cartilage, is the interaction between water and collagen [Bella94]. Water interacts with collagen by hydrogen bridges and forms a highly ordered hydration network, which helps stabilizing the collagen molecules [Bella94, Brodsky08]. By this interaction the motion of water molecules becomes restricted, so that the hydrogen atoms of bounded water molecules experience an effective dipole-dipole interaction between each other. This interaction is an efficient mechanism of relaxation, which is responsible for the short T_2 times in cartilage.

- Proteoglycans (PG):** PG represents up to 10% of the wet weight of the cartilage [Maroudas80, Knudson01, Kiani02]. Proteoglycan consists of a central core protein to which glycosaminoglycan (GAG) side chains are covalently linked [Wight92, Bayliss99, Knudson01]. In cartilage, 90% of all the proteoglycan is present in form of aggrecan, which is a PG composed of the GAGs chondroitin sulfate (100 - 150 chains per aggrecan) and keratan sulfate (30 - 60 chains per aggrecan) [Bayliss99, Kiani02].

The aggrecan can bind non-covalently by a link protein to a strand of hyaluronase (a non-sulfated GAG), forming an aggregate. A single hyaluronase strand can bind up to 100 aggrecans [Buckwalter98b, Kiani02], forming a large aggregate which is entrapped in the collagen network compressed to only a fraction of their volume in water solution. The PG bind to the collagen network through the regions rich in keratan sulfate GAG.

Under physiological conditions, the sulfate and carboxyl residues of the GAGs are ionized and as a result PG becomes so negatively charged, that it could disintegrate the cartilage if not neutralized by Na^+ . Therefore, a great difference in Na^2 concentration between cartilage and synovial liquid occurs, which is one important factor of the osmotic pressure in cartilage (see Section 2.2).

- Chondrocytes:** The chondrocytes are the only cellular component of the cartilage and represent approximately 1% of the cartilage volume [Buckwalter98b]. Chondrocytes are responsible for the synthesis and degradation of all macromolecules in the extracellular matrix and their

2.1 Anatomy

organization into a highly ordered structure. Although chondrocytes in articular cartilage vary in shape, size, orientation and metabolic activity [Aydelotte88b, Aydelotte88a, Aydelotte92], all chondrocytes contain the organelles necessary to synthesize the matrix components.

Chondrocytes originate from undifferentiated mesenchymal cells that cluster together and begin to synthesize molecules of the extracellular matrix in a process known as chondrogenesis [Goldring06]. As the extracellular matrix grows the chondrocytes progressively separate from each other. During the formation and growth of articular cartilage the chondrocytes show their highest metabolic and division rates [Goldring06]. With skeletal maturation, the metabolic rate decreases and cell division stops, so that chondrocytes remain unchanged in position and appearance for decades [Tallheden06]. However, recent *in vitro* and *in vivo* experiments have evidenced that under certain stimulus the chondrocytes can migrate through the extracellular matrix [Morales07].

The balance between the catabolic (synthesis) and anabolic (degradation) activities of the chondrocytes is regulated through interaction with the extracellular matrix. The deformation of the matrix produces a variety of signals (electrical, mechanical...), that can be detected by the chondrocytes [Guilak95]. The chondrocytes respond to these signals with the release or inhibition of cytokines (interleukins, interferons, tumor necrosis factors and growth factors), which causes enhancement or retardation of the matrix synthesis and degradation [Lotz95, Huber00, Goldring08]. However, the details of the regulation mechanism remains poorly understood [Goldring08]. In the absence of disease, the chondrocytes maintain a low rate of replacement of cartilage matrix proteins with a half-life of collagen over 100 y [Verzijl00] and a half-life of PG in the range of 3–24 y [Maroudas98].

5. **Other components:** Other components of the articular cartilage are present in lower fractions ($< 1\%$ of the wet weight), but are also the basis of important functions. Free cations (principally ^{23}Na) guarantee the electroneutrality of the extracellular matrix. Due to the high electronegativity of PG molecules, free cations in the articular cartilage are present in a much higher concentration than in the surrounding tissues. ^{23}Na concentration in cartilage varies from approximately 200 mmol/L at the surface to 390 mmol/L in the deep cartilage with a mean concentration of 320 mmol/L [Shapiro00], which is 150% higher than in synovial liquid [Gray08]. Anions, especially Cl^- , are present at much lower concentration than in the synovial fluid. The concentration of Cl^- in cartilage is 50% lower than in synovial liquid. The difference in the electrolyte concentration between the cartilage matrix and the synovial fluid is an important factor for the osmotic pressure in articular cartilage (see section 2.2).

Several non-collagenous proteins are present in the articular cartilage. Most of these proteins help in binding the different components of the extracellular matrix: Anchorin CII anchors chondrocytes to the pericellular region [Mollenhauer84], fibronectin and tenascin bind different molecules of collagen type II and collagen type XI to form collagen fibrils [Keene95]. However the role of the non-collagenous proteins needs to be elucidated.

2.1.2 Structure

Although the first work supporting that the cartilage contains a fibrous component oriented mainly vertically to the joint surface was published as early as 1743 [Hunter43] the existence of a fibrous

2 Anatomy and physiology of the articular cartilage

structure in the cartilage remained controversial until the beginning of the 20th century. In 1925, the publication of the seminal work of Benninghoff [Benninghoff25] introduced the model that the collagen fibrils arrange in an arcade-like form and ended a controversy lasting almost two centuries [Clarke71].

The discovery of the electron scanning and transmission microscopy allowed examination of the cartilage matrix at micrometer scales and thus resolving the fiber structure of the cartilage [Clarke71]. Observed in the scanning electron microscopy (SEM), the articular cartilage presents four well differentiated zones according to the orientation of the collagen fibrils (Fig. 2.3). The collagen fibrils anchor to the subchondral bone in the calcified zone, which borders to the radial zone across a wavy, irregular interface known as the tidemark. In the radial zone, collagen fibrils of thick diameters (100-140 nm) arrange perpendicular to the bone-cartilage interface. The transitional zone is characterized by a fuzzy arrangement of the collagen fibrils, with an increasing fraction of fibrils oriented parallel to the articular surface, with decreasing distance to the articular surface. In the tangential zone, just underneath the articular surface the densely packed thin (30-60 nm) collagen fibrils are oriented parallel to the articular surface. The tangential zone is enclosed by the lamina splendens [Weiss68], a layer of fine fibrils with no cellular component, which acts as a filter preventing macromolecules larger than 6 nm to enter or escape from the cartilage matrix.

The relative height of the zones varies from one cartilage to the other and, within a cartilage plate, between different anatomical regions. For example, in the patellar cartilage the relative thickness of the different zones as measured with SEM are: (65 ± 12)% radial, (30 ± 16)% transitional and (5 ± 9)% tangential [Filidoro08].

The proteoglycans do not distribute homogeneously from the articular surface to the bone-cartilage interface (Fig. 2.4). With a combination of chemical and histochemical methods Stockwell and Scott [Stockwell67] were the first to demonstrate an increased GAG content in the deep-zone of the cartilage. Further studies with chemical methods [Maroudas69, Bayliss83], the cation tracer method [Maroudas76, Venn77, Maroudas80], immunoelectron microscopy and radioimmunoassay [Ratcliffe84] and a hyaluronan binding region-link protein complex [Parkkinen96] consistently corroborated the inhomogeneous distribution of PG. The measured fixed charge density in articular cartilage, which is almost entirely due to the GAG side chains of the PG, varies between 50 mmol/L at the surface to 200 mmol/L in the deep radial zone [Maroudas76, Venn77, Maroudas80]. The concentration of PG depends on the mechanical stress on the cartilage [Slowman86], and decreases with age [Venn78, Buckwalter85, Buckwalter94, Brown98, Bayliss99].

Chondrocytes show a higher cell density near the articular surface (Fig. 2.4). In the tangential zone chondrocytes are elliptically shaped with the principal axis oriented parallel to the articular surface. In the transitional zone chondrocytes are predominantly spherical and appear isolated, whereas in the radial zone columns of chondrocytes are usually observed. Chondrocyte concentration also varies with the anatomical location, likely due to differences in the loading conditions of each cartilage region [Huber00, Quinn05].

In the matrix the chondrocytes are located in the so-called lacunae (see the holes in the histological cuts in Fig. 2.4). Under the electron microscope the structure of the collagen matrix around the cells allows to differentiate three regions: the pericellular, territorial and interterritorial regions. The first region surrounding the chondrocytes is the pericellular region, a thin matrix rich in PGs and with no collagen that binds the cell membrane to the extracellular matrix. The territorial region is formed by thin collagen fibrils, which adhere to the pericellular region, and provides mechanical protection

2.2 Physiology

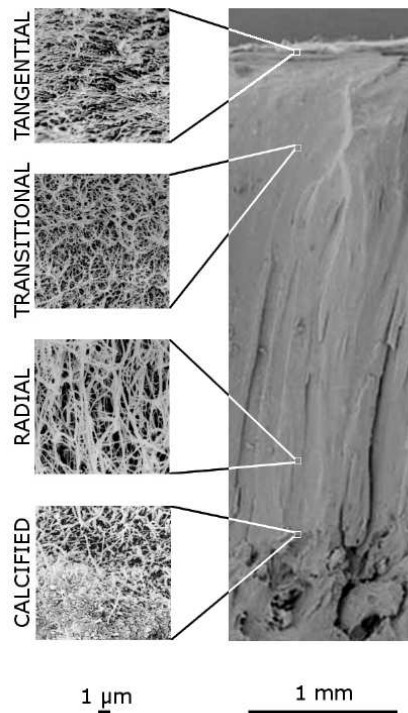


Figure 2.3: SEM images of the different zones of articular cartilage, obtained with a resolution of $6000\times$. In the overview (right, acquired with a resolution of $20\times$), squares approximately indicates the position of the details.

to the cell by loading and deformation of the matrix [Poole97, Buckwalter98b]. The interterritorial region differs from the territorial region in the thickness of the collagen fibrils and their orientation [Buckwalter98b, Huber00].

2.2 Physiology

The unique mechanical properties of cartilage result from the balance between the swelling pressure due to the highly compressed and negatively ionized PGs and the restraining forces exerted by the collagen network.

The osmotic pressure induced by PGs have two components. On the one hand, the PG in the cartilage matrix are so densely packed that they occupy only a fraction of their aqueous volume, thus causing a strong non-ideal osmotic pressure. On the other hand, the high difference in ^{23}Na concentration between the extracellular matrix and the synovial fluid induced by the PG generates an additional osmotic pressure. Both components of the swelling pressure are approximately of the same order of magnitude with values as high as 1.7×10^5 Pa (1.7 atm) [Maroudas76, Maroudas85]. The nonuniform distribution of PG from the articular surface to the bone-cartilage interface in healthy

2 Anatomy and physiology of the articular cartilage

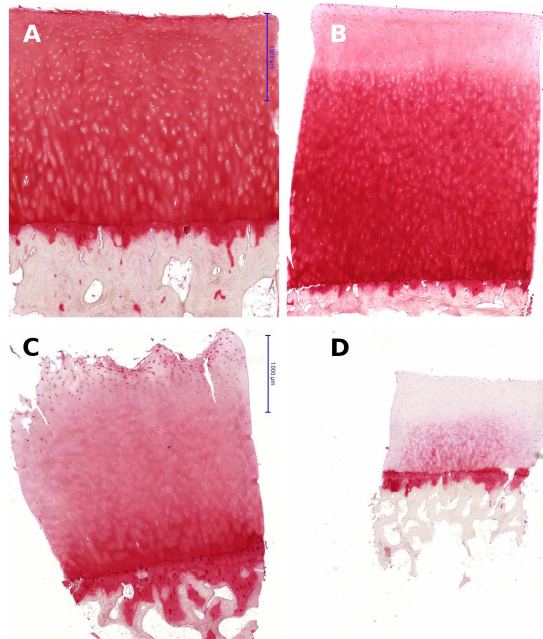


Figure 2.4: Examples of Safranin-O stained $7 \mu\text{m}$ histological cut sections. Safranin-O stain binds to the GAG side chains of the PGs, so that the intensity in red is a semi-quantitative measurement of the GAG concentration. **A.** Sample of a healthy patellar cartilage of a 29-years-old female donor. The PG shows a concentration increasing from the articular surface to the bone-cartilage interface. **B.** Sample of a healthy patellar cartilage of a 39-years-old male donor. Histology revealed loss of the PG in 25% of the superficial cartilage. **C.** Slice cut of the patellar cartilage of a 43-years-old male with signs of fibrillation. Observe the high concentration of chondrocytes at the tangential zone marked by the Safranin-O, thus indicating increased PG production. **D.** Histological cut of the patellar cartilage of a 73-years-old male, demonstrating great PG loss but with an apparently intact collagen structure.

cartilage produces a smooth gradient in the osmotic pressure, with lowest values at the articular surface, thus protecting the collagen network from long term fatigue [Maroudas76].

In equilibrium, the elastic force exerted from the collagen network balance the osmotic pressure generated by the PGs. If an external force compresses the cartilage, water is squeezed from the most superficial layers dragging the cations with it [Burstein93, Duvvuri98, Lüsse95], so that the fixed negative charge of the GAGs experience a strong repulsive electrostatic force, which opposes the compressive stress [Maroudas85, Xia00]. After removal of loading, the osmotic pressure of the PGs accounts for a rapid recovery of the cartilage. In a separate study not included in this thesis we performed a multiparametric MRI examination of the changes which occurred in the cartilage under compression [Raya08c]. We observed a redistribution of water and a reorientation of the collagen network (Fig. 2.5).

The differences in orientation and composition of the collagen fibrils in the different zones of the cartilage (see section 2.1.2) are a consequence of their specific dedicated mechanical functions. The

2.2 Physiology

densely packed collagen fibrils parallel to the articular surface in the tangential zone distribute the compression force applied at the articular surface to a broad region in the transitional zone [Xia00], where the random organization of the fibrils with numerous fibrils oriented obliquely optimally resist the shearing forces. The thick fibrils in the radial zones efficiently transmit the stress towards the tide mark. The wavy and irregular shape of the tide mark transforms the shear forces into tensile and compressive forces, which are absorbed by the subchondral bone [Imhof00]. The articular cartilage is a poor shock absorber. Only between 1% and 3% of the loading forces are absorbed in the cartilage [Hoshino87], whereas subchondral bone is responsible for 30% of the stress attenuation. The residual stress is absorbed by the cortical bone and the joint capsule [Hoshino87].

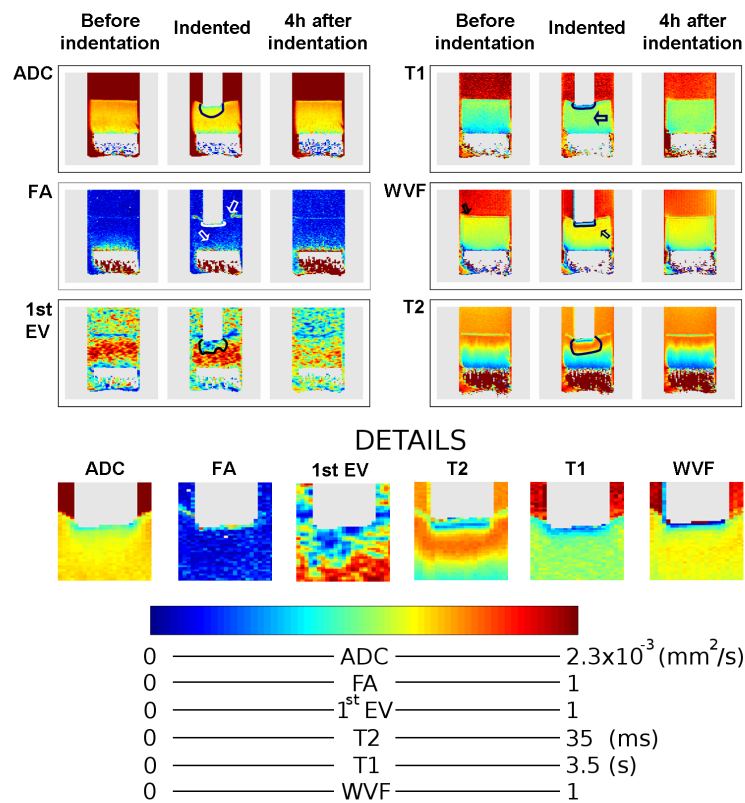


Figure 2.5: MRI maps (ADC, FA, first eigenvector (1st EV), T₂, T₁, and water volume fraction (WVF) measured on the same sample native, under indentation and four hours after indentation. Lines and arrows indicate significant change in the MR parameters under loading conditions. Indentations lead to significant alteration of all MRI parameters, although in different ranges, since the different MRI parameters are sensitive to different components of the cartilage (see Chapter 3) [Raya08c].

2 Anatomy and physiology of the articular cartilage

2.3 Osteoarthritis

OA is the most common joint disease affecting a majority of the population older than 65 y. OA produces a progressive degeneration of the joint with cartilage loss, inflammation of the synovial capsule, fibrosis and subchondral bone remodelling. OA is therefore associated with pain, joint stiffness and, in its latest stages, with functional impairment and disability of the joint. Due to its large prevalence OA represents a major socioeconomic burden in most industrialized countries (see 2.3.6).

2.3.1 Pathogenesis

According to the origin of OA it is differentiated between primary or idiopathic OA, i.e. OA occurring in the absence of a known cause, or secondary OA, when occurs as a consequence of injury, infection, metabolic disorder... Yet, idiopathic OA is by far the most common cause of OA.

Although many of the mechanisms responsible for cartilage degradation are still unknown, the fundamental pathogenetic process in OA is characterized by an imbalance between the anabolic and the catabolic activity of chondrocytes. The process of cartilage degradation is usually divided in three overlapping stages:

1. Macromolecular degradation of the cartilage matrix. The PG concentration decreases first at the articular surface and later also at the bone-cartilage interface [Buckwalter98a]. The loss of PG causes a redistribution of the osmotic pressure, which result in additional mechanical load in other regions of the collagen network. [Maroudas76].
2. Response of the chondrocytes to the process of degradation. Changes in the extracellular matrix induce changes in the osmolarity, the charge density and the strain, which act as signals that the chondrocytes receive. Chondrocytes react to these signals with a transient proliferation and increased metabolic activity, thus stimulating the synthesis of macromolecules.
3. Failure of the chondrocytes in restoration of the cartilage, with premature apoptosis of the chondrocytes. In the last years, the importance of the cytokines and inflammatory mediators in the process of cartilage degeneration has become more evident [Fernandes02, Goldring08]. These molecules inhibit the collagen synthesis and provoke the chondrocytes to produce nitric oxide, NO, and metalloproteinases (responsible for the degradation of PG) [Krasnokutsky07, Goldring08]. NO is a fast messenger between cells, which seems to play an important role as inhibitor of PG synthesis, metalloproteinase activation and the premature apoptosis of chondrocytes [Amin95, Hancock08].

As chondrocytes fail, progressive loss of cartilage takes place, thus leading to pathological changes in most of the joint structures. Cartilage loss causes changes in the subchondral bone, which includes increased density of the subchondral bone and the appearance of bony spurs (osteophytes). Osteophytes are small round lumps of extra bone that grow at the bone-cartilage interface and usually around the periphery of the joint, thus frequently causing motion restriction and pain. The synovial membrane often shows inflammatory reaction and may contain fragments of articular cartilage [Myers92]. With time, the ligaments, capsule and muscles become contracted, related to the stiffness and weakness associated with OA.

2.3 Osteoarthritis

Finally, due to the absence of innervations in the articular cartilage, pain in OA occurs due to the damage induced by the cartilage loss in the neighbouring joint structures (subchondral bone, joint capsule, ligament...) [Hancock08]. Therefore, the severity of the damage of cartilage is not closely related to the severity of the clinical symptoms.

2.3.2 Risk factors

Multiple risk factors have been identified, which affect the onset and progression of OA. These factors can be divided into systemic risk factors, which influence susceptibility of any joint to OA, and local mechanical risk factors, which determine the exposure of individual joints to injury.

Age is the most important systemic risk factor for idiopathic OA. The incidence of OA increases strongly with age. Almost 60% of the population over 70 years suffers from OA [Arden06]. It should be mentioned that OA is not simply the result of aging in the cartilage [Buckwalter98a, Horton06]. The relation between aging and degradation of the cartilage remains still uncertain [Horton06]. Gender is also a relevant systemic risk factor for OA. The incidence of OA in women is higher than in men, especially after an age of 50 y [Oliveria96]. Other systemic risk factors are bone density and osteoporosis, genetic factors and nutrition [Arden06, Goldring07].

Local mechanical risk factors include, among others, obesity, repetitive joint loading, joint instability, intra-articular crystal deposition, muscle strength and weakness [Arden06, Goldring07].

2.3.3 Diagnosis

Gold standard for the diagnosis of OA remains the plane projection radiograph in combination with clinical symptoms. Signs of OA in radiographs include narrowing of the joint space, presence of osteophytes and changes in the subchondral bone. Nowadays, the most widely used criteria, which were developed by the American College of Rheumatology [Altman86], combine recurrent joint pain in the last month and radiographic findings.

The most broadly used classification of OA grade according to the radiographic findings is the Kellgren and Lawrence classification [Kellgren57], which is a five point scale from 0 to 4. A score of 0 (none) is assigned if no osteoarthritic features are found. A score of 1 (doubtful) indicates osteophytes of doubtful importance. A score of 2 (minimal) indicates definite osteophytes without narrowing of the joint space. A score of 3 (moderate) is given when the joint space has diminished. A score of 4 (severe) is assigned if greatly reduced joint space and sclerosis of the subchondral bone is observed.

The diagnosis of OA based on the analysis of X-ray images is not sensitive to the biochemical composition of cartilage, and does not correlate well with the clinical symptoms [Arden06], and the results may depend on the chosen direction of X-ray projection [Duncan06]. From post-mortem studies it is known that the pathological process starts several years before radiological detection of OA is possible [Byers70]. There is a great potential of MRI with respect to the radiographic gold standard, since MRI potentially offers the diagnosis of early degenerative changes in the cartilage matrix. This is the subject of Chapter 3.

2 Anatomy and physiology of the articular cartilage

2.3.4 Prevalence and incidence

Not all the joints are equally affected by OA. Knee, hip and hand are the most commonly affected joints. Spine and foot joints are also frequently affected by OA. Less affected are the wrist, shoulders and ankles. Involvement of more than one joint is also common, and epidemiologic studies demonstrate that this occurrence cannot be explained by chance or age alone [Cushnaghan91]. This thesis is confined to the knee articular cartilage and thus the data about the prevalence and incidence of OA will be restricted to the knee.

Prevalence

First data about the prevalence of OA were obtained by systematic autopsy studies. In a population over 70 y, more than 60% of the male knees and more than 70% of the female knees presented some findings of OA (cartilage loss, subchondral bone alteration, osteophytes...) [Arden06].

Population-based studies using plane radiographs resulted in lower prevalence due to the low sensitivity of radiographs to detect mild OA. A study from the Netherlands included 6 585 inhabitants randomly selected of the total population of a dutch village [Saase89]. The prevalence of knee OA strongly correlated with age and presented clear gender differences (see Fig. 2.6). There is no similar study for Germany.

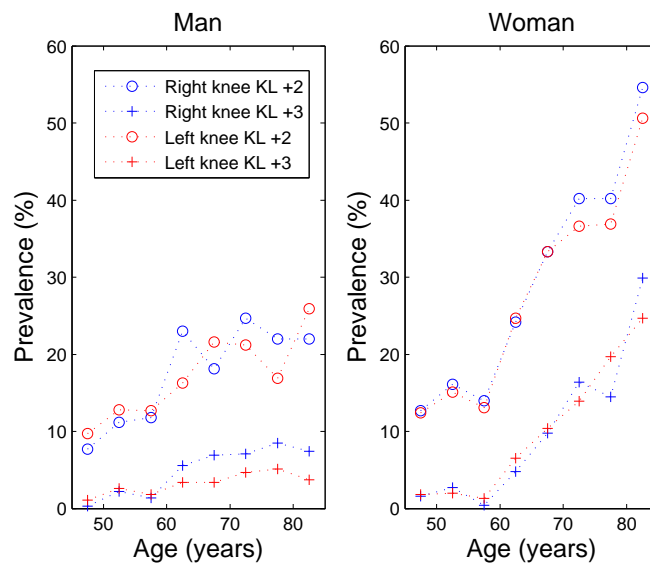


Figure 2.6: Prevalence of knee OA as estimated from 6 585 inhabitants of a dutch village [Saase89]. Prevalence correlates strongly with age. Markedly gender differences can be appreciated. KL +2 denotes Kellgren and Lawrence scale greater or equal to 2, KL +3 denotes Kellgren and Lawrence scale greater or equal to 3.

2.3 Osteoarthritis

Incidence

There are several epidemiological studies of the incidence of OA [Wilson90, Oliveria95, Cooper00]. The total incidence of knee OA in these studies varies between 164 and 250 per 100 000 persons-year. Again incidences showed an important gender and age dependence. Oliveria et al. [Oliveria95] found that the incidence of knee OA varies between 75 per 100 000 persons-year at age of 30-39 y to 380 per 100 000 persons-year in man and 475 per 100 000 persons-year in woman at age of 70-79 y.

2.3.5 Therapy

Nowadays there is no effective treatment against OA. Indeed, most of the international guidelines recommend nonpharmacological treatments as the first-line management of OA patients [Jordan03, Conaghan08, Zhang08]. The core of nonpharmacological interventions include information of the patient, strengthening exercise to reinforce the musculature, education of the patient to avoid positions or movements, which overload the cartilage, and interventions to achieve weight loss if the person is overweight or obese. For pain reduction additional nonpharmacological treatments are suggested: local application of heat and cooling, stretching, transcutaneous electrical nerve applications, use of suitable footwear (shock absorbing) and support and braces for those persons who cannot develop their daily living normally.

The pharmacological treatments focus on pain relief. Paracetamol and topical non-steroidal anti-inflammatory drugs are at first recommended for low to moderate pain. If this fails, opioid analgesics can be supplied. Moderate to severe pain is considered as indication for intra-articular corticosteroid injections.

In advanced stages of OA, as pain, stiffness and reduced function of the articulation limits the patient's quality of life, joint replacement surgery (arthroplasty) can be performed. In arthroplasty, the joint surface is partially or totally replaced by a prosthesis to permit recovery of the joint motion.

2.3.6 Socio-economical aspects of OA

OA is the leading cause of physical disability in most industrialized countries, and therefore represents an enormous burden for the social and welfare systems. According to the data published by the *Robert Koch-Institute* [Koch-Institut06], almost every fourth German is diagnosed as suffering from OA. The *Deutsche Bundesamt für Statistik* perform every two years a survey of the direct health care expenses caused by the most relevant diseases [Bundestamt08]. From 2002 until 2006 (last data reported) there was a clear trend of increasing direct expenses caused by OA: 7 123 Mio € in 2 002, 7 275 Mio € in 2 004 and 7 474 Mio € in 2 006. In addition, a considerable proportion of lost workdays, early retirements and rehabilitation measures are caused by OA, making it one of the most important chronic diseases affecting the German economy. Together with indirect expenses, which amounted to 3 000 Mio € in 2002, this results in a total amount of costs of 10 200 Mio € (approximately 0.5% of the gross national product).

Chapter 3 MRI of articular cartilage

The unique mechanical properties of the articular cartilage are a consequence of its molecular structure and organization. As described in Section 2.3, in the early stages of OA a progressive loss of PG from the articular surface to the bone-cartilage interface occurs with a subsequent destruction of the collagen network [Buckwalter98a]. Due to the low ability of the chondrocytes to regenerate the extracellular matrix (especially the collagen fibrils, which have a mean life in the matrix over 100 years), an early diagnosis of OA may have an important influence on the outcome of OA patients. Nowadays, nonpharmacologic treatments, whose effectiveness critically depends on an early onset of the therapy, are recommended by international guidelines as the first-line management of patients with OA (see Section 2.3.5).

Gold standard for the diagnosis of OA remains the plane radiograph in combination with clinical symptomatic (see Section 2.3.3). Plane radiographs are insensitive to the integrity of the cartilage matrix, so that the diagnosis bases on indirect manifestations of OA. From post-mortem studies it is known that the pathological process takes place several years before conventional radiological detection of OA is possible [Byers70]. Even more, the symptoms of OA do not correlate well with the radiographic features of OA.

MRI presents many advantages for the imaging of the joint, since it is non-invasive, radiation-free and has an excellent contrast for soft tissues. In the last decades, much effort has been invested in developing MRI methods to noninvasively assess the integrity of the extracellular matrix. In the following, the most relevant MR imaging methods for the cartilage are briefly described. See Table 3.1 for a summary of the methods described in this chapter. Only for the T_2 relaxation time, on which this thesis bases, the measurement techniques and the current results in articular cartilage are addressed in more detail.

3.1 MRI of the proteoglycans

The most widely used MRI methods for the measurement of the PG content base on the indirect measurement of the fixed charge in the cartilage matrix, which is mostly, if not completely, due to the GAGs [Maroudas69]. The key idea of these methods is to image the equilibrium distribution of free-mobile ions in cartilage, which is determined by the distribution of the fixed negative charge. The cation ^{23}Na , which is responsible for the electroneutrality in cartilage, is the natural tracer of the fixed negative charge. Another possibility is to introduce MR-visible ions, such as the anionic contrast agent $\text{Gd} - \text{DTPA}^{-2}$ (a complex of gadolinium with a chelating agent, diethylenetriamine penta-acetic acid). Another parameter has been demonstrated to be sensitive to the PG content is

3.1 MRI of the proteoglycans

Table 3.1: Summary of the MRI methods for the knee

| Method | Sensitive to | | | Validated | Advantages | Disadvantages |
|----------------------|--------------|-------|----------|-----------|---------------------------|-------------------------------|
| | PG | Coll. | Early OA | | | |
| ²³ Na-MRI | ++ | -- | ++ | ++ | Na equil. with GAG | Low SNR, hardware |
| dGEMRIC | ++ | - | ++ | ++ | Early OA, robust | Use of Gd(DTPA) ²⁻ |
| T_2 | - | ++ | + | ++ | Collagen sensitive | T_{aq} , magic-angle |
| $T_{1\rho}$ | ++ | ? | + | + | No Gd(DTPA) ²⁻ | Unspecific, T_{aq} , SAR |
| Volume | -- | - | +- | ++ | Reproducible, robust | Not for early OA |
| DTI | + | + | + | -- | Collagen, PG | T_{aq} , SNR |
| gagCEST | ++ | -- | ? | -- | PG specific | Clinical evaluation |
| UTE | -- | + | ? | -- | Imaging BCI | Diagnostic value? |

Coll. = Collagen, T_{aq} = acquisition time

the relaxation time in the rotating frame, $T_{1\rho}$, although it gives no direct quantification of the PG concentration.

3.1.1 Sodium MRI

The nucleus of the sodium atom is composed of 11 protons and 12 neutrons and has a nuclear spin of 3/2, which invest the nucleus with a non vanishing quadrupole moment. The gyromagnetic ratio (γ) of sodium is $\gamma_{Na} = 11.3$ MHz/T, so that sodium MRI cannot be performed with the same hardware as proton MRI. Due to the spin 3/2 and its abundance, sodium is after ¹H the most visible nucleus in the human body.

In healthy articular cartilage, ²³Na shows a concentration of 362 mmol/L, that means a proportion of 1 ²³Na atom for each 307 atoms of ¹H [Shapiro00]. Since sodium also presents a lower the gyromagnetic ratio than hydrogen, the SNR of ²³Na-MRI is much lower than that of ¹H-MRI. Therefore, ²³Na-MRI requires from high magnetic fields (>3 T).

The ²³Na relaxation time T_2 is governed by the quadrupolar interaction between the non-spherical ²³Na nucleus and the surrounding electric field gradients. In cartilage, ²³Na- T_2 presents a bi-exponential decay with a slow component of about 10–12 ms with a weight factor of approximately 40% and a rapid component of approximately 1–2 ms with a weight factor of 60% [Reddy97]. Therefore, the quantitation of the sodium concentration requires using ultra-short RF pulses and fast acquisition schemes to measure also the rapid component of T_2 .

The first in vivo images of human ²³Na were acquired by Reddy et al. [Reddy97]. First ²³Na images with an in-plane resolution of 5 mm and a total of 20 slices were acquired in 20 min with a SNR of 8 [Reddy97]. Insko et al. [Insko97] provided the first high resolution Na images with sub-millimeter in plane resolution and a SNR up to 40.

The first proof of the potential of ²³Na-MRI for the detection of early degradation in OA was given by Reddy et al. [Reddy98]. High contrast in signal intensity between the two lateral facets of a bovine patella, one of them with induced PG depletion, was observed with Na MRI. Posterior studies have systematically analyzed the effect of PG depletion in the Na relaxation times [Insko99,

3 MRI of articular cartilage

Shapiro00, Borthakur06]. With a 50% PG depletion Na relaxation time T_1 increased from 18 to 26 ms, whereas the T_2 reduced to about 50% [Insko99]. Experiments performed in vivo with Yorkshire pigs demonstrated that the quantification of Na is sensitive to cartilage degradation and correlates well with histological findings [Wheaton04a] (Fig. 3.1).

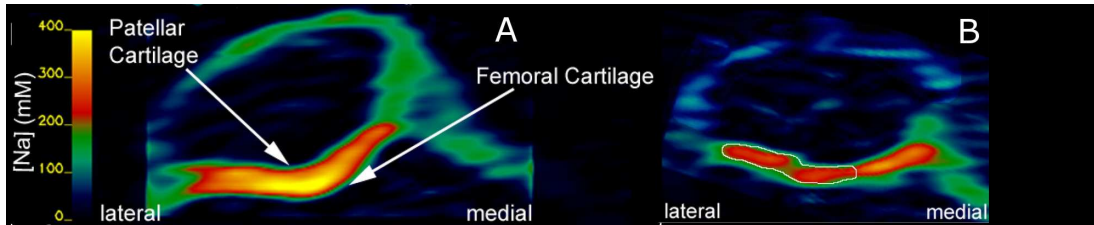


Figure 3.1: A. Transverse section from the three-dimensional sodium map of a healthy human subject. The bar scale on the left represents sodium concentration in millimoles. The cartilage in the patella and in the femoral condyle is labeled accordingly. The sodium concentration in the healthy cartilage is homogeneous throughout both the medial and lateral sides. B. Transverse section of a three-dimensional sodium map from a symptomatic subject. The region of decreased sodium concentration that corresponds to decreased FCD is outlined in white. (Adapted from [Wheaton04a])

In spite of the high specificity of ^{23}Na -MRI to the measured PG content, the additional hardware required to perform ^{23}Na -MRI, the low ^{23}Na relaxation times in articular cartilage, which still decrease with PG loss, combined with the limitations in the shortest achievable echo times due to the gradient strength, make ^{23}Na -MRI a technique far beyond clinical routine.

3.1.2 Delayed Gadolinium enhanced MRI of the cartilage (dGEMRIC)

The idea of using the MRI contrast agent $\text{Gd}(\text{DTPA})^{2-}$ to detect the fixed negative charge of the extracellular matrix with ^1H -MRI was first proposed in 1996 by Bashir et al. [Bashir96]. The imaging technique based on this idea is known as delayed Gadolinium enhanced MRI of the cartilage (dGEMRIC). For in vivo imaging $\text{Gd}(\text{DTPA})^{2-}$ is injected intravenously with a concentration of 0.2 mmol/L/kg (“double concentration”). Afterwards, the patient is asked to walk or do some exercise for a short time (between 10 and 15 min), to facilitate diffusion of the contrast agent. 90 min after injection it is assumed that the $\text{Gd}(\text{DTPA})^{2-}$ is balanced in the joint [Burstein01]. Due to the anionic character of $\text{Gd}(\text{DTPA})^{2-}$, in equilibrium its concentration is inversely proportional to the concentration of the fixed charge. The $\text{Gd}(\text{DTPA})^{2-}$ concentration can be measured with the T_1 relaxation time, which grows almost linearly with the $\text{Gd}(\text{DTPA})^{2-}$ concentration (at least for the concentrations observed in the cartilage). In MRI, T_1 is usually measured with inversion-recovery turbo-spin-echo sequence (TSE) or with a saturation-recovery fast low-angle shot (FLASH) sequence.

If the condition of equilibrium is known, as is the case in measurements in vitro, T_1 measured after $\text{Gd}(\text{DTPA})^{2-}$ injection can be converted to the GAG concentration [Bashir97]. The dGEMRIC-measured GAG concentration has been demonstrated to correlate very well with the GAG concentrations measured with ^{23}Na -MRI and biochemical assays [Bashir96, Bashir97, Bashir99], although dGEMRIC slightly overestimated the GAG concentration measured with biochemical methods [Bashir96].

3.1 MRI of the proteoglycans

In vivo the equilibrium condition is unknown, thus it is only possible to calculate relative GAG concentrations. However, several factors may influence the equilibrium conditions, so that in practice the T_1 measured after $\text{Gd}(\text{DTPA})^{2-}$ injection is used directly as a dGEMRIC index [Gray08]. Validation of dGEMRIC in vivo has been performed in patients undergoing total joint arthroplasty by measuring the knee before and after arthroplasty and correlating these measurements with histology [Bashir99]. In vivo, regional reproducibility of the dGEMRIC from day to day was lower than 12.9% [Multanen08].

Abnormal dGEMRIC indices have been observed in patients whose plain radiographs did not show any sign of OA [Williams03], thus indicating the potential of dGEMRIC for the early diagnosis of OA. The dGEMRIC index appears to be sensitive to cartilage-modifying injuries, such as the rupture of the anterior cruciate ligament [Williams05], and can monitor the process of cartilage repair in autologous chondrocyte transplanted (ACT) patients [Gillis01, Vasara05, Kurkijärvi07, Trattinig07b]. Roos and Dahlberg [Roos05] reported the first in vivo evidence that mechanical stimulation of the cartilage can modulate the GAG concentration.

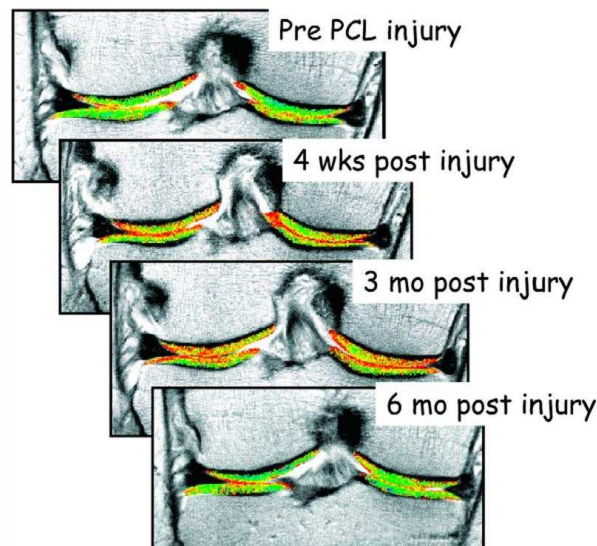


Figure 3.2: dGEMRIC images of the right medial compartment from before and after a posterior cruciate ligament tear showing a drop from the baseline dGEMRIC index at one and three months after the injury and a return to baseline values by six months. (Adapted from [Williams05])

dGEMRIC is a well validated MRI technique for the imaging of the GAG-concentration with potential for the early diagnosis of OA. The principal disadvantage of dGEMRIC is to ensure that $\text{Gd}(\text{DTPA})^{2-}$ is in equilibrium before the imaging session, which requires waiting for 90 minutes after $\text{Gd}(\text{DTPA})^{2-}$ administration for MRI.

3.1.3 $T_{1\rho}$ imaging

$T_{1\rho}$ (the spin-lattice relaxation time in the rotating frame), is the relaxation time measured under the continuous irradiation of a low-power radio frequency (RF) field. This technique was first proposed

in 1955 [Redfield55] in solids, and subsequently extended to liquids [Bull92]. In this method the magnetization is rotated into the transversal plane with a 90° pulse (mostly a short block pulse). Once in the transversal plane, the magnetization relaxes to the longitudinal axis while irradiated with a low-power RF pulse, which continuously refocuses the transversal magnetization. Under these conditions the relaxation is determined by the interactions between macromolecules and bulk water. In cartilage, it is expected that the relaxation is dominated by the PG and collagen content of the cartilage, so that $T_{1\rho}$ is sensitive to early degeneration of cartilage.

The low-power RF pulse effectively locks the magnetization to its initial resonant state, so that the relaxation occurs as if it would occur in the rotating frame. Therefore, the relaxation time, $T_{1\rho}$, is also called “ T_1 in the rotating frame” and the measurement technique is known as spin-lock. The duration of the low-power RF pulse (or spin-lock field) is termed the spin-lock time (TSL) and determines the $T_{1\rho}$ -weighting of the image. The magnetization in the rotating frame decays with TSL following an exponential function,

$$S(\text{TSL}; T_{1\rho}, S_0) = S_0 \exp\left(-\frac{\text{TSL}}{T_{1\rho}}\right) \quad (3.1)$$

where S is the signal intensity after a pulse of duration TSL and S_0 is the signal intensity at zero TSL. To measure $T_{1\rho}$, several (at least two) measurements with different TSL must be performed. $T_{1\rho}$ is calculated with an exponential fit or a linear regression analysis of the measured signal intensities.

In order to obtain $T_{1\rho}$ -weighted images, which can be used to calculate $T_{1\rho}$, the magnetization must be space-encoded. Therefore, the $T_{1\rho}$ -weighted magnetization is first pulled back into the longitudinal axis with a short 90° pulse, so that imaging can be performed with any standard sequence: 2D TSE sequence [Duvvuri01], a 2D FLASH sequence [Regatte03b, Akella03], a 3D FLASH sequence [Borthakur03]...

First studies of $T_{1\rho}$ in the cartilage were performed in vitro on animal specimens. Reddy et al. [Reddy95] reported the first in vitro $T_{1\rho}$ maps of the articular cartilage indicating that the exchange of water molecules with the macromolecules in the cartilage may be responsible for the values of $T_{1\rho}$. Posterior in vitro studies with series of progressively depleted bovine cartilage have demonstrated that $T_{1\rho}$ correlates with the GAG content [Duvvuri97, Akella01, Regatte02]. However, $T_{1\rho}$ seems to have also a dependence on the collagen concentration. At different fields and at different orientations both T_2 and $T_{1\rho}$ showed almost identical spatial distributions, thus indicating a dependence on collagen content [Mlynárik04]. Wheaton et al. [Wheaton04b, Wheaton05] found strong correlations between bulk $T_{1\rho}$ and PG content ($r^2 = 0.93$), and between $T_{1\rho}$ and the mechanical properties ($r^2 = 0.86$) in bovine cartilage explants.

Difficulties to measure $T_{1\rho}$ maps in vivo lie in the long acquisition times needed for imaging and in the limits on the specific absorption rate (SAR) for application in humans. The first $T_{1\rho}$ -weighted images in vivo were acquired on the patella of 5 healthy volunteers and one symptomatic patient using a $T_{1\rho}$ prepared 2D TSE sequence [Duvvuri01]. The lesion on the symptomatic patient presented in $T_{1\rho}$ -weighted images a 25% better contrast to noise than in T_2 -weighted images. Regatte et al. [Regatte03a] published the first $T_{1\rho}$ maps of the human tibial cartilage (Fig. 3.3). In subsequent systematic studies, Regatte et al. [Regatte04, Regatte06] demonstrated in vivo that patients with OA presented increased cartilage $T_{1\rho}$ values compared to healthy controls, and that the $T_{1\rho}$ has a larger dynamic range than T_2 .

Observational evidence indicates that $T_{1\rho}$ is very sensitive to the process of cartilage degradation, although the relaxation mechanism of $T_{1\rho}$ seems to be unspecific. Initially, the application of $T_{1\rho}$

3.2 MRI of the collagen network

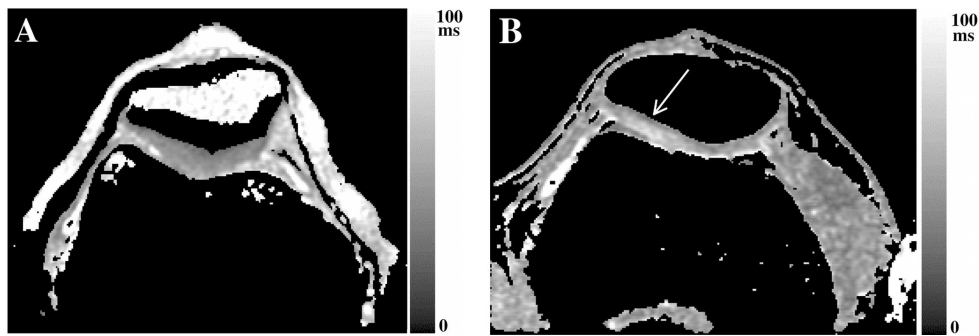


Figure 3.3: A. In vivo transverse $T_{1\rho}$ relaxation maps of the patellofemoral joint in a 30-year-old healthy human volunteer. B. In vivo transverse $T_{1\rho}$ map of the patellofemoral joint in a 40-year-old woman with knee pain. The high signal intensity in the lateral patellar facet (arrow) of cartilage reflects an increase of approximately 45% in $T_{1\rho}$ relaxation time compared with baseline values. The bar scale at the right in B indicates variations in $T_{1\rho}$ relaxation time. (Adapted from [Regatte03a])

in the routine has been hampered by the long imaging time required and the SAR limits. However, recent sequence developments, which overcome these limitations, have approached $T_{1\rho}$ to the clinical routine.

3.2 MRI of the collagen network

3.2.1 T_2 relaxation time

In contrast to the other MRI techniques presented here, which have been specifically applied to cartilage to quantify one of its components, the value of the relaxation time T_2 as a measure of the integrity of the collagen network was partially a matter of serendipity. The unexpected laminar appearance of the cartilage in the first high-resolution MRI studies of the knee, motivated an intense investigation to explain it, which demonstrated the connection between T_2 in articular cartilage and the collagen matrix [Xia00].

Significance of T_2 in the cartilage: The magic-angle effect

Early high-resolution MRI studies of the knee used spin-echo (SE) sequences with TEs larger than 20 ms and reported a homogeneous appearance of cartilage [Reicher85, Burk86, Gylys-Morin87], although a laminar structure of the cartilage could be clearly seen. The first mention of a laminar structure of the cartilage in T_2 -weighted images was a comment in the work of Tyrrell et al. [Tyrrell88]. Lehner et al. [Lehner89] performed the first systematic study of the laminar structure of the cartilage in excised bovine patellae. They used inversion recovery SE and SE sequences to demonstrate that the layers were a consequence of T_1 - and T_2 -weighting of the image. The authors attributed the laminar structure to differences in the relaxation times T_2 and T_1 , water content and histology between the deepest and superficial layers of the cartilage [Lehner89]. Subsequent studies corroborate the laminar structure of cartilage with different sequences (SE [Modl91], 3D gradient echo (GE) [Paul93], fast

imaging with steady precession (FISP) and FLASH [Uhl98]), and tried without great success to correlate the MR laminar structure with the histological findings [Modl91, Cova98, Uhl98, Goodwin98, Goodwin00].

Rubenstein et al. [Rubenstein93] firstly identified “an orientation-dependent T_2 of collagen fibers” as the cause of the laminar appearance of cartilage. Inspired by previous studies, which demonstrated the orientation-dependent signal intensity and T_2 relaxation time in tendons [Berendsen62, Fullerton85, Erickson91], Rubenstein et al. [Rubenstein93] investigated the laminar structure of cartilage in vitro for different positions of the articular cartilage with respect to the external magnetic field. T_1 -weighted SE images of excised bovine cartilage were acquired by varying the orientation of the sample with respect to the magnetic field in increments of 5° (41 increments). A clear peak of the signal intensity at the orientations corresponding to the magic angle was observed. The magic-angle effect is a consequence of the presence of an effective dipolar-dipolar interaction between the water molecules in tissue. If the water molecules cannot move freely (as is the case of the water molecules bound to the collagen fibrils), they experience an effective dipolar-dipolar interaction, which is a very effective mechanism of relaxation. A characteristic of the dipolar interaction is that it depends on the orientation of the water molecules with respect to the external magnetic field. At certain angles, known as the magic-angles (54.7° , 125.3° , 234.7° and 305.3°), the dipolar interaction is effectively zero. At this orientations occurs an increment of the T_2 relaxation time and hence on the signal intensity.

Henkelman et al. [Henkelman94] analyzed the effect of cartilage orientation on T_2 , T_1 , diffusion and magnetization transfer parameters. They found two components in T_2 (a short T_2 of 20 ms and a large T_2 of 55 ms), which changed with orientation. At the magic angle, where the dipolar interaction is less effective, the short T_2 component appeared clearly diminished compared to an orientation of 0° .

The first imaging study which quantitatively analyzed the variation of T_2 and T_1 with the orientation was performed by Xia [Xia98]. High-resolution ($14 \mu\text{m}$) T_2 and T_1 maps of excised canine cartilage were obtained at different angles to the normal of the articular surface and the external magnetic field (-35° , 3° , 25° , 40° , 57° and 85°). No orientation dependence of T_1 was found, but a clear orientation dependence of T_2 was observed in the deep radial and the tangential zones, where the collagen fibrils demonstrate greater organization (Fig. 2.3). No significant change of T_2 with the orientation was found in the transitional zone, where the cartilage shows almost random orientation of the collagen fibrils (Fig. 2.3). In a posterior study Xia et al. [Xia01] demonstrated that the transitional zone in T_2 profiles correlates with a zone of smooth variation in polarized microscopy. Nieminen et al. [Nieminen01] found in bovine cartilage a good correlation between high-resolution T_2 profiles and the inverse of the birefringence index measured with polarized-light microscopy, thus demonstrating a close connection between the laminar T_2 structure and the collagen architecture. The magic angle effect has been estimated in vivo on sagittal T_2 maps of the femur [Mosher01]. A maximal increase in T_2 of 29.1% at the magic angle was found at the articular surface. However, this estimation relayed on the assumption of an uniform structure throughout the complete cartilage.

Measurement of T_2 in the cartilage

The standard method for T_2 calculation is to acquire several (at least two) SE images at different echo times TE, and fitting the signal intensity at different TEs to a model, which for most applications is a

3.2 MRI of the collagen network

mono-exponential function (see 4.1).

The SE sequence offers the methodological advantage that all lines in k -space are acquired exactly at the same TE. However, the SE sequence requires long acquisitions times, since the repetition time, TR (i.e. the time between the acquisition of two lines in k -space), must be of the order of five times the relaxation time T_1 , in order to allow complete relaxation of the magnetization to its initial state (and thus maximal signal), before the new excitation. Since the typical T_1 values in the cartilage are of the order of 1 s, the TR in a SE sequence should be of the order of 5 s. Due to the high resolution necessary to resolve the cartilage, which has a thickness of 2–4 mm, the matrix-size of the images should be at least 256 with a field of view (FOV) around 15 cm to avoid aliasing (isotropic in-plane resolution of about 0.6 mm). That means a total acquisition time of approximately $256 \times 5 \text{ s} \approx 21 \text{ min}$ for one TE, and 2:40 h for 8 different TEs.

The acquisition of the same line in k -space at different TEs can be performed one after the other by consecutive refocusing of the transversal magnetization with a train of 180° pulses. This technique, called multi-echo, allows the complete acquisition of all the images at different TEs of one slice in only 21 min. For further reduction of the measurement time, multi-echo acquisitions of several slices can be performed in an interleaved manner, thus optimally using the large TR. To avoid any cross-talk effect between the slices, an even-odd interleaved acquisition scheme of the slices is recommended. This method is known as multi-slice and the sequence which combines multi-echo and multi-slice techniques is called multi-slice multi-echo (MSME, Fig. 3.4). A MSME sequence can acquire 20 slices at 8 different TEs in only 21 min. The scanning time can still be accelerated if partial acquisition of the k -space is performed with partial Fourier or parallel imaging. However, due to the SNR limitations (especially in the later echoes) only a partial Fourier factor of 6/8 or an iPAT factor of two can be applied.

The use of MSME sequences however are tied with some problems, which can result in significant bias of the calculated T_2 values. The first problem is the formation of stimulated echoes due to the impossibility of obtaining perfect 180° inversion profiles [Schick97]. Stimulated echoes occur in an echo train when a fraction of the transversal magnetization is rotated back to the longitudinal axis by an imperfect 180° pulse and subsequently pushed back into the transversal plane by a posterior 180° pulse in the echo train. Since between the two 180° pulses the magnetization decays with T_1 , stimulated echoes have a mixed T_2 - and T_1 -weighting, which results in artificially lengthened calculated T_2 values.

There are two possibilities to correct a MSME sequence from stimulated echoes. One possibility is to use crusher gradients of variable amplitude around the 180° pulses within the same echo train [Poon92] (Fig. 3.4). In SE sequences crusher gradients are used to avoid spurious free-induction-decay signal coming from the tilting of any residual longitudinal magnetization (after imperfect 90° excitation), into the transversal plane by 180° pulse. Any residual longitudinal magnetization rotated into the transversal plane by an imperfect 180° pulse, will be dephased by the crusher gradient *after* the 180° pulse, so that it will not produce any signal. The transversal magnetization, which is correctly inverted, is first dephased by the crusher gradient before the 180° pulse and after inversion rephased by the second crusher gradient. In multi-echo sequences crusher gradients are required around each 180° pulse, but using the crusher gradients of the same amplitude in each 180° pulse is unfavorable. If a stimulated echo occurs, it will be dephased by the first crusher gradient of the 180° pulse, which rotates it into the longitudinal direction, and rephased by the crusher gradient after the 180° pulse, which pull it back to the transversal plane. If the amplitude of those crusher gradients are different the

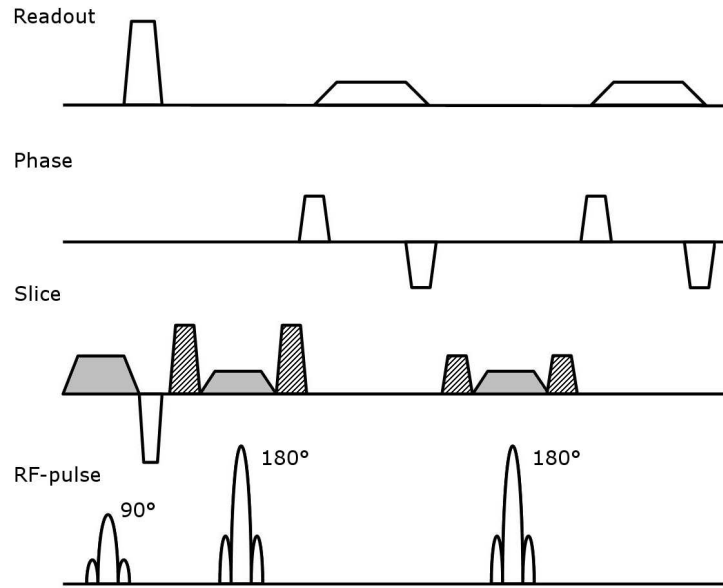


Figure 3.4: Diagram of a MSME sequence with two different echo times. Pulse gradients are represented in all three spatial directions (encoded as readout, phase and slice). At the bottom are represented the RF pulses. The dashed pulse gradients are the crusher gradients and the gray pulse gradients are the slice selection gradients. Note the implementation of the mechanisms for stimulated echo suppression: Crusher gradients and slice selection gradients of different heights.

stimulated echo would not be rephased and it will not contribute to the signal. The second possibility of reducing stimulated echoes is to use 180° pulses with a slice thickness 1.2 times larger than the slice thickness of the 90° pulse to achieved a more homogeneous inversion profile over the excited magnetization in slice direction (Fig. 3.4).

A second problem of MSME sequences for T_2 calculation is the increasing diffusion-weighting along the echo train, which causes a signal loss additionally to the T_2 weighting. Therefore, fitting the measured points to a signal-model (mostly mono-exponential) would result in underestimation of T_2 . However, the underestimation of T_2 is much smaller than the measurement errors due to the low SNR as demonstrated in Section 4.4.3. Although multi-slice sequences are also influenced by magnetization transfer effects, they do not alter the measured T_2 since the magnetization transfer effectively reduces the S_0 without altering the exponential decay of the signal [Yao96, Mendlik04].

All measurements of the T_2 relaxation time included in this thesis are acquired with a self-developed MSME sequence including the two corrections explained above [Mendlik04]. The T_2 values measured with the MSME sequence were compared with the T_2 values calculated with the much more time consuming SE sequence. On excised human patellar cartilage the MSME sequence showed a mean underestimation of 8% respect to the T_2 values measured with the SE sequence [Mendlik04]. In all in vivo images included in the present work the MSME sequence parameters were kept constant (TR=3000 ms, initial TE=13.2 ms, 8 echoes, echo spacing 13.2 ms, FOV=160×160 mm²,

3.2 MRI of the collagen network

matrix=256×256, acquisition time=12:48 min). Image resolution was 0.625×0.625×3 mm³.

Studies of T_2 in the cartilage

The characteristic appearance of the cartilage in T_2 -weighted images is a consequence of the orientation of the collagen fibrils in the external magnetic field. Water molecules bind to the collagen fibrils in different layers [Fullerton85, Bella94], so that the dipolar interaction between them do not average to zero. The dipolar interaction depends on the orientation to the magnetic field and is a very effective mechanism of T_2 relaxation, which is responsible for the short T_2 relaxation times in cartilage and tendons.

If the collagen network becomes degraded its ability to bind water decays, so that the water molecules can move more freely, thus decreasing the dipolar interaction they experienced and leading to an increase in T_2 relaxation time, which can be measured with MRI. The diagnosis of pathological changes in the collagen matrix is a very important question, since degradation of the collagen matrix is considered to be an entry point in the process of irreversible joint degradation [Bank00].

The first in vivo T_2 maps of the human cartilage were acquired on the patellar cartilage of 6 healthy and 1 symptomatic volunteers by Dardzinski et al. [Dardzinski97]. With a MSME sequence without correction of stimulated echoes, Dardzinski et al. found increasing T_2 values from the bone-cartilage interface (32 ms) to the articular surface (76 ms), as expected from the orientation of the collagen fibrils with respect to the magnetic field. The symptomatic patient examined in this study showed increased T_2 values of 55-70 ms in the deep radial and transitional zones. In a posterior study, 32 healthy and 6 symptomatic volunteers were examined to analyze the change in T_2 with age and early OA [Mosher00]. The population over 45 y presented a significant increase of the T_2 in the most superficial 25% of the cartilage compared to the population under 45 y [Mosher00, Mosher04b]. In symptomatic volunteers, a significant ($P < 0.05$) increase in T_2 was found, which presented three different patterns: small focal areas of increased T_2 , heterogeneously increased T_2 and a locally increased T_2 associated with a tear [Mosher00].

Several studies have investigated the ability of T_2 to predict the grade of OA. In a first multiparametric study, Mlynárik et al. [Mlynárik99] investigated the value of T_1 , T_2 and dGEMRIC in vivo to assess the integrity of cartilage in patients prior to complete joint replacement. Mlynárik et al. did not find the expected increase of the T_2 relaxation time. However, they observed that T_2 was increased in regions of cartilage fibrillation. David-Vaudey et al. [David-Vaudey04] performed an in vitro study on fresh human cadaveric knees. Cartilage samples from different locations of the patellar, femoral and tibial cartilage were imaged at 1.5T for T_2 calculation. After imaging, cartilage samples underwent histology and polarized light microscopy. T_2 values showed a positive correlation with the OA grade as assessed by histology.

In vivo the relationship between radiological diagnosed OA and T_2 has been investigated on 55 volunteers with diverse OA grade [Dunn04]. The grade of OA in all 55 volunteers was assessed with plane radiographs and classified in healthy ($n = 7$, Kellgren-Lawrence = 0), mild OA ($n = 20$, Kellgren-Lawrence = 1–2) and severe OA ($n = 28$, Kellgren-Lawrence = 3–4). Significantly larger bulk T_2 values were found in the volunteers affected by OA compared to the healthy population. However, no significant difference in T_2 could be seen with OA grade. A poor correlation of T_2 with the radiographic grading of OA was found on 113 symptomatic volunteers [Koff07]. However, a significant ($P < 0.037$) relationship between T_2 and molecular biomarkers for OA (serum cartilage oligomeric

3 MRI of articular cartilage

matrix protein and cleaved collagen neopeptide) in male symptomatic patients was reported [King04].

In clinical routine, quantitative T_2 mapping has been revealed to be more sensitive for the detection of focal lesions than the standard MRI protocol [Hannila07]. Twenty-eight lesions were detected both on MRI and T_2 maps, while eight lesions were only visible on T_2 maps. Even more, the lesions appeared significantly wider and thicker in T_2 than in standard images. A crucial point for the diagnostic value of T_2 is how reproducible T_2 measurements are. Therefore, much effort has been invested in the study of the T_2 reproducibility in cartilage [Glaser05, Glaser07, Schneider08, Welsch08c, Koff09]. Reproducibility is normally characterized by the coefficient of variation (CV), which is the ratio in percent between the standard deviation and the mean value. Bulk T_2 times showed CVs between 3% and 7% at 1.5 T [Glaser05, Glaser07] and between 3.2% and 4.7% at 3 T [Glaser07, Welsch08c]. In a multi-centre study global T_2 reproducibility at 3 T varied longitudinally over 3 years from 2.3 to 18.8% [Schneider08]. Regional reproducibility showed clear variations across the cartilage with mean value of 8.62% at 1.5 T [Glaser05] and 9.66% at 3 T [Glaser07]. Voxel-based reproducibility with the method presented in Chapter 5 showed only slightly worse CVs between 7% and 18% [Raya09].

The value of T_2 in monitoring the disease progression has been investigated in OA and autologous chondrocyte transplanted (ACT) patients (Fig. 3.5). In a 2-year longitudinal study with OA patients Blumenkrantz et al. [Blumenkrantz04] observed a significant ($P < 0.05$) increment of bulk T_2 in all cartilage compartments with the exception of the tibial plateau. In a 1-year follow-up study [Stahl07], the tibial and femoral cartilage of 8 OA female patients with body mass index greater than 30 were observed with MRI at 3, 6, 9 and 12 months after baseline MRI. No differences of the bulk T_2 of the tibial and femoral cartilage was observed with respect to an 8 age-matched healthy volunteers, although significantly higher T_2 was found in OA patients than in age-matched healthy volunteers was found.

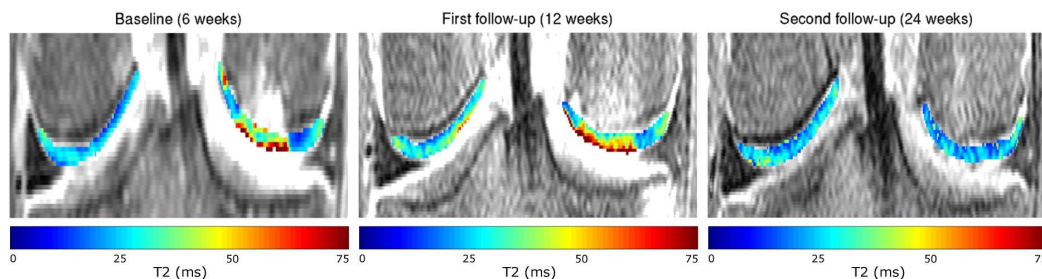


Figure 3.5: Follow-up examinations on a 39-year-old patient after MACT transplantation in the right knee. From left to right, T_2 maps of examinations at 1.5, 3 and 6 months after intervention. Observe the reduction of T_2 in the examination at 6 months, which indicates healing of the lesion. MRI images has been stretched to improve visibility of the cartilage.

ACT lesions can be monitored with the T_2 relaxation time, since the collagen network of the implanted allografts is unordered, so that the lesion initially present large T_2 values, which decrease in the process of healing. In 2-year follow-up examinations of ACT patients the mean T_2 in allografts is increased compared to the T_2 values measured in a healthy collective in the first year, and equals the healthy values in the second year [Trattng07a]. Welsch et al. [Welsch09] examined 15 ACT trans-

3.3 MRI methods sensitive to proteoglycan and collagen

planted patients in two-year follow-up examinations. Mean T_2 values over the complete cartilage were not sensitive to the process of healing, but zonal variations in the lesion could be used for monitoring. After surgery, T_2 appears homogeneous, but following healing progressive zonal stratification was observed [Welsch09].

Since T_2 is the only easily accessible MRI parameter sensitive to the organization of the collagen network, an increasing number of studies simultaneously measured T_2 and PG-sensitive MRI parameter (dGEMRIC, $T_{1\rho}$...) to completely assess the integrity of the extracellular matrix. One of the best candidates to combine with T_2 is dGEMRIC, although attention must be paid to the effect of $\text{Gd}(\text{DTPA})^{2-}$ in the shortening of T_2 . Nieminen et al. [Nieminen04, Kurkijärvi08] demonstrated that at low field (1.5 T) the concentrations of $\text{Gd}(\text{DTPA})^{2-}$ do not significantly shorten T_2 , so that both parameters can be measured in the same imaging session. First in vivo study on ACT-transplanted patients demonstrated that 10–15 months after surgery, ACT grafts showed significantly longer T_2 values for bulk tissue as well as for the superficial 50% and deep 50% of tissue as compared to control cartilage. However, dGEMRIC assessment in the sagittal and coronal directions did not show significant differences [Kurkijärvi07].

Another possibility is to combine T_2 with $T_{1\rho}$, which is sensitive to the PG content. Regatte et al. [Regatte06] compared T_2 and $T_{1\rho}$ in patients which underwent total joint replacement. Both T_2 and $T_{1\rho}$ were larger in patients than in healthy volunteers, however $T_{1\rho}$ demonstrated a wider range of change. In patients, T_2 increased between 5% and 50% whereas $T_{1\rho}$ increased between 30% and 120%.

In conclusion, T_2 is the only easily accessible MRI parameter that is mainly sensitive to the organization of the collagen matrix. T_2 demonstrated a great potential for the early diagnosis of the degradation of the collagen network, which is considered as an entry point on the irreversible process of cartilage degradation. Both in vitro and in vivo studies showed that T_2 increased in OA. However, a principal disadvantage of T_2 is the relatively long acquisition time of MSME sequences, which may restrict its use in clinical routine.

3.3 MRI methods sensitive to proteoglycan and collagen

3.3.1 Quantitative measurements of cartilage morphology

Since in OA the cartilage suffers a progressive degradation affecting its morphology, quantitating the changes in morphology of cartilage can be used to monitor OA. Morphology quantitation include measurement of the cartilage volume and thickness, assessment of the area of the articular surface and the bone-cartilage interface, denuded subchondral area, lesion size, ...

In order to quantitate the morphology of the cartilage, high-resolution images (standard resolution is $0.3 \times 0.3 \times 1.5 \text{ mm}^3$), are required with a good contrast between cartilage and adjacent tissues. Nowadays, the most used sequences are FLASH with water excitation and fat-suppressed T_1 -weighted spoiled gradient echo (SPGR) [Eckstein06a]. Suppressing the fat signal improves the contrast at the bone-cartilage interface and avoids chemical shift artifacts, which can bias the measurement of volume and thickness. Sequences for cartilage morphology must be carefully optimized by balancing the image resolution, the acquisition time and the contrast-to-noise ratio at the articular surface and the bone-cartilage interface.

To derive quantitative data the cartilage must be first segmented. Cartilage segmentation is a diff-

cult task, especially in OA patients, where the denuded subchondral bone must be segmented and the osteophytes be avoided. Therefore, all attempts to fully automate the segmentation did not produce the desirable results in OA patients. Thus, only semi-automatic segmentation algorithms, like the one used in this work [Hohe02], are used in the praxis.

After segmentation, quantitation of the morphology can be performed. Volume is straightforward to calculate but it is not a valuable indicator for the integrity of the cartilage, since it depends both on how large the bone-cartilage interface is and how thick the cartilage is. Therefore, the mean thickness or the thickness distribution are more sensitive to the detection of local defects. However, the calculation of these parameters require more image processing [Stammberger99, Raya06].

Since OA has a long natural history, which spreads over several years, a very important issue is the accuracy (deviation of the measured values in average from the exact value), and precision (spread of the values) of the quantitative morphology parameters. The accuracy of volumetric and thickness measurements has been studied in cadaveric samples and in patients who underwent a complete joint arthroplasty. Most of the studies reported non-significant differences between the parameters measured with MRI and other invasive methods [Eckstein96, Eckstein98a, Cohen99, Cicuttini00]. Typical differences between MRI and other invasive methods were in the range from 3.8% to 9.2% for the cartilage volume, from 2.5% to 8.4% for the thickness and from 5.1% to 17.4% for the mean thickness.

Precision has been extensively analyzed with repeated acquisitions on the same volunteer. The precision is characterized with the CV. CVs for the cartilage volume vary from 0.8% and 8.2% depending on the sequence used, the resolution and the cartilage examined [Glaser03, Eckstein06b]. Long-term precision examined on healthy volunteers in a period of 9–12 months was not significantly larger than short-term precision [Eckstein02]. The precision of the cartilage thickness (regional, maximum and averaged) varied between 1.6% and 8.9% [Koo05, Eckstein05, Inglis07, Wirth08].

Cartilage loss has been measured with follow-up examinations of OA patients over several years [Cicuttini01, Cicuttini02, Wluka02, Cicuttini04b, Raynauld08, Eckstein08a]. The rate of cartilage loss varied from one cartilage to the other. The patellar cartilage showed the lowest rate of cartilage loss, -4.1%/y, the tibial cartilage presented rates of -5.6%/y (lateral) and -6.0%/y (medial) and the largest rates were found for the femur with -8.7%/y (lateral) and -7.6%/y (medial).

The correlation of cartilage loss and other nonradiological parameters (weight, muscle mass, ...), has provided valuable information about the risk factors and evolution of OA. Tibial cartilage loss is significantly correlated with a loss of muscle mass and is three times higher in patients with meniscal extrusion [Cicuttini05]. Cartilage loss is also related with the pain scores and body-mass index [Wluka02, Hunter03], and seems to predict the risk of undergoing total knee arthroplasty [Cicuttini04a]. A positive correlation of the misalignment of the cartilage with the loss of cartilage has been reported [Eckstein08b]. The use of quantitative morphological parameters can be combined with dGEMRIC, thus complementing the morphological information with biochemical information about the PG [Eckstein09].

Quantitative morphology, principally based on quantification of cartilage volume and thickness, is a robust and well-established technique for measurement of cartilage degradation in OA. This technique is not specifically sensitive to any component of the cartilage matrix, so that it has low potential to detect early degenerative changes. However, the application of quantitative morphology to large cohorts of OA patients has resulted in valuable information about the risk factors influencing OA.

3.3 MRI methods sensitive to proteoglycan and collagen

3.3.2 Diffusion tensor imaging (DTI)

Diffusion-weighted imaging (DWI) has proven to be a valuable method to trace the tissue microscopic structure. This technique is based on the tissue-dependent signal attenuation caused by incoherent thermal motion of water molecules (Brownian motion). Changes of the mobility of water molecules in biological tissue can be detected in various pathologic conditions. Initially, DWI was successfully applied to neuroradiological settings [Le Bihan86]. The first confirmation of its diagnostic possibilities was in the assessment of acute stroke, which DWI can detect within minutes of its onset [Mintorovitch91]. DWI has also demonstrated a great potential in the differentiation of benign and malignant acute vertebral fractures [Baur98, Raya05, Raya06, Raya07].

To quantitatively determine the diffusivity in tissue (also known as the apparent diffusion coefficient, ADC), a method proposed in 1965 by Stejskal and Tanner [Stejskal65] as pulsed-gradient spin echo measurement is used for almost all diffusion-sensitized pulse sequences. The idea is to perform a position-dependent dephasing and rephasing of the spins using two identical gradients, the so-called diffusion gradients, at both sides of a refocusing RF pulse. Since diffusing spins are always in motion the phases acquired during dephasing and rephasing (i.e. during the first and second diffusion gradient) do not compensate and diffusing spins will only partially contribute to the signal intensity, showing an attenuation which depends on their mobility. Spins with a large diffusivity scarcely contribute to the resulting signal intensity, whereas spins with small diffusivity will show only little attenuation. Indeed, with this simple method the signal intensity shows an exponential dependence on the ADC,

$$S(b; S_0, \text{ADC}) = S_0 \exp(-b \times \text{ADC}), \quad (3.2)$$

where $S(b; S_0, \text{ADC})$ is the intensity in the presence of the diffusion gradients, S_0 the signal without diffusion gradients and b is the so-called b -value,

$$b = (\gamma g \delta)^2 (\Delta - \delta/3), \quad (3.3)$$

which depends on the gyromagnetic ratio γ , and on diffusion gradient parameters: their amplitude, g , their duration, δ , and the separation time between the onset of the two diffusion gradients, Δ . In order to obtain a purely diffusion-weighted image, it is necessary to explicitly calculate the diffusivity. This can be easily performed due to the exponential dependence of the signal intensity on the ADC Eq. [3.2]. First, several (at least two) images of the same slice are acquired with different b -values. Then the ADC is calculated with an exponential fit or a linear regression analysis either using the mean intensity of a region of interest or pixel-by-pixel. In the latter case, the resulting image, in which each pixel contains an ADC, is the so-called ADC map.

The diffusion gradients introduced above have a certain spatial orientation, and only the component of the molecule motion parallel to this gradient direction causes a signal attenuation in the corresponding diffusion-weighted image. By varying the direction of the diffusion gradients it is possible to calculate the ADC in different directions. A complete description of the spatially varying diffusivity is given by a symmetric 3×3 matrix of diffusion coefficients called the diffusion tensor [Le Bihan01]. The imaging technique used to measure the diffusion tensor is known as the diffusion tensor imaging (DTI). The most important properties derived from the diffusion tensor are the mean diffusivity averaged over all spatial orientations (trace of the tensor), the diffusion anisotropy as a measure of the orientational differences of diffusivity (the most broadly parameter is the fractional anisotropy (FA)), and the eigenvector associated to the largest eigenvalue, which indicates the preferred direction of diffusion.

3 MRI of articular cartilage

The value of ADC as a marker for OA is largely known. First invasive measurements of the diffusion in cartilage were performed by Maroudas et al. [Maroudas68, Maroudas77], which obtained mean ADCs in healthy cartilage of $1.37 \times 10^{-3} \text{ mm}^2/\text{s}$ and $1.45 \times 10^{-3} \text{ mm}^2/\text{s}$ in OA cartilage at 37°C . First ADC maps in cartilage demonstrated an increment on diffusivity from the bone-cartilage interface to the articular surface an resulted in bulk ADC values of $1.45 \times 10^{-3} \text{ mm}^2/\text{s}$ at 24°C [Xia94], and $1.42 \times 10^{-3} \text{ mm}^2/\text{s}$ at 25°C [Henkelman94].

Henkelman et al. [Henkelman94] were the first who analyze the effects of anisotropy in diffusion. They did not perform standard DTI measurements, but rotated the sample in the magnet field. Interestingly, they did not report any “angular dependence” in cartilage, probably because they only performed spectroscopic measurements. In spectroscopic measurement the signal coming from different parts of the cartilage with different collagen structures and therefore with different anisotropies is averaged. However, posterior DTI studies have demonstrated an evident diffusion anisotropy in human [Filidoro05, Deng07] and bovine cartilage [Meder06, Visser08a] (Fig. 3.6). Filidoro et al. [Filidoro05] demonstrated that the first projection vector on the image plain showed a distinct zonal pattern, being oriented tangentially and radially in the upper and lower portions of the cartilage, respectively. These findings were corroborated in human [Deng07] and bovine cartilage [Meder06, Visser08a]. DTI showed good correlation with scanning electron microscopy on human samples [Filidoro08] and with polarized-light microscopy in bovine patellar cartilage [Meder06, Visser08a].

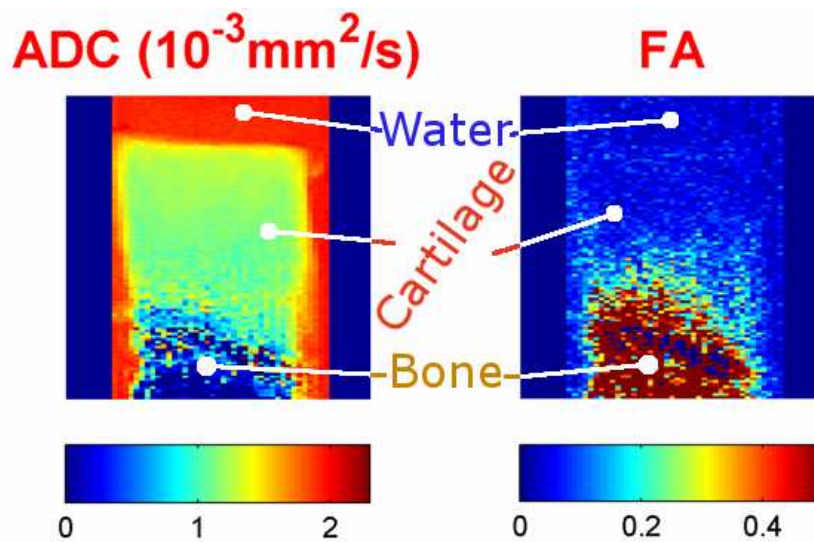


Figure 3.6: Example of a ADC and FA maps acquired at 17.6 T on a sample of the patellar cartilage of a healthy 23-years-old donor. ADC slightly decreased from the articular surface to the bone-cartilage interface. Mean ADC over the sample was $1.15 \times 10^{-3} \text{ mm}^2/\text{s}$. FA decreases from the bone-cartilage interface to the articular surface.

There are two studies which have investigated the effect of trypsin degradation of the cartilage on DTI. An increase of ADC across the complete cartilage depth was observed after PG depletion,

3.4 Emerging techniques

but no significant change in FA was observed. Experiments performed under strain showed reduced ADC and FA under the indenter and re-arrangement of the first eigenvector parallel to the surface of the indenter [Raya08c, Visser08b]. In human articular cartilage significant increased ADCs were observed with increasing OA grade [Raya08b].

DTI of the cartilage gives information about both the PG content and the collagen structure and is sensitive to the process of cartilage degradation. However, its application in vivo faces many difficulties, principally due to the large acquisition times needed to acquire a DTI dataset. Reduction of the scanning time with rapid-acquisition techniques (such as DW-HASTE or DW-EPI sequences) seems unlikely due to the high resolution needed to meaningfully resolve the cartilage, the complex anatomy of the knee with much tissue interfaces causing susceptibility jumps and the low T_2 values in the cartilage.

3.4 Emerging techniques

For the sake of completeness, some recently proposed techniques are briefly discussed. These techniques have potential for the early diagnosis of cartilage degradation, although more experimental evidence is needed to ultimately demonstrate their utility.

3.4.1 Ultra-short echo time MRI

In the calcified and deep radial zones of articular cartilage the T_2 relaxation time has two components, a fast T_2 component of less than 5 ms and a slow T_2 component of around 30 ms. In the calcified zone the fast component represents approximately 80% of the signal [Shinar06]. Imaging of the bone-cartilage interface may be of clinical relevance since micro-fractures in the calcified zone may play an important role in the pathogenesis of OA [Imhof00].

MRI of the calcified and deep radial zones requires ultra-short echo times (UTE) sequences with TEs as short as 0.08 ms (80 μ s). To achieve these extreme short TEs, UTE sequences use a partitioned excitation, which does not require the slice rephasing gradient, and a half-radial acquisition of the k -space, which avoids the readout dephasing gradient prior to the echo readout [Robson03, Robson06]. In UTE images, the calcified zone of the cartilage appears very bright [Gatehouse04b] (Fig. 3.7).

The UTE sequences have also great potential for the imaging of all tissues with very low T_2 such as the menisci ($T_2 = 5-8$ ms), ligaments ($T_2 = 4-10$ ms), bone ($T_2 = 0.5$ ms), ... [Bydder09]. With this technique it was possible to differentiate the red and white zone of the menisci [Gatehouse04a]. This may have important consequences for the surgical planning to repair tears, since those in the red zone show much greater capacity of healing.

UTE sequences are promising for the imaging of the bone-cartilage interface. However, UTE sequences are tied to some problems such as the inefficient sampling of the k -space and their limitability on many systems. The potential for diagnosis of OA in the cartilage must still be demonstrated.

3.4.2 gagCEST MRI

Recently, Ling et al. [Ling08] proposed a novel technique for the selective imaging of PG in articular cartilage. The method bases in the chemical-exchange-dependent saturation transfer (CEST) technique. In this technique the -NH and -OH spins of the GAG are saturated and the saturation is

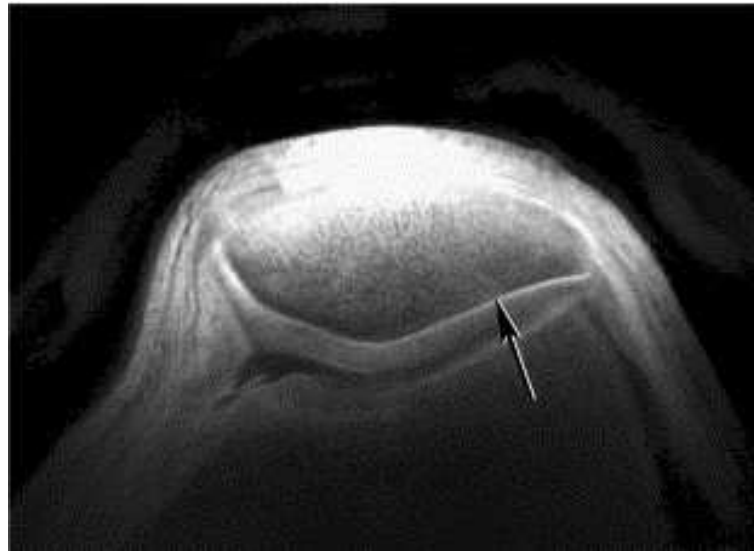


Figure 3.7: UTE image of the patellar cartilage in a healthy volunteer. The arrow indicates the bright line at the bone-cartilage interface, due to the low T_2 component. (Adapted from [Gatehouse04b]).

transferred to the bulk water in cartilage, thus allowing a great contrast enhancement. The gagCEST method has been validated in a series of measurements on trypsin-depleted cartilage. Excellent correlation was found with the GAG concentration measured with ^{23}Na -MR. In one patient with occasional knee pain, gagCEST MRI clearly demonstrated PG loss.

Chapter 4 T_2 calculation in conditions of low SNR

Spin echo images for T_2 calculation in articular cartilage are inherently affected from low SNR due to the high resolution needed to meaningfully resolve the structure of cartilage and its short T_2 times (between 10 and 50 ms). High resolutions in acceptable acquisition times can only be achieved at the cost of SNR. On clinical 1.5 T scanners in-plane resolutions of $0.6 \times 0.6 \text{ mm}^2$ with acquisition times around 10 min are standard.

The measurement of the low T_2 in cartilage requires using short TE, in order to appropriately sample the rapidly decaying signal intensity. The shortest achievable TE in SE sequences is of the order of 10 ms due to the minimum pulse duration necessary to obtain a good slice profile and the low bandwidth (of a few hundred Hz/pixel) required to keep the SNR as large as possible. Even more, since the largest TE should be at least a 1.3 times [Jones96] of the largest T_2 to be accurately measured (approximately 50 ms), the signal of the voxels with short T_2 times at the later echoes is dominated by noise.

High noise levels seem to be an unavoidable element in the measurement of T_2 in articular cartilage. In magnitude reconstructed images, which are the images usually used in MRI, the noise distribution in the absence of signal has a nonzero mean, so that the measured (noisy) signal intensity never decays towards zero when $TE \gg T_2$. Therefore, calculating T_2 by fitting the measured signal to an exponential function, which decays toward zero, may result in significant overestimation of the short T_2 times of the cartilage.

The purposes of this chapter are to establish a method for T_2 calculation from low-SNR images with minimal possible errors and to assess the impact of the fitting method on T_2 values calculated from in vivo images of articular cartilage. These objectives are achieved in the following steps:

1. Two new noise-corrected methods for pixelwise T_2 calculation are introduced.
2. The accuracy and precision of the two new methods and the most frequently used fit methods (linear least-squares regression and nonlinear fit to an exponential), are tested with simulations and in phantom measurements.
3. The differences between the fit methods in the evaluation of in vivo images are assessed.

4.1 Theory

4.1 Theory

The standard method for T_2 calculation is to acquire several (at least two) SE images at different TEs, and fitting the signal intensity to a model. In the absence of noise the signal intensity, S , of a magnitude reconstructed SE image of a homogeneous system decays with TE following a monoexponential function [Abragam04],

$$S(\text{TE}; S_0, T_2) = S_0 \exp\left(-\frac{\text{TE}}{T_2}\right), \quad (4.1)$$

where $S(\text{TE}; S_0, T_2)$ is the noise-free signal intensity at the echo time TE and S_0 is the noise-free signal intensity at zero TE.

Due to the presence of noise, the measured signal intensity, S_M , is a random variable whose possible outcomes are determined by a probability density function $P_{S_M}(S_M|S, \sigma)$, which depends both on the noise-free signal intensity, S , and the standard deviation of noise, σ . The concrete form of $P_{S_M}(S_M|S, \sigma)$ is determined by the image acquisition (noise generated by the electronics and the object being imaged, the coil used...) [Rice54, Henkelman85, Holden86, Gudbjartsson95, Constantinides97, Dietrich08] and by the image reconstruction (use of filters on the raw data, use of parallel imaging...) [Dietrich08]. If the images are acquired with a single-channel coil and without using any partial acquisition of the k -space or filtering, as all images included in this thesis actually are, $P_{S_M}(S_M|S, \sigma)$ can be analytically calculated from the noise distribution of complex MRI raw data.

Both the real and imaginary parts of the raw data are affected by Gaussian white noise. Fourier transformation of raw data leads to complex image data, \mathbf{S}_M , which are the noise-free complex signal intensity, \mathbf{S} , superimposed with Gaussian white noise, \mathbf{n} , of standard deviation σ , $\mathbf{S}_M = \mathbf{S} + \mathbf{n}$. In MRI, it is a common practice to work with magnitude images. Using the polar representation of the complex numbers \mathbf{S} , $\mathbf{S} = S \exp(i\theta)$, and \mathbf{n} , $\mathbf{n} = n \exp(i\phi)$, the magnitude of \mathbf{S}_M takes the form,

$$S_M^2 = S^2 + 2Sn \cos(\phi - \theta) + n^2, \quad (4.2)$$

where the variables $n \in \mathbb{R}^+$ and $\phi \in [0, 2\pi)$ are random variables with probability density functions,

$$P_n(n|\sigma) = \frac{n}{\sigma^2} \exp\left(-\frac{n^2}{2\sigma^2}\right), \quad P_\phi(\phi) = \frac{1}{2\pi}. \quad (4.3)$$

$P_{S_M}(S_M|S, \sigma)$ is calculated by summing the probability $P_n(n|\sigma)P_\phi(\phi)$ over all values of n and ϕ satisfying Eq. [4.2] for a particular choice of S_M and S , and results in a Rician distribution [Rice54, Henkelman85, Holden86, Gudbjartsson95, Dietrich08],

$$P_{S_M}(S_M|S, \sigma) = \frac{S_M}{\sigma^2} \exp\left(-\frac{S_M^2 + S^2}{2\sigma^2}\right) I_0\left(\frac{S_M S}{\sigma^2}\right), \quad (4.4)$$

where I_ν represents the modified Bessel function of the first kind of ν -th order [Olver72].

For large SNR, $P_{S_M}(S_M|S, \sigma)$ approximates a Gaussian probability distribution with mean value S and standard deviation σ , but as SNR decreases $P_{S_M}(S_M|S, \sigma)$ shifts, so that S_M deviates on average from S . Indeed, at vanishing S , $P_{S_M}(S_M|0, \sigma) = P_n(S_M|\sigma)$, the probability of correctly measuring the noise-free signal intensity (i.e. that $S_M=0$), is zero, the most probable value of S_M is σ and S_M has a mean of $\sigma\sqrt{\pi/2}$ and a standard deviation of $\sigma\sqrt{2-\pi/2}$. Thus, the statistics of regions with $S=0$ allow determining the value of σ .

4 T_2 calculation in conditions of low SNR

For long TE, as S approaches to zero, S_M varies randomly around $\sigma\sqrt{\pi/2}$ and never becomes zero ($P_n(0|0, \sigma) = 0$). Therefore, the decay of S_M with TE is no longer described by an exponential function. Thus, to correctly calculate T_2 , S_M should be fitted to a function describing appropriately its decay with TE, which cannot be the noise-free decay Eq. [4.1]. The main idea of this chapter is to use the function describing the decay of the mean value of S_M with TE as the signal model to fit S_M . The noise-corrected signal intensity, $\Sigma(S, \sigma)$, is defined as the average of S_M for a given S and σ ,

$$\Sigma(S, \sigma) = \int_0^\infty dS_M S_M P_{S_M}(S_M|S, \sigma). \quad (4.5)$$

$\Sigma(S, \sigma)$ can be calculated for the Rician distribution (Eq. [4.4]) [Gudbjartsson95, Dietrich08],

$$\Sigma(S, \sigma) = \sqrt{\frac{\pi\sigma^2}{2}} \exp(-\alpha) \left((1 + 2\alpha) I_0(\alpha) + 2\alpha I_1(\alpha) \right), \quad (4.6)$$

where $\alpha = \left(\frac{S}{2\sigma}\right)^2$. The substitution of the noise-free exponential (Eq. [4.1]) in the definition of $\Sigma(S, \sigma)$ (Eq. [4.6]), results in a noise-corrected exponential function, $\Sigma(\text{TE})$, which describes the decay of the mean value of S_M with TE (Fig. 4.1). For nonlinear fit methods it is convenient to have the derivative of $\Sigma(\text{TE})$ with respect to T_2 and S_0 [Olver72],

$$\begin{aligned} \frac{\partial \Sigma(\text{TE})}{\partial T_2} &= \frac{\partial \Sigma}{\partial S} \frac{\partial S}{\partial T_2} = \frac{\partial \Sigma}{\partial S} \frac{S_0 \text{TE}}{T_2^2} \exp\left(-\frac{\text{TE}}{T_2}\right), \\ \frac{\partial \Sigma(\text{TE})}{\partial S_0} &= \frac{\partial \Sigma}{\partial S} \frac{\partial S}{\partial S_0} = \frac{\partial \Sigma}{\partial S} \exp\left(-\frac{\text{TE}}{T_2}\right), \\ \frac{\partial \Sigma}{\partial S} &= \sqrt{\frac{\pi\alpha}{2}} \exp(-\alpha) \left(I_0(\alpha) + I_1(\alpha) \right), \end{aligned} \quad (4.7)$$

and the asymptotic expansions [Olver72] of Eqs. [4.6,4.7],

$$\begin{aligned} \frac{\Sigma(\text{TE})}{\sigma} &= 2\alpha^{\frac{1}{2}} + \frac{\alpha^{-\frac{1}{2}}}{4} + \frac{\alpha^{-\frac{3}{2}}}{64} + O(\alpha^{-\frac{5}{2}}) \\ \frac{\partial \Sigma(\text{TE})}{\partial S} &= 1 - \frac{1}{8\alpha} + O(\alpha^{-2}). \end{aligned} \quad (4.8)$$

Another method for T_2 calculation in the presence of noise can be derived from Eq. [4.2]. As Miller and Joseph observed [Miller93], the average of the variable $S_M^2 - 2\sigma^2$ is a mono-exponential, $S^2 = S_0^2 \exp(-\text{TE}/(T_2/2))$, (the term $\cos(\phi - \theta)$ averages to zero and n^2 to $2\sigma^2$). Miller and Joseph [Miller93] interpreted this average as a necessary average to be performed over regions of the images prior to the fit. Therefore, they limited their self to a region-based method, in which the signal intensity for each TE is first averaged over a ROI and then fitted to an exponential.

However, according to the main idea of this Chapter, that the noise-corrected signal decay is the adequate function to voxel-wise fit the data, the observation of Miller and Joseph [Miller93] can be re-interpreted such that the function $S^2 + 2\sigma^2$ is the noise-corrected decay of the random variable S_M^2 . Therefore, T_2 can be calculated not only for ROIs as suggested by Miller and Joseph but on a voxel basis by fitting the S_M^2 data to an exponential function plus a constant, $S^2 + 2\sigma^2$. Even more, it can be demonstrated that from the theoretical point of view squaring the data does not affect the quality of the fit (see Appendix A).

4.2 Methods

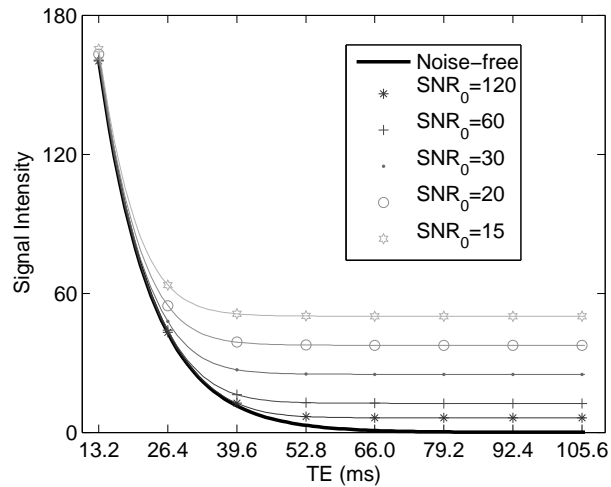


Figure 4.1: Example of a noise-free exponential decay (Eq. [4.1], black line) with $T_2 = 10$ ms and $S_0 = 600$ and the resulting noise-corrected exponential decays (Eq. [4.6], gray lines) for SNR at zero TE between 15 and 120.

4.2 Methods

4.2.1 MRI measurement protocol

All measurements were performed on a 1.5-T whole-body scanner (Magnetom Symphony; Siemens Medical Solutions, Erlangen Germany) using a circularly polarized quadrature knee coil. For T_2 measurements, the MSME sequence described in Section 3.2.1 was used ($TR = 3500$ ms, $TE_{\min} = 13.2$ ms, 8 echoes, echo spacing = 13.2 ms, $FOV = 160 \times 160$ mm², matrix = 256×256 , slices = 20, slice thickness = 3 mm, acquisition time = 14:56 min, gap between slices = 0 mm, in-plane resolution = 0.6×0.6 mm²). As in our experience it is problematic to adequately segment cartilage from MSME images, T_1 -weighted FLASH images with water excitation were additionally acquired for cartilage segmentation with the same slice geometry, resolution and positioning as for the MSME sequence ($TR/TE = 19/9$ ms, flip angle = 25° , acquisition time = 2:55 min).

Segmentation of the cartilage was performed using proprietary software [Hohe02]. The FLASH-based segmentation was overlaid on the MSME dataset and its overlap was visually controlled to assure optimal delineation of cartilage in every dataset. In case of discrepancies between the FLASH segmentation and the cartilage position in the MSME dataset, manual correction of the segmentation was performed (necessary in 2 of the 6 volunteers for one MR imaging session each).

4.2.2 Calculation of the T_2 relaxation time

The relaxation time T_2 was calculated voxel-by-voxel with four different methods using self-written Matlab programs (Matlab v7.0, The MathWorks, Natick, Massachusetts, USA):

4 T_2 calculation in conditions of low SNR

1. Minimum variance case of a linear least squares regression (LR) [MacFall86].
2. Nonlinear fit of S_M to an exponential function (EXP).
3. Nonlinear fit of $S_M^2 - 2\sigma^2$ to an exponential function (SQEXP) [Miller93].
4. Nonlinear fit of S_M to a noise-corrected exponential function (NCEXP).

All nonlinear fits were performed with the Levenberg-Marquardt algorithm, using the analytical expressions of the derivatives (Eqs. [4.7,4.8] for the NCEXP method) [Levenberg44, Marquardt63]. The result of the LR method was used as the starting guess of T_2 and S_0 . For the SQEXP and NCEXP methods, the parameter σ was previously calculated for each slice as $\sqrt{2/\pi}$ times the standard deviation over all voxels in a background ROI located in the upper left corner of the 8 images of the same slice acquired with different TEs (including $20 \times 20 \times 8 = 3200$ voxels).

4.2.3 Calculation of the SNR

To avoid a T_2 dependence in SNR, all SNR values in this work were calculated at zero TE as the quotient of S_0 and σ , and therefore denoted as SNR_0 . The value of σ is calculated from the noise distribution in a background ROI (see Section 4.1). In the simulations, the value of S_0 is a priori fixed. For the MRI measurements, SNR_0 is calculated as the quotient of S_0 calculated with the NCEXP method in the segmented cartilage and σ .

4.2.4 Numerical simulations

A synthetic phantom was defined with 10 fields with different T_2 (10, 21, 32, 43, 54, 66, 77, 88, 99 and 110 ms); each field contained 1350 pixels. Noisy MR images of this phantom were simulated for the same TEs as in the MSME sequence. In the simulations, S_0 was kept constant, whereas σ was varied to obtain SNR_0 between 67 and 15. For each SNR_0 , T_2 was calculated with the four methods.

4.2.5 Accuracy and precision

Errors in calculated T_2 are characterized by the accuracy, which measures how close the mean of the calculated T_2 is to the true T_2 , and precision, which accounts for the spread, i.e. the standard deviation (SD) of the measured T_2 . Only if the true T_2 is known, which is the case in the numerical simulations, can the accuracy and precision of the different fit methods be examined. In simulations, the accuracy and precision were estimated from the T_2 values calculated over 1350 identical voxels with the same true T_2 . The accuracy was assessed by statistically testing if the mean of the calculated T_2 values in each field (i.e. with the same exact T_2 value) for each SNR_0 level and fit method after extreme outliers removal deviates from the true T_2 (Wilcoxon signed rank test, $P < 0.001$). A T_2 value is considered to be an extreme outlier if its distance to the inter-quartile interval (i.e. the interval between the 25%- and 75%-percentiles) exceeds three times the length of the inter-quartile interval.

The best achievable precision of T_2 for any non-biased fit method (minimal possible SD of T_2), can be calculated if the noise distribution is known. This minimal SD is known as the Cramér-Rao lower bound (CRLB) (see Appendix). The CRLB was compared (chi-square test, $P < 0.001$) to the SD of the calculated T_2 in each field (exact T_2), for each SNR_0 level and fit method after extreme outliers

4.2 Methods

removal. Moreover, the precision of the different methods was compared for each field and SNR_0 level against each other using the Levene test ($P < 0.001$) [Levene60], which tests for equal variance in multiple samples without assuming normal distribution in the data.

4.2.6 Phantom measurements

Nine test tubes were filled with distilled water with different concentrations of Gadopentetate dimeglumine (USAN) (Magnevist, Bayer-Schering, Berlin, Germany), ranging between 2.3 mmol/L and 9.7 mmol/L to reproduce typical relaxation times of cartilage (between 60 ms and 15 ms, Table 1). The tubes were placed on the same circularly polarized quadrature knee coil used for in vivo imaging and six times imaged with the MSME sequence with increasing resolution (square acquisition matrix of 64, 128, 192, 256, 384 and 512), and keeping all sequence parameters fixed as described above (see Section 4.2.1). For each measurement, T_2 was calculated with all four methods.

Table 4.1: Gd-DTPA concentration, true T_2 times and SNR_0 values for the phantoms.

| Gd ^{1*} (mmol/L) | T_2 ² (ms) | SNR_0 ³ | | | | | |
|------------------------------|----------------------------|-----------------------------|-------------|------------|------------|------------|------------|
| | | 64×64 | 128×128 | 192×192 | 256×256 | 384×384 | 512×512 |
| 2.3 | 58.7 (0.9) | 343 (19) | 167.3 (6.7) | 67.4 (2.4) | 44.5 (1.6) | 25.0 (0.8) | 16.7 (0.5) |
| 2.7 | 47.3 (0.6) | 360 (17) | 177.1 (5.6) | 70.4 (2.0) | 46.6 (1.3) | 26.5 (0.7) | 17.4 (0.4) |
| 3.1 | 41.0 (0.6) | 422 (14) | 205.7 (2.4) | 84.6 (0.7) | 56.1 (0.5) | 30.7 (0.6) | 21.1 (0.2) |
| 3.8 | 31.7 (0.7) | 376 (20) | 187.4 (4.7) | 74.6 (1.8) | 48.8 (1.1) | 26.1 (0.6) | 17.8 (0.4) |
| 4.8 | 26.0 (0.4) | 341 (15) | 167.6 (3.1) | 65.1 (1.1) | 43.3 (0.4) | 23.7 (0.6) | 15.5 (0.2) |
| 5.6 | 24.2 (0.4) | 361 (16) | 173.2 (2.9) | 67.9 (1.0) | 44.8 (0.6) | 24.7 (0.3) | 16.1 (0.2) |
| 6.5 | 21.6 (0.3) | 337 (15) | 167.1 (3.2) | 63.2 (1.1) | 41.7 (0.3) | 22.7 (0.6) | 14.3 (0.2) |
| 8.4 | 18.7 (0.2) | 366 (15) | 178.9 (2.1) | 70.5 (1.0) | 45.7 (0.7) | 23.8 (0.3) | 15.7 (0.3) |
| 9.8 | 14.7 (0.4) | 336 (15) | 162.8 (2.1) | 65.4 (1.2) | 41.8 (0.8) | 22.2 (0.2) | 14.5 (0.1) |

¹Concentration.

²True T_2 (mean (SD)) calculated on the 64×64 matrix.

³Mean (standard deviation).

Since the 64-matrix images have the highest SNR_0 , the T_2 values calculated with the NCEXP method from the 64-matrix images were considered the *true*, i.e. reference T_2 values for analysis of the accuracy and precision (Table 4.1). In the analysis of the accuracy and precision all voxels in a single test tube acquired with the same resolution were considered together. Analogously to the simulations, the accuracy was assessed by comparing the mean T_2 calculated with each fitting method, for each phantom at each SNR_0 level with the true T_2 value of the phantom. The precision was compared with the CRLB for each phantom, fitting method and SNR_0 . The accuracy and precision obtained on phantom images were compared with simulations performed for the same true T_2 values and SNR_0 levels as measured in the phantom scans.

4.2.7 In vivo measurements

Six healthy volunteers (3 male, 3 female, mean age 23.7 ± 1.4) were examined at seven different time points (four times in one imaging session with repositioning of the knees between the measurements and one time in each of three successive imaging sessions separated by one week) with both, the FLASH WE and the MSME sequences. The volunteers had no history of knee injury or surgery and no episodes of knee pain in the past 3 years, and were asked to rest one hour before examination in order to avoid influence from physical exercise [Eckstein98b]. Special care was taken to strictly position the knees in an angle of 10° of flexion, neutral position without internal or external rotation and with the long axis of the leg parallel to the main magnetic field. MRI slices were selected to be perpendicular to the magnetic field, centred on the patellar cartilage and covering the complete cartilage. All volunteers gave informed consent to participate in the study.

Since the true T_2 values of cartilage are not known, it is not possible to directly assess the accuracy and precision in vivo. Nevertheless, they can be tested indirectly by comparing with each other the T_2 values obtained with the different methods, and correlating these comparisons to the results of the simulations. On this background the relative accuracy and precision are defined as the accuracy and precision calculated using the NCEXP T_2 values as reference values, comparable to the true, predefined T_2 values in the simulations. Since only the differences in T_2 from the four fit methods will be analyzed, all data of all voxels in all volunteers were pooled together. Voxels were pooled according to their reference T_2 in intervals of 1 ms (reference T_2 between 10 and 11 ms, between 11 and 12 ms...). For each group, the accuracy (mean) and precision (standard deviation) of the T_2 obtained with the other three methods were calculated after extreme outliers removal.

Simulations were performed using the same T_2 distribution as the in vivo calculated NCEXP T_2 values and the same SNR_0 distribution as measured in the in vivo images. A synthetic phantom with T_2 values distributed according to the distribution of the NCEXP T_2 values in vivo was created. From this phantom simulations were performed with SNR_0 distributed according to the distribution of the SNR_0 in cartilage. The relative accuracy and precision was calculated from the simulations and compared with the in vivo results.

4.3 Results

4.3.1 Numerical simulations

The first row of Fig. 4.2 shows simulated MRI measurements calculated from the synthetic phantom. The mean time needed to calculate T_2 for a voxel with an SNR_0 of 25 and an exact T_2 between 10 and 110 ms in a 2.8 GHz computer was (0.24 ± 0.21) ms with the LR method, (5.4 ± 5.1) ms with the EXP method, (28.0 ± 4.5) ms with the SQEXP method, and (24.2 ± 7.3) ms with the NCEXP method. The number of extreme outliers in a field ($N = 1350$ voxels), was lower than 5 for all methods with true $T_2 \geq 21$ ms independently of the SNR_0 level (mean (SD) number of outliers were 1.0 (1.5), 0.62 (0.98), 0.36 (0.75), 0.57 (0.89) with the LR, EXP, SQEXP and NCEXP methods, respectively). For $T_2 = 10$ ms the number of extreme outliers grows from about 6 at a $\text{SNR}_0 = 26.0$ to 84 at a $\text{SNR}_0 = 14.4$.

Accuracy and precision of the simulated T_2 measurements with the four described methods are shown in Fig. 4.3 for SNR_0 values between 67.0 and 14.6. Representative numerical values of accuracy and precision, i.e. mean and standard deviation calculated over all 1350 voxels in one field at an SNR_0 level, are summarized in Table 4.2. Both, the LR and EXP methods led to poor accuracy

4.3 Results

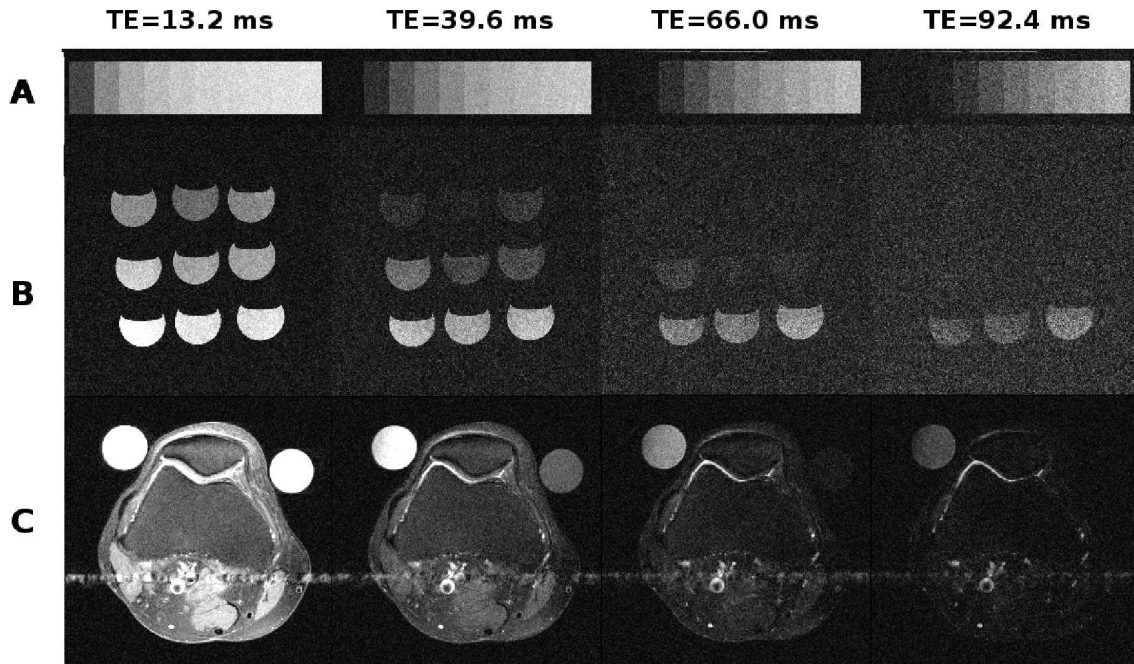


Figure 4.2: Example of simulated and MSME images for TEs of 13.2, 39.6, 66.0 and 92.4 ms. **A.** Synthetic MR images. **B.** Phantom images acquired with a matrix of 256×256 . **C.** Images of a healthy volunteer (matrix 256×256).

at low SNR_0 and T_2 , the LR method yielding worst results. For a T_2 of 10 ms and SNR_0 of 14.6, the deviation of the mean value from the true value was as high as 772% with the LR method and 522% with the EXP method (Table 4.2). The LR method led to a significant ($P > 0.001$) deviation from the true T_2 value for the complete range of T_2 independently of SNR_0 , whereas the EXP method deviated significantly for $T_2 \leq 54$ ms or $\text{SNR}_0 \leq 30$. The T_2 calculated with the SQEXP method showed a significant deviation from the true T_2 value only for $T_2 = 10$ ms and $\text{SNR}_0 \leq 60$ (maximal significant deviation of 11.4%). The NCEXP method had no significant deviation from the true value for any T_2 and SNR_0 (maximal non-significant deviation 7.0%).

The precision of the NCEXP method was comparable with the CRLB ($P < 0.001$) for $T_2 \geq 21$ ms and $\text{SNR}_0 \geq 21.5$. The EXP method was comparable with the CRLB for $T_2 \geq 32$ ms and $\text{SNR}_0 \geq 21.5$. The LR method was comparable with the CRLB only for $T_2 \geq 66$ ms and $\text{SNR}_0 \geq 31.4$. The SQEXP method was not comparable with the CRLB for any T_2 and SNR_0 .

The NCEXP method was the most precise of all four methods ($P < 0.001$). The SDs obtained by the EXP method were larger than the SD of the NCEXP method only for $T_2 < 32$ ms (independent of SNR_0). The LR method leads to larger SDs than the EXP and NCEXP methods for $T_2 \leq 56$ ms or $\text{SNR}_0 \leq 18$.

4 T_2 calculation in conditions of low SNR

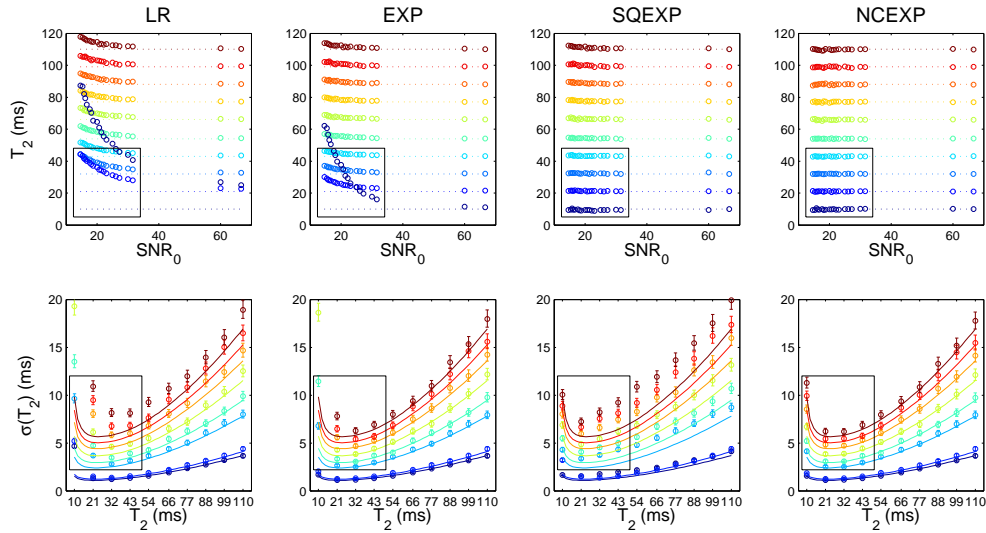


Figure 4.3: Accuracy and precision of the T_2 values in simulations with the LR, EXP, SQEXP and NCEXP methods (from left to right). First row, the accuracy (mean T_2) is represented against the SNR_0 . Colors encode different true T_2 (10, 21, 32, 43, 54, 66, 77, 88, 99 and 110 ms from dark blue to dark red), and dotted lines represent the true T_2 values. Second row, the precision (SD) is plotted against the true T_2 . Colors encode here different SNR_0 levels (67, 59, 31, 26, 21, 18, 16 and 15 from dark blue to dark red). Solid lines are the CRLB for the different SNR_0 levels. Error bars represent the 99% confidence interval of the standard deviation. Error bars intersecting with the CRLB indicate precisions comparable with the CRLB. The black rectangles represent typical SNR_0 and T_2 values for in vivo articular cartilage.

4.3.2 Phantom measurements

An example of a phantom measurement and the corresponding calculated T_2 maps are shown in the second row of Fig. 4.2, and in Fig. 4.4, respectively. Mean SNR_0 values of the images were 359, 177, 70.1, 46.0, 25.1 and 16.6 for increasing resolution from 64 to 512. T_2 calculated with the NCEXP method from the images with the lowest resolution was considered the *true*, i.e. reference, T_2 value (Table 4.1). Mean SNR_0 of the images were 359, 177, 70.1, 46.0, 25.1 and 16.6 for increasing resolution from 64 to 512.

Accuracy and precision of T_2 measured from phantoms are represented in Fig. 4.5. The LR method showed the lowest accuracy with a significant overestimation of T_2 for all true T_2 and SNR_0 except $T_2 \geq 21.6$ ms and $\text{SNR}_0 > 177$. The EXP method, too, led to significant overestimation T_2 for true $T_2 \leq 30.8$ or $\text{SNR}_0 \leq 23.9$. The SQEXP and NCEXP did not show any systematic deviation of T_2 for any resolution or SNR_0 level. It is worth noting the good agreement between simulations and phantom measurements.

The precision of the NCEXP and EXP methods was comparable with the CRLB for $T_2 \geq 23.9$ ms or $\text{SNR}_0 \geq 46.1$. The NCEXP method was the most precise method for all values of T_2 and SNR_0 ($P < 0.001$). The LR method led to the largest SDs, followed by the SQEXP method.

4.3 Results

Table 4.2: Accuracy and precision for different T_2 and SNR_0 values.

| True ¹ T_2 | Fit method | SNR_0 | | | | |
|-------------------------|------------|----------------|-------------|-------------|-------------|-------------|
| | | 67 | 30 | 25 | 20 | 15 |
| 10 ms | LR | 24.9 (4.7) | 43.9 (11.1) | 50.9 (14.8) | 64.5 (22.8) | 87.2 (41.7) |
| | EXP | 11.0 (1.7) | 17.8 (8.8) | 23.7 (13.1) | 37.6 (23.3) | 62.2 (39.6) |
| | SQEXP | 9.9 (1.6) | 9.5 (4.7) | 9.4 (5.5) | 9.3 (7.4) | 9.4 (10.0) |
| | NCEXP | 10.0 (1.6) | 10.1 (4.6) | 9.9 (5.4) | 9.8 (7.5) | 9.3 (11.3) |
| 21 ms | LR | 22.6 (1.3) | 28.8 (4.0) | 31.1 (5.0) | 36.1 (7.0) | 44.3 (10.9) |
| | EXP | 21.4 (1.1) | 23.2 (2.8) | 23.8 (3.5) | 25.8 (4.9) | 30.1 (7.8) |
| | SQEXP | 21.1 (1.5) | 21.2 (3.4) | 21.1 (4.2) | 21.5 (5.4) | 21.4 (7.2) |
| | NCEXP | 21.0 (1.1) | 21.1 (2.6) | 20.9 (3.3) | 21.3 (4.3) | 21.3 (6.2) |
| 32 ms | LR | 32.6 (1.2) | 35.4 (3.1) | 36.7 (3.9) | 39.1 (5.1) | 44.3 (8.2) |
| | EXP | 32.2 (1.2) | 33.2 (2.7) | 33.8 (3.4) | 34.8 (4.2) | 37.1 (6.3) |
| | SQEXP | 32.0 (1.7) | 32.3 (4.0) | 32.3 (4.8) | 32.4 (6.1) | 32.4 (8.2) |
| | NCEXP | 32.0 (1.2) | 32.1 (2.7) | 32.0 (3.4) | 32.2 (4.2) | 31.9 (6.2) |

¹ Mean (standard deviation) in ms.

4.3.3 In vivo measurements

Examples of in vivo images are shown in the third row of Fig. 4.2. The mean SNR_0 of all cartilage voxels in all examinations was 25.3, ranging from 12.4 to 34.1. Representative T_2 maps obtained with all methods and SNR_0 maps are shown in Fig. 4.6. The T_2 profiles illustrate even more clearly that both the LR and EXP method resulted in significant overestimation of T_2 at and close to the bone-cartilage interface, where the lowest SNR_0 took place.

The relative accuracy and precision of the LR, EXP and SQEXP methods compared to the NCEXP method are shown in Fig. 4.7. The LR and EXP methods presented a poor relative accuracy, which is particularly bad for low T_2 values. Voxels with a T_2 between 10 and 11 ms calculated with the NCEXP method showed an averaged T_2 of 47 ms with the LR method (overestimation of 370%), and 22 ms with the EXP method (overestimation of 120%). The SQEXP method had a good relative accuracy for T_2 values lower than 35 ms (which include 80% all voxels), but an underestimation of T_2 of up to 4.7 ms (underestimation of 8.7%) for $T_2 \geq 35$ ms. Simulations (dots in Fig. 4.7) coincided quite well for the relative accuracy in the range between 15 and 35 ms (70% all voxels).

In vivo relative precision behaved similar to the simulations. The highest relative precision was achieved with the SQEXP method for $T_2 < 20$ ms and with the EXP method for $T_2 \geq 20$ ms. The simulations also accurately described the relative precision for T_2 NCEXP values between 15 and 35 ms, but tended to underestimate the relative precision outside this interval (Fig. 4.7).

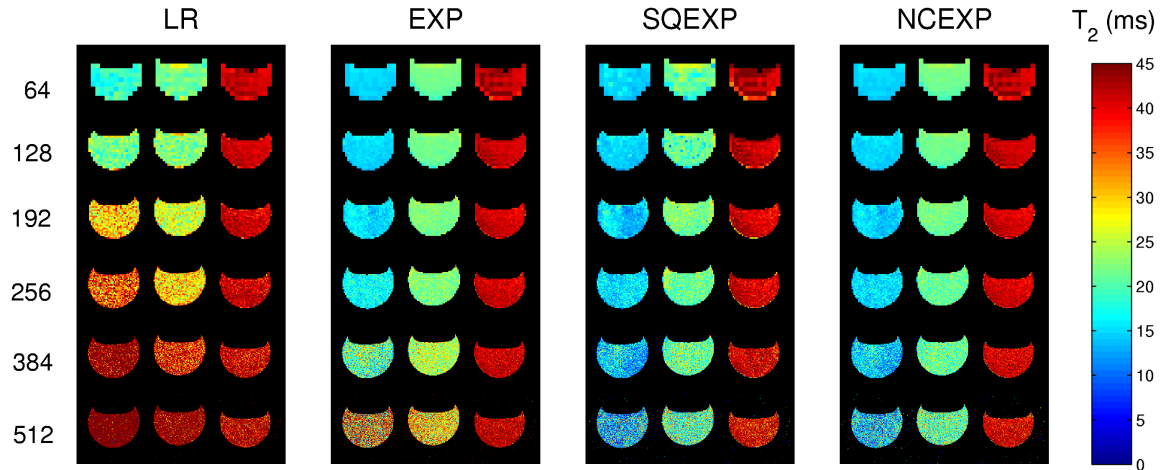


Figure 4.4: Example of T_2 maps of phantom measurements of three tubes (true T_2 of 14.7, 21.6 and 41.0 ms calculated from the 64×64 images with the NCEXP method) for the four methods (from left to right the LR, EXP, SQEXP and NCEXP methods), and increasing resolution (matrix size indicated on the left side of the figure).

4.4 Discussion

In this work it is demonstrated that fitting to noise-corrected functions, which correctly describe the decay of S_M or S_M^2 with the TE, results in accurate and precise T2 values, whereas fitting to the noise-free function leads to inaccuracy or imprecision.

In most works concerned with the accuracy and precision of T_2 values it is a common practice to assume $\text{SNR}_0 \geq 100$ [MacFall86, Jones96, Graham96, Bonny96, Bastin98, Shrager98, Whittall99], so that the noise distribution can be approximated by a zero mean Gaussian. In this case the noise-corrected signal decay coincides with the noise-free signal decay (Eq. [4.1]), so that the exponential function can be used for T_2 calculation without significant loss of accuracy or precision. Recently, Koff et al. [Koff08] reported the loss of accuracy in T_2 values obtained in articular cartilage with the different traditional methods, although they failed in identifying noise as the cause of these disagreements.

To the best of our knowledge, only two correction methods for the calculation of MRI parameters from decaying signal images in low-SNR conditions have been proposed in the literature. Miller and Joseph [Miller93] proposed a ROI-based method, on which the SQEXP method is based (see Section 4.1). In diffusion-weighted imaging, Dietrich et al. [Dietrich01] introduced a ROI-based method in which the averaged signal intensity in a ROI is noise-corrected previous to exponential fitting. This method has been extended to include multi-channel coil acquisitions [Koay06].

Although this work has been devoted to T_2 calculation it has direct applications to the measurement of other MR parameters calculated from an exponential decay, such as $T_{1\rho}$ or diffusion coefficients (see Chapter 3).

4.4 Discussion

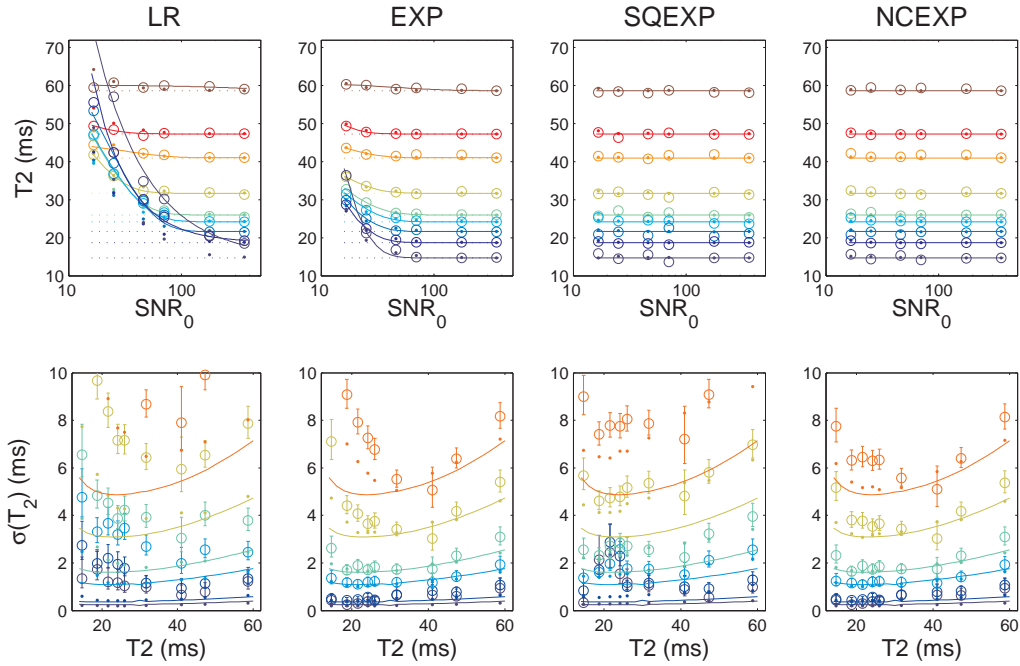


Figure 4.5: Accuracy and precision of the T_2 values in the phantom measurements with the LR, EXP, SQEXP and NCEXP methods (from left to right). First row, mean T_2 against the mean SNR_0 level (359, 177, 70.1, 46.0, 25.1 and 16.6 from dark blue to the dark red). To improve visibility, all mean T_2 values of the same tube are fitted to an exponential function. The dotted lines represent the true T_2 . Second row, the precision (SD) is plotted against the true T_2 . Colors encode results obtained for different mean SNR_0 levels. Solid lines represent the CRLB for the different mean SNR_0 levels. Error bars represent the 99% confidence interval of the standard deviation. Error bars intersecting with the CRLB indicate precisions comparable with the CRLB. In all plots, dots represent the results of the simulations performed for the true T_2 values and with same SNR_0 levels as in phantom images.

4.4.1 The fit methods

The LR method

In this work a least-squares regression weighted by the variance of the estimates of the SI was used [MacFall86]. Such a linear regression has the property that the estimators of T_2 and S_0 are minimum variance estimators (i.e. the highest precision) [MacFall86].

The major drawback of the LR method comes from the logarithm transformation of S_M , which causes great errors when S approaches zero. For vanishing S , the $\log(S)$ tends to minus infinity, whereas $\log(S_M)$ varies randomly around $\log(\sigma)$. Thus, the LR method results in a large overestimation of T_2 and in an underestimation of S_0 .

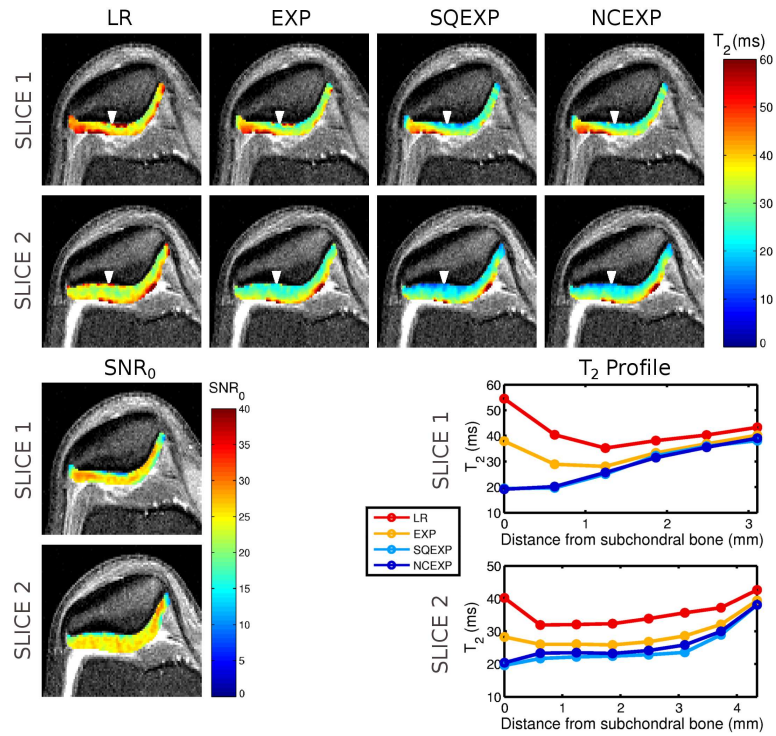


Figure 4.6: Examples of in vivo T_2 maps, SNR_0 maps and T_2 profiles in two slices of the same volunteer acquired in the same imaging session. Observe the increased T_2 values in the LR and EXP methods compared with the lower T_2 in the very similar SQEXP and NCEXP maps. Arrows in maps indicate the location of the T_2 profiles represented in the right side of the illustration. SNR_0 maps demonstrate low SNR_0 values near to the bone-cartilage interface. In T_2 profiles, the low SNR_0 causes increased T_2 values at the bone-cartilage interface with the LR and EXP methods.

The EXP method

The nonlinear fit method minimizes the sum of the quadratic distance of S_M to the noise-free model (Eq. [4.1]), and no logarithm transformation is needed. However, the influence of the noise-dominated echoes in the fit is still large for low T_2 and SNR_0 . For low T_2 , the noise-free signal intensity S decays rapidly so that later echoes are dominated by noise. For low SNR_0 and T_2 , the EXP method leads to overestimates of T_2 due to the large differences between S and S_M in the later echoes.

The choice of the starting guess for the nonlinear fits was not a critical point in any of the nonlinear fits (EXP, SQEXP and NCEXP methods). The same results would be obtained if, instead of the T_2 and S_0 values calculated with the LR method, constant values of T_2 and S_0 (for example 30 ms and 800), would be used as the starting guess for the nonlinear fits.

4.4 Discussion

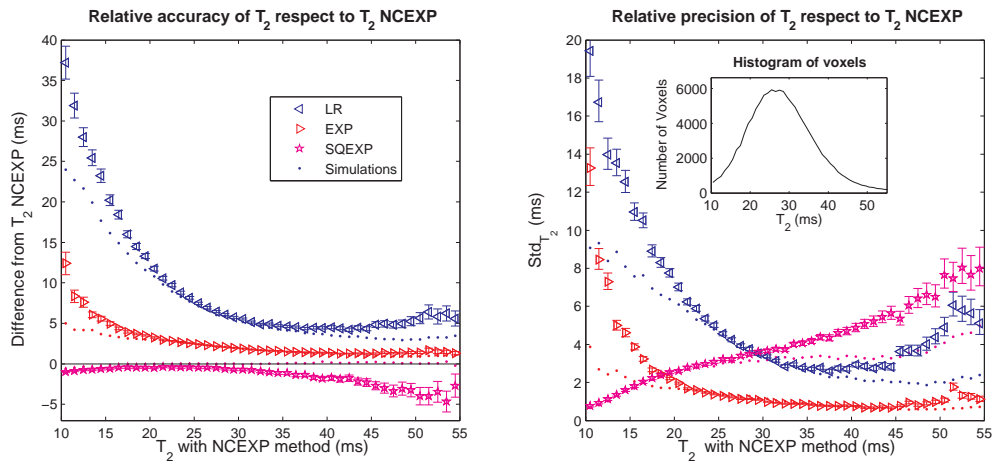


Figure 4.7: In vivo relative accuracy (left) and precision (right) of the LR (light gray), EXP (dark gray) and SQEXP (black) plotted over the reference T_2 (NCEXP T_2 values). Error bars represent the 99% CI for the mean (relative accuracy) and the SD (relative precision). The distribution of the NCEXP T_2 values of all voxels is represented in the small inset.

The SQEXP method

In the SQEXP method S_M^2 is fitted to an exponential plus a constant, $S_0 \exp(-2TE/T_2) + 2\sigma^2$. Since σ can be very accurately calculated from the image background, it should not be considered a fit parameter. The calculation of σ from images acquired at different TEs is possible since the noise in MRI is uncorrelated [Gudbjartsson95]. Considering σ as a free parameter could lead to cross-correlations with T_2 and S_0 affecting the precision of T_2 . Only if there is evidence that σ is not constant in the image (i.e. if filtering or partial acquisition of the k -space is being used), σ should be considered as a free-parameter to be fitted in the SQEXP or NCEXP method.

The SQEXP method is very accurate for all SNR₀ and T_2 . Although from the theoretical point of view a similar precision of the SQEXP and NCEXP methods is expected (see Appendix), larger SDs were systematically observed for by the SQEXP method. This may indicate that the fit method does not work optimally. Data are fitted using the least-squares criterion, which minimizes the squared distance between the measured signal and the fit function. However, the $S_M^2 - 2\sigma^2$ are not distributed symmetrically around the exponential (the term $n^2 - 2\sigma$ in Eq. [4.2] has zero mean, but the probability for $n^2 - 2\sigma \leq 0$ is $1-1/e \approx 0.63$, which is greater than 0.5, Eq. [4.3]). Therefore, a least-squares criterion, which does not consider an asymmetric distribution of the measured points around the function, may be prone to poorer precision than predicted by the CRLB. A criterion based on the maximum likelihood method could result in improved precision of SQEXP T_2 values, although it would make the implementation of SQEXP more complicated since it requires finding a minimum of Eq. [A.1].

The SQEXP method can be trivially extended to mean root (“sum of squares”) reconstructed multi-channel acquisition by fitting S_M^2 to the function $S^2 + 2n\sigma^2$, with n being the number of channels [Constantinides97, Dietrich08]. However, the method could fail if the noise distribution of ϕ (Eq. [4.3]) becomes non uniform by the use of filters, parallel imaging or noise correlations

[Dietrich08]. The method can also be trivially extended to include other signal decays such as the bi-exponential decay. In this case, the function to fit is no longer an exponential but the squared of the noise-free bi-exponential signal decay model. An analysis of the precision and accuracy of the fit in this case however is beyond the scope of the present thesis.

The NCEXP method

The NCEXP method is the most accurate and precise method for T_2 calculation. Indeed, no systematic deviation from the exact values could be demonstrated, and in simulations and high-SNR₀ phantom measurements the calculated T_2 values were comparable with the CRLB. The NCEXP method can be extended to other probability distributions such as acquisitions with multi-channel coils (see Appendix B), and to consider other signal decays than the monoexponential. The fit method remains the same up to the calculation of the derivatives in Eq. [4.7], where the derivative of S with respect to the new parameters must be calculated.

Other fit methods

For the sake of clarity, only the most frequently used noise-free methods for T_2 calculation found in the literature (LR and EXP methods) were systematically compared to the noise-corrected methods (NCEXP and SQEXP). However, any other fit method which do not use a noise-corrected function, will inevitably lead to poor accuracy or precision in low-SNR images.

For example, it has been suggested, that adding a constant to the exponential fit [Mosher04a] will improve the accuracy of the T_2 values. Although the accuracy for low T_2 is improved with this method, it systematically underestimates T_2 , especially for large T_2 , where due to the high signal in all TEs the inclusion of a constant is unjustified. Underestimation in large T_2 would reduce the diagnostic value of T_2 , since the range of pathology is shortened.

Other methods, such as the nonnegative least squares fit [Laws04], which involves a logarithm linearization, or a threshold-selection the echoes for T_2 calculation, which discard the information of several echoes, would also suffer from inaccurate or imprecise T_2 values. Weighting the data in the EXP fit procedure is also inappropriate, since weighting only takes into account different (stochastic) spread of the data along the echo train, but not the *systematic* deviation of S_M .

Improving SNR₀ by averaging intensities of several voxels is also problematic, since at least 16 voxels must be averaged to increment the SNR₀ from 15 (lowest SNR₀) to 60, where the use of the EXP method is acceptable. This is a large amount of voxels, since the cartilage only have 3-6 voxels in thickness. Even more, averaging must be very carefully performed in order to avoid contamination of the signal intensity with the synovial liquid.

4.4.2 Numerical simulations

Simulations are a very useful tool to investigate the accuracy and precision of the different fit methods, since the true T_2 values are known. The most important conclusion of the simulations was the huge loss of accuracy of the LR and EXP methods at low T_2 (Fig. 4.3), and the good accuracy of the SQEXP and NCEXP methods. Interestingly, the SQEXP and NCEXP methods led to accurate results even for a T_2 of 10 ms, which is lower than the minimum TE.

4.4 Discussion

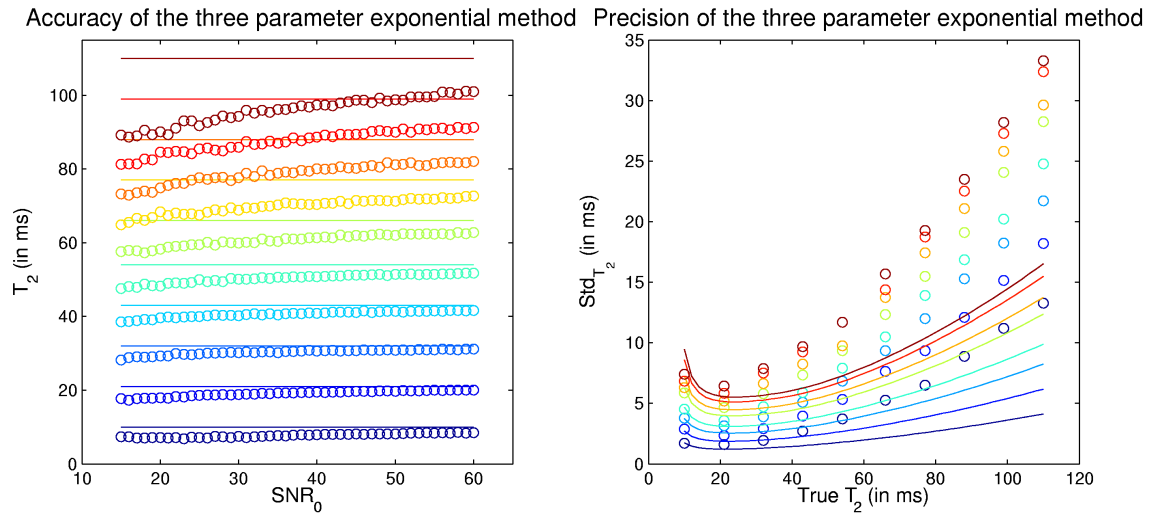


Figure 4.8: Accuracy and precision of the T_2 values in simulations with the 3P-EXP method. Left, the accuracy (mean T_2) is represented against the SNR_0 . Colors encode the true T_2 (10, 21, 32, 43, 54, 66, 77, 88, 99 and 110 ms from dark blue to dark red), and solid lines represent the true T_2 values. Right, the precision (SD) is plotted against the true T_2 . Colors encode here different SNR_0 levels (60, 40, 30, 25, 20, 18, 16 and 15 from dark blue to dark red). Solid lines are the CRLB for the different SNR_0 levels.

Simulations allowed comparing the precision of the different fitting methods to the highest achievable precision predicted by the CRLB. For each σ , the CRLB is a convex function with a minimum. For low SNR_0 and the TEs used in this study the CRLB took its lowest values for T_2 between 20 and 40 ms (Fig. 4.3), corresponding to the range of T_2 values in articular cartilage (see histogram in Fig. 4.7). Outside this interval the precision decreased due to poor sampling of the signal decay (low T_2) or due to truncation of the sampling (large T_2).

4.4.3 Phantom measurements

Phantom measurements allowed validating the results of simulations with real data. One of the major problems in T_2 measurement with a MSME sequence is the contamination of the signal intensity by stimulated echoes, which lead to falsely increased T_2 times. However the sequence used for image acquisition was optimized to avoid stimulated echoes (see Section 3.2.1). The possible underestimation of T_2 with a MSME sequence due to diffusion effects are much lower than the measurement errors caused by the SNR_0 . To demonstrate this, the pulse sequence with the same parameters as in scanner was simulated with the Siemens IDEA software and the b -values considering *all* gradients in the pulse sequence calculated at the 8 TEs based on Mattiello et al. [Mattiello97]. The b -values increased linearly from 0.66 s/mm² at the first TE to 4.35 s/mm² at the eighth TE. The underestimation of T_2 due to the diffusion-weighting was an order of magnitude lower than the typical measurement errors and

4 T_2 calculation in conditions of low SNR

can therefore be neglected¹. For a T_2 of 100 ms the error (greatest error) is 0.41 ms, which is smaller than the Crámer-Rao lower bound for a typical cartilage SNR_0 of 25 (7.8 ms) (see Section 4.3.1).

In phantom measurements, the SNR_0 can be easily modulated by varying the resolution of the images without changing any other sequence parameter, so that all the images capture the same decaying curve but with different SNR_0 levels. Therefore, the T_2 values calculated from the images with the highest SNR_0 were considered the *true* T_2 values and used for accuracy and precision analysis. A caveat to this method is that the T_2 values could change with the resolution due to the different diffusion-weightings caused from the varying amplitude of the readout gradients. However, an exact calculation of the b -matrix for all 8 echoes [Mattiello97] for a resolution of 64×64 and 512×512 , reveals that the largest diffusion-related apparent differences in T_2 are only 0.05 ms.

The generally good agreement between the simulations and the phantom measurements (Fig. 4.5) indicates that the results of simulations are also valid for phantom measurements. The small discrepancies in precision between the simulations and the phantom measurements have different causes. On the one hand, not all phantoms showed the same SNR_0 (Table 4.1), and simulations were performed with the mean SNR_0 . For example, the phantom with a T_2 of 41 ms showed an increased SNR_0 in all resolutions, and its precision was below the CRLB. The phantom with a T_2 of 47.3 ms had a SNR_0 very similar to the average SNR_0 and its values coincide rather well with the simulations. On the other hand, the T_2 maps of the lower resolutions were sometimes affected by residual artifacts (see for example the ringing on the phantom with T_2 of 41.0 ms in Fig. 4.4), which resulted in a larger SD explaining the discrepancies at large SNR_0 .

The fact that the number of pixels included in the calculation of the mean and standard deviation increased with the image resolution only slightly affected the error of the mean and standard deviation. The typical errors in the estimation can be estimated with the bootstrap method, which does not assume any specific distribution for the data. As an illustration, the relative error of the estimation of standard deviation of T_2 in % defined as, $\sigma_{\sigma_{T_2}} / \sigma_{T_2} \times 100$ is presented in Table 4.3. The small differences in the standard deviation between the 64 and the 512 matrix are not relevant for the phantom measurements. For example, the errors in the determination of the standard deviation of T_2 changed from 0.05 ms (7.7%) with the 64-matrix to 0.1 ms (2.2%) with the 512-matrix.

¹Since the b -values increase linearly with TE, $b = b_0 + \Delta b \cdot i$ and $\text{TE} = \Delta \text{TE} \cdot i$, the errors in T_2 can be easily estimated,

$$\begin{aligned} S &= S_0 \cdot \exp\left(-b_{\text{TE}} D - \frac{\text{TE}}{T_2}\right) \\ S &= S_0 \cdot \exp(-b_0 D) \cdot \exp\left(-\Delta \text{TE} \cdot i \cdot \left(\frac{D \Delta b}{\Delta \text{TE}} + \frac{1}{T_2}\right)\right), \end{aligned} \quad (4.9)$$

so that the apparent T_2 time, T_2^{app} , is

$$\frac{1}{T_2^{\text{app}}} = \frac{D \Delta b}{\Delta \text{TE}} + \frac{1}{T_2} = \frac{1}{T_2^b} + \frac{1}{T_2}, \quad (4.10)$$

and the difference is,

$$T_2 - T_2^{\text{app}} = \frac{T_2^2}{T_2 + T_2^b}. \quad (4.11)$$

T_2^b is 2.45×10^4 ms for a mean diffusion coefficient in cartilage of $D = 1.0 \times 10^{-3} \text{ mm}^2/\text{s}$ [Raya08c]. For a T_2 of 100 ms the error (greatest error) is 0.41 ms which is smaller than the CRLB for a typical cartilage SNR_0 of 25 (7.8 ms).

4.4 Discussion

Table 4.3: Relative errors in σ_{T_2} for different sample sizes

| T_2 (ms) ¹ | Error in the standard deviation $\sigma_{\sigma_{T_2}}/\sigma_{T_2}$ (in %) | | | | | |
|----------------------------|---|-----------|-----------|-----------|-----------|-----------|
| | 64×64 | 128×128 | 192×192 | 256×256 | 384×384 | 512×512 |
| 58.7 | 7.76 | 6.81 | 5.26 | 4.87 | 3.71 | 2.86 |
| 47.3 | 8.03 | 5.83 | 4.55 | 3.21 | 2.67 | 2.05 |
| 41.0 | 9.41 | 5.61 | 4.02 | 3.37 | 2.32 | 2.05 |
| 31.7 | 8.31 | 5.65 | 4.52 | 3.33 | 2.46 | 1.92 |
| 26.0 | 8.32 | 5.60 | 4.03 | 3.67 | 2.61 | 2.12 |
| 24.2 | 5.49 | 4.10 | 4.02 | 3.20 | 2.40 | 1.87 |
| 21.6 | 8.19 | 5.84 | 4.76 | 3.81 | 3.02 | 2.46 |
| 18.7 | 7.57 | 4.40 | 4.26 | 3.38 | 2.59 | 2.02 |
| 14.7 | 5.97 | 4.76 | 3.93 | 3.77 | 2.41 | 2.05 |
| Average | 7.7 (1.2) | 5.4 (0.8) | 4.4 (0.4) | 3.6 (0.5) | 2.7 (0.4) | 2.2 (0.3) |

¹True T_2 calculated on the 64×64 matrix with the NCEXP method.

4.4.4 In vivo measurements

The LR and EXP method showed a very poor relative accuracy for $T_2 \leq 25$ ms, which involves 37% of all cartilage voxels (Fig. 4.7). Voxels with low T_2 and SNR_0 are located at the bone-cartilage interface (Fig. 4.6), therefore the use of an inadequate fitting method artificially increases calculated T_2 in this region. This finding may be more likely to explain the unexpected increased T_2 values toward the bone-cartilage interface observed by other authors than volume averaging with subchondral bone marrow [Smith01, Mosher01, Dardzinski02], which could account for T_2 increase either in the femoral or the tibial bone-cartilage interface due to chemical-shift effects in readout direction but not in both interfaces simultaneously [Smith01], since the chemical effect only occurs in one direction. A correct determination of T_2 may improve the detection of local lesions in the early stages of OA and the diagnosis of diseases affecting the deep layers of the cartilage such as in autologous chondrocyte transplanted patients.

Simulations account very well for the relative accuracy and precision in the range from 15 to 35 ms, which includes 70% of all cartilage voxels, thus indicating that the conclusions obtained from simulations and phantom measurements also apply to in vivo measurements. The disagreement of the measurements with the simulations has a different cause for low and large T_2 . Most voxels with a T_2 lower than 15 ms were located near the bone-cartilage interface with the lowest SNR_0 of the whole cartilage (Fig. 4.6). However, in simulations the same SNR_0 distribution is assumed for all T_2 values. Thus, simulations showed better relative accuracy and precision for low T_2 values than in vivo data. The excellent agreement with simulations of the SQEXP method confirms this hypothesis, since the accuracy of the SQEXP method does not depend on the noise level.

For large T_2 , the discrepancy to simulations may be caused to some extent by the presence of partial volume effects. Voxels with NCEXP-determined T_2 larger than 40 ms are predominantly located at the articular surface, where they are prone to partial volume effects with the synovial fluid, which has a T_2 about 250 ms. Fitting the signal of the voxels affected by partial volume effect to a monoexponential

decay results in overestimation of the low T_2 component, which varies from one method to the other. In the NCEXP and EXP method the overestimation becomes much higher than in the SQEXP method, where the squaring of the data enhance the low T_2 component, thus resulting in lower T_2 values. The largest overestimation in T_2 occurs with the LR method, since the logarithm transformation especially emphasizes the long T_2 component.

4.5 Conclusions

Establishing a method for accurate and precise T_2 calculation from low-SNR₀ images is far away from being academic, since images for cartilage T_2 calculation are unavoidably affected from low SNR₀. The non-zero mean distribution of noise in the absence of signal causes the traditional f t methods (LR and EXP) to dramatically overestimate T_2 (overestimation up to 500%). The main idea of this work was to use the averaged decay of the measured signal intensity, S_M , with TE as the f tting function. The two noise-corrected f t methods (the SQEXP and the NCEXP methods) based on this idea and introduced in this chapter lead to a very accurate determination of T_2 , although they differ in precision. The NCEXP method is the most precise method for T_2 calculation. Indeed, its precision coincides with the maximally achievable precision (i.e. the Cramér-Rao lower bound) for SNR₀ ≥ 20. For in vivo images, using the traditional f t methods results in large overestimations of T_2 , especially in the deep radial zone toward the bone-cartilage interface. This may explain the unexpected increase of T_2 close to the tide mark in previous studies. The f t methods introduced in this study may contribute to improve the sensitivity of T_2 to detect pathology in cartilage and may contribute to increase the sensitivity to change in T2 follow-up studies, e.g. in cartilage repair or OA patients.

Chapter 5 Voxel based reproducibility of T_2 with a new registration algorithm

Reliable assessment of abnormalities (focal and diffuse) in articular cartilage and its evolution in time with T_2 requires knowledge of the healthy T_2 values in cartilage, and their reproducibility. Reproducibility can be calculated comparing datasets of the same subject acquired at different time points. The differences in patient and slice positioning between the repeated acquisitions does not allow for a direct comparison of datasets at a voxel basis, so that images must be registered before comparison. Since the articular cartilage is typically only 2–4 mm thick, registration should have precision errors smaller than the dimension of a single voxel. After registration, the voxel-based reproducibility can be calculated. At present, T_2 reproducibility has been systematically assessed only from comparatively large regions of interest [Glaser06, Glaser07, Koff09].

The purpose of this chapter was to develop and validate a registration method for the cartilage to assess the voxel-based T_2 reproducibility of patellar cartilage. Further applications of the registration algorithm apart from the subject matter of Chapter 6, will be briefly presented.

5.1 Theory

Rigid registration algorithms rely on two datasets, one, usually called target, which is kept fixed while the other one, called source, is successively transformed until reaching an optimal alignment. The implementation of this procedure requires the definition of three fundamental elements: A transformation model determining how the source dataset is transformed, a measure of the alignment of both datasets and an optimization method for maximization of alignment.

5.1.1 Transformation Model

3D Euclidean transformations, which include 3D rotations and 3D translations, have been used as a transformation model. To apply the 3D Euclidean transformations, each voxel is represented by the (metric) position vector and the Euclidean transformation is represented by a matrix. Voxels are transformed by multiplication of their position vectors with the transformation matrix. Between the different parameterizations of the rotation group, the Euler angles in the XYZ convention were chosen.

5.1 Theory

5.1.2 Measure of alignment

Given a source and a target datasets, the measurement of their alignment is a scalar function, usually termed similarity function, which has an extreme for perfectly registered data. In the registration algorithm presented here, the similarity function, Ω , is defined as the overlap volume between the two segmented datasets normalized to the mean volume of both datasets,

$$\Omega = \frac{V_{Trg \cap Src}}{\frac{1}{2}(V_{Trg} + V_{Src})}, \quad (5.1)$$

where V_{Trg} is the volume of the target image, V_{Src} the volume of the source and $V_{Trg \cap Src}$ the intersection volume between the target and the source datasets, so that Ω takes values between 0 and 1. The position of the data sets which maximize the similarity function Ω is considered as their registered position. Although the function Ω is normalized between 0 and 1, it should not be considered as a goodness of registration alone, since the value of Ω depends both on how good the data are registered and on how much target and source datasets really intersect. For example, cartilage voxels available in the source dataset, but not acquired or segmented in the target dataset, contribute to the total volume but not to the overlap volume; i.e., the value of Ω is reduced, even though the datasets may be perfectly registered. Therefore, introducing a pure goodness of registration is non-trivial because of the difficulty of differentiating whether a voxel is misaligned or simply belongs to a region not imaged or segmented in one of both datasets.

The exact calculation of the overlap volume is very time consuming, since for each two cuboid-shaped voxels it involves a total of 6 parameters describing their relative position and orientation. A simplification can be achieved by discarding the relative rotation between images and considering voxels as being parallel (parallel-voxel approximation). In a coordinate system oriented along the voxels' axes, two voxels with the same resolution, $\{\Delta X_i\}_{i=1,2,3}$ centered at the positions $\vec{X}(1)$, $\vec{X}(2)$ would produce an overlap volume, v ,

$$v = \begin{cases} \prod_{i=1}^3 \left(1 - \frac{|X_i(1) - X_i(2)|}{\Delta X_i}\right) \Delta X_i & \max\left(\frac{|X_i(1) - X_i(2)|}{\Delta X_i}\right) \leq 1 \\ 0 & \max\left(\frac{|X_i(1) - X_i(2)|}{\Delta X_i}\right) > 1 \end{cases} \quad (5.2)$$

where $|\cdot|$ denote the absolute value and \prod the Cartesian product.

Since in the parallel-voxel approximation the calculated overlap volume slightly differs when parallelizing the source voxels to the target voxels or the target voxels to the source voxels, the similarity function must be rewritten as follows,

$$\Omega = \frac{V_{Trg \cap Src} + V_{Src \cap Trg}}{V_{Trg} + V_{Src}}, \quad (5.3)$$

where $V_{Trg \cap Src}$ is the overlap volume with source voxels parallelized to the target voxels, and $V_{Src \cap Trg}$ is the overlap volume with target voxels parallelized to the source voxels. With this definition the similarity function is continuous and symmetric by interchanging the role of source and target.

5.1.3 Optimization method

For overlap maximization a quasi-Newton method based on the Broyden-Fletcher-Goldfarb-Shanno (BFGS) estimation of the Hessian matrix [Fletcher00] was used. A first approximation of the desired

5 Voxel based reproducibility of T_2 with a new registration algorithm

registration can be quickly performed by aligning the principal inertial axes of the source dataset to the inertial axes of the target dataset. Then small translations and rotations bring the images to the final registered position. Low-angle rotations and small translations have the fortunate property that they commute to a very good approximation, i.e. the result of an accomplished translation and rotation is almost independent of their order.

5.1.4 Comparison of registered datasets

After registration the T_2 value of each target voxel was compared to the interpolated T_2 values of its nearest-neighbor source voxels (trilinear interpolation). Differences in T_2 were characterized by the coefficient of variation (CV), which for T_2 takes the form

$$CV = \sqrt{2} \frac{|T_{2,Trg} - T_{2,Src}^i|}{T_{2,Trg} + T_{2,Src}^i}, \quad (5.4)$$

where $T_{2,Trg}$ corresponds to the T_2 value at the target voxel and $T_{2,Src}^i$ to the interpolated T_2 values of the nearest-neighbor source voxels to the position of the target voxel.

5.2 Methods

5.2.1 Numerical simulations

Patella model

Since the registration algorithm presented here is selectively based on the patellar geometry, simulations with an accurate mathematical model of the patellar cartilage closely mimic the behavior of the registration of real datasets.

In order to generate a mathematical model of the patellar cartilage an in vitro measurement of an excised human patella was performed. A fresh human patellar cartilage specimen was harvested at time of autopsy 24 hours after death. Following harvest, the sample was rinsed in physiologic saline and wrapped in a plastic film to prevent drying. MRI was accomplished at room temperature with a small amount of physiological saline between the cartilage surface and the plastic film to prevent susceptibility effects from air and drying of the sample during measurements. The sample was imaged with the FLASH WE sequence with a 1 mm slice thickness keeping all other parameters as described in Section 4.2.1. After manual segmentation of the cartilage, the patellar model was generated by linear interpolation of the points at the articular surface and bone-cartilage interface.

Simulation of MRI measurements

MRI measurements were simulated by calculating the intersections of the mathematical patellar cartilage model with 20 parallel slices (3 mm separation between the slices), randomly oriented in the axial direction and randomly translated around the patellar center of mass. Each intersection was filled up with 0.6×0.6 mm² voxels. The maximally allowed translation was half out of plane distance, i.e. 1.5 mm (a maximal relative distance between two slices of 1.5 mm in each direction, i.e., $\sqrt{3} \cdot 1.5$ mm = 2.6 mm). As constantly 20 slices per dataset were acquired, a displacement in slice position larger than 1.5 mm will effectively result in a shift in one slice number but not in larger

5.2 Methods

errors. The maximal angle deviation in the axial direction was 15° (resulting in a maximal possible relative angle between slices of 30°), which was much larger than the deviations that typically occur in routine clinical MRI.

Registration errors

The registration algorithm was implemented using Matlab software (The MathWorks, Inc., Natick, Massachusetts, USA). For each of the 1000 simulated pairs of MRI measurements the registration was performed twice, once for the complete patellar cartilage plate, and once for the BCI only.

The registration error was defined for each voxel as the absolute value of the difference between its registered and exact positions. In each simulation the distribution of the registration errors was calculated for all source voxels. This distribution was characterized by the mean registration error (MRE) and the maximum registration error (MARE), which are defined as the mean and maximum value of the registration errors over all source voxels.

Because of the anisotropic voxel size ($0.6 \times 0.6 \times 3 \text{ mm}^3$), errors were separately analyzed in each direction. Therefore, the MRE and MARE were calculated for each direction separately. For the distribution of registration errors, the registration error of each voxel in each direction was normalized by the voxel dimension in this direction. For each voxel the largest relative error was considered for the histogram of the registration errors.

Role of overlap volume

So far it has been hypothesized that the exact position of the datasets corresponds with the maximum overlap, so that optimizing the overlap volume leads to the best registration. In order to examine this hypothesis the differences between exact and calculated overlap volume were analyzed. Large deviations may either indicate that the optimization method is unable to find the exact position or that the overlap volume is not an appropriate measurement of alignment.

It has been also been explained that the overlap volume is not a measurement of the registration quality. The relationship between overlap volume and registration quality is resolved by calculating the Pearson's correlation coefficient between the overlap volume and the MRE and MARE.

5.2.2 In vitro measurement

Since in simulations segmentation occurs exactly, the influence of the segmentation errors in the registration has to be analyzed separately. Before applying the registration algorithm to in vivo measurements, the robustness of the registration algorithm has to be tested in the presence of segmentation errors. With this aim ten consecutive datasets of an excised human patellar cartilage were acquired with the MSME sequence. Special care was taken to maintain the precise position of the patella by using a special fixation device in the small-extremity coil. This fixation device consisted of a Plexiglas half-cylinder fitting the (cylindrical) inferior part of the small extremity coil with an extractable squared Plexiglas slice, on which the excised patella is glued with its bone side. Patellar cartilage was manually segmented in each of the MSME images with the shortest echo time.

To analyze the effect of segmentation in the registration algorithm, all possible pairs of the 10 segmented datasets of the patella specimen, 45 in total, underwent registration. Registration errors

5 Voxel based reproducibility of T_2 with a new registration algorithm

were characterized by the MRE and MARE, assuming the initial position as the correct registered position.

5.2.3 In vivo measurements

Volunteers

The voxel based reproducibility in the patellar cartilage was investigated on the same datasets as were used for the estimation of the accuracy and precision of the different T_2 fitting methods (see Section 4.2.7).

T_2 relaxation time

For the analysis of typical T_2 relaxation times in healthy cartilage, the T_2 values from the bone-cartilage interface to the articular surface were calculated as a function of the distance. For each multi-echo dataset, the bone-cartilage interface was separated and the normal vectors in the position of all voxels at the bone-cartilage interface computed. A profile is generated for each voxel in the bone-cartilage interface by linear interpolation of T_2 to eleven equidistant points in the line joining this voxel with the articular surface along the direction of the normal vector. Profiles were averaged after normalization of their length between 0 (bone-cartilage interface) and 1 (articular surface). Only trajectories whose length was larger than 70% of the maximum thickness were considered.

Voxel-based T_2 reproducibility

All possible pairwise combinations of the seven datasets of the same patient, 21, underwent registration. The only possibility to validate the registration method for in vivo measurements was to use consistency measurements [Hill01], which measure in multiple ($n > 2$) acquisitions of the same subject the differences in the registration when the data are registered in different ways. For the 7 datasets, $I_1, I_2 \dots I_7$ of the same volunteer, consistency was defined as the differences in the position of the voxels in the image I_7 , after registration with $I_1, I_1 \circ I_7$ (\circ symbolizes the operation of registration with I_1 as target and i_7 as source), and after indirect registration with I_1 including all pairwise registrations, $I_1 \circ I_2 \circ \dots \circ I_7$. By perfectly aligned data both operations give the same positioning for I_7 . Registrations errors would produce differences between both positions of image I_7 . These differences provide an estimation of the registration errors and were characterized with the MRE and the MARE. Consistency measurements were performed for the complete segmented cartilage, the bone-cartilage interface and the articular surface.

Once registered all patellar datasets were divided into regions along the principal inertial axes in order to allow a better overview and simpler visualization of the results: 3 in anterior-posterior (AP) direction, 6 in left-right (LR) direction and 4 in cranio-caudal (CC) direction. All regions contained approximately the same number of voxels. The intersections of the regions in all three directions divided each patellar dataset into a total of 72 ($6 \times 3 \times 4$) elemental regions. Once the elemental regions were defined in all datasets, all voxels from the $21 \times 6 = 126$ registrations were grouped according to the elemental regions they occupied. The distribution of the T_2 CVs in each elemental region was characterized by the median. To assess the significance of the differences between the elemental regions the U-test was used.

5.3 Results

5.3 Results

5.3.1 Numerical simulations

The registration algorithm was applied to 1000 simulations of two complete cartilage plates with an average of 2719 voxels per patella, and to 1000 simulations of two bone-cartilage interface with an average of 538 voxels per bone-cartilage interface. Averaged over the 1000 simulations the computing time for the registration of two complete patellar datasets was 59 s (7 s for the two bone-cartilage interface) on a Pentium 4 (2.8 GHz, 1 GByte RAM) computer.

Table 5.1: Mean and maximum registration errors

| | | Mean registration error (MRE) ¹ | | | Maximum registration error (MARE) ¹ | | |
|----------------------|------------|--|----------|-----------|--|-----------|-------------|
| | | LR | AP | CC | LR | AP | CC |
| Patella | Mean (Std) | 128 (76) | 90 (49) | 233 (141) | 267 (150) | 210 (103) | 457 (245) |
| (Simul.) | Max-Min | 490–7 | 280–4 | 823–10 | 922–14 | 617–11 | 1442–35 |
| Patella | Mean (Std) | 89 (129) | 78 (76) | 137 (71) | 249 (243) | 188 (140) | 340 (172) |
| (In vitro) | Max-Min | 533–2 | 265–7 | 282–29 | 733–6 | 681–79 | 835–17 |
| Patella ² | mean (Std) | 144 (138) | 78 (59) | 874 (657) | 233 (190) | 222 (136) | 1192 (682) |
| (In vivo) | Max-Min | 383–12 | 183–24 | 1918–110 | 494–45 | 436–72 | 1992–261 |
| BCI | Mean (Std) | 137 (79) | 94 (50) | 244 (149) | 265 (146) | 211 (100) | 454 (240) |
| (Simul.) | Max-Min | 490–7 | 280–5 | 822–10 | 915–17 | 617–11 | 1368–35 |
| BCI ² | Mean (Std) | 220 (144) | 113 (45) | 537 (714) | 380 (217) | 225 (105) | 962 (1001) |
| (In vivo) | Max-Min | 459–84 | 172–50 | 1939–62 | 699–155 | 402–78 | 2780–148 |
| AS ² | Mean (Std) | 462 (307) | 203 (92) | 683 (473) | 915 (698) | 400 (139) | 1475 (1163) |
| (In vivo) | Max-Min | 806–115 | 361–114 | 1324–161 | 1832–115 | 604–113 | 3166–161 |

¹ All errors in μm . Voxel size = $612 \times 612 \times 3000 \mu\text{m}^3$.

² Registration errors calculated using the consistence method (See 5.2.3)

The distribution of registration errors is represented for the complete patellar cartilage (including 2.71 Mio voxels, Fig. 5.1.A) and the bone-cartilage interface (including 0.54 Mio voxels, Fig. 5.1.B). For the complete cartilage the averaged registration error was 20.3% of the voxel size. 95% of all voxels showed a misalignment lower than 50.8% of the voxel dimension and only 0.2% all voxels had a misalignment greater than 100%. Bone-cartilage interface registration showed slightly larger registration errors, with an average of 28.6%, 95% all voxels having a misalignment lower than 68.2% and with only 1.6% of the voxels showing a misalignment greater than 100%.

For the registration of the complete patellar cartilage the MREs and MAREs showed a direction-dependent mean and standard deviation (Table 5.1), with largest values along the low-resolution CC direction (MRE: $(233 \pm 141) \mu\text{m}$, MARE: $(457 \pm 245) \mu\text{m}$). In the other two directions mean and standard deviations displayed values of about 40% (AP, MRE: $(90 \pm 49) \mu\text{m}$, MARE: $(210 \pm 103) \mu\text{m}$) and 55% (LR, MRE: $(128 \pm 76) \mu\text{m}$, MARE: $(267 \pm 150) \mu\text{m}$) of their corresponding values in the CC direction. The mean value of the MREs and MAREs for the registration of the complete patellar cartilage were clearly smaller than the voxel dimension. The mean MRE was 21% of the voxel dimension in the LR direction, 15% in the AP direction and 8% in the CC direction. Also MAREs remained smaller than the voxel dimension. Mean MAREs were 44% of the voxel dimension in the

5 Voxel based reproducibility of T_2 with a new registration algorithm

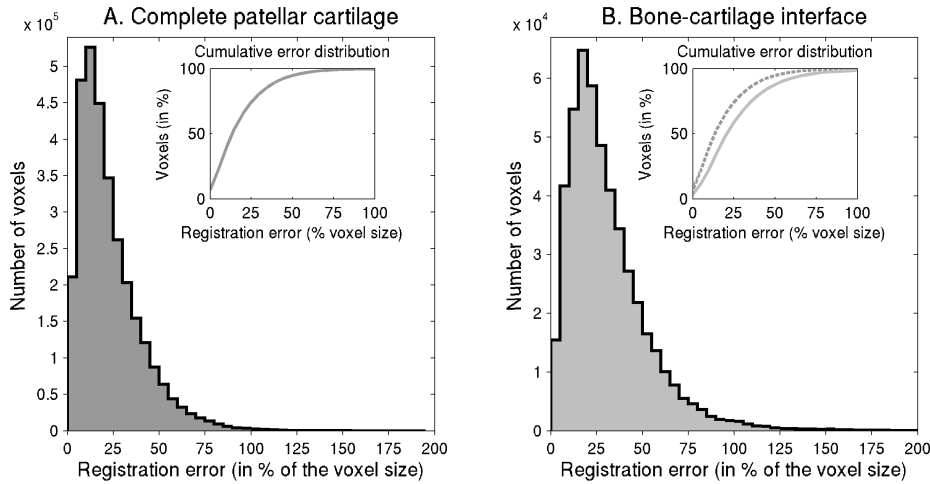


Figure 5.1: Distribution of registration errors for the registration of the complete patellar cartilage (A, 2.7 Mio voxel) and the registration of the BCI (B, 0.5 Mio voxels). Small insets represent the cumulative distribution of voxels (for the BCI the cumulative curve of the complete patellar cartilage is also represented with dashed line for comparison illustrating the slightly larger errors of the BCI registration).

LR direction, 35% in the AP direction and 15% in the CC direction. Only 2.5% of the simulations had MAREs larger than a voxel dimension in the LR direction and only 0.15% showed MAREs larger than the resolution in AP direction and no simulation lead to MARE in the CC direction larger than the slice thickness.

Simulations for the registration of the bone-cartilage interface also showed subvoxel accuracy (average MRE and MARE were 28% and 55% of the voxel size, Table 5.1), although registration errors were significantly larger ($P < 0.001$) as compared to the registration of the complete patellar cartilage.

5.3.2 Role of the overlap volume

In simulations, exact and registered overlap volumes had a very good correlation (r^2) of 0.92 ± 0.02 (Pearson's correlation coefficient, 95% confidence interval) for the complete patellar cartilage and a slightly lower correlation of 0.84 ± 0.03 for bone-cartilage interface simulations. Overlap volumes after registration of the complete patellar cartilage were on average slightly smaller, $(86.9 \pm 1.6)\%$, than the exact overlap volume, $(87.1 \pm 1.7)\%$. In the bone-cartilage interface simulations these differences grew in average up to 2% (exact $(55.5 \pm 15.6)\%$ and registered $(53.5 \pm 6.0)\%$ overlap volume).

Neither the overlap volume nor the differences between the exact and registered overlap had any effect on registration errors. Very low Pearson's coefficients were obtained from the correlation of MRE, MARE and the exact and registered overlap volume or their difference (mean 0.18, ranging from 0.33 to 0.03).

5.3 Results

5.3.3 In vitro measurements

MREs and MAREs calculated for the 45 registrations of the 10 measurements were of the same order of magnitude as the simulations of the complete patellar cartilage (Table 1). The in vitro overlap volumes after registration, $(88.1 \pm 2.0)\%$, were in good agreement with the values obtained in the numerical simulations.

Segmentation errors in cartilage were assessed by the frequency of a voxel being segmented in each image: The total number of voxels which were identified as cartilage voxels was 2854. From all these voxels 2112 were segmented in the 10 datasets. The rest of the voxels were segmented in some of the datasets: 134 voxels in 9 datasets, 89 in 8, 52 in 7, 59 in 6, 41 in 5, 37 in 4, 33 in 3, 111 in 2 and 186 in one. Most of the segmentation errors occur in the lateral portions of the cartilage and near to the articular surface .

5.3.4 In vivo measurements

T_2 relaxation times

T_2 values showed an increasing T_2 from the bone-cartilage interface to the articular surface (Fig. 5.2). Near to the bone-cartilage interface T_2 remained almost constant in the first 20% with values between 24 and 32 ms. Beyond the bone-cartilage interface, T_2 slowly increased up to values of 30 to 38 ms at a thickness of 80%. In the last 20% below the articular surface T_2 rose up to 42 to 52 ms. Interindividual T_2 variability also showed differences throughout the cartilage. At the articular surface T_2 values showed a large variability with differences of up to 16%. In the central region of the cartilage T_2 values appeared more homogeneous with variations around only 10%. Near to the subchondral bone T_2 values, again, showed a larger variability of up to 33%.

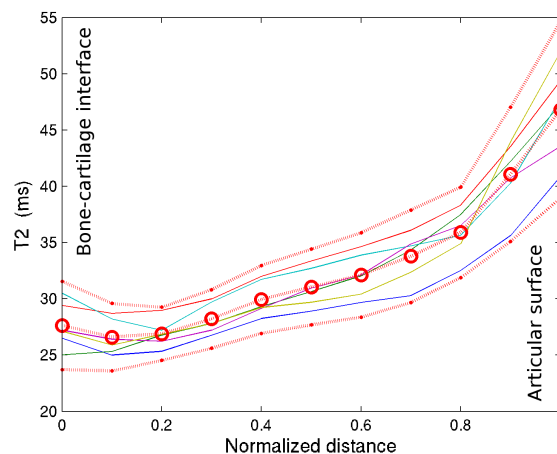


Figure 5.2: Distribution of T_2 from the bone-cartilage interface (normalized distance=0) to the articular surface (normalized distance=1). Color lines represent the mean T_2 profile for the 7 measurements of each volunteer. Discontinuous red lines represent the mean value (marked with circles) and the 95%-confidence interval over all volunteers.

5 Voxel based reproducibility of T_2 with a new registration algorithm

Image registration

The overlap volume before and after registration of the in vivo measurements is summarized in Table 5.2. The pairwise registration of the complete cartilage led to a mean overlap volume of $(85.7 \pm 1.4)\%$, whereas the mean overlap volume for the registration of the bone-cartilage interface was $(55.8 \pm 3.8)\%$. Interestingly, the registration of the articular surface result in significantly worse overlap volume (mean overlap volume, $(47.9 \pm 5.3)\%$). The importance of registration can be seen in the differences of overlap volume before and after registration. Registration of the complete patellar cartilage improved the overlap volume to 7.5%. More sensitive to registration were the bone-cartilage interface and the articular surface, which improved to 23.4% and 17.5% respectively.

Table 5.2: Overlap volume before and after registration of in vivo images

| Volunteer | Patella | | BCI | | AS | |
|-----------|---------------------|------------|---------------------|------------|---------------------|------------|
| | Before ² | After | Before ² | After | Before ² | After |
| 1 | 78.3 (3.8) | 84.5 (1.5) | 36.7 (8.1) | 57.3 (4.0) | 32.4 (5.7) | 46.7 (6.8) |
| 2 | 79.6 (6.3) | 87.5 (0.8) | 28.7 (11.1) | 54.0 (3.9) | 27.0 (8.3) | 47.9 (3.7) |
| 3 | 76.4 (8.9) | 84.8 (1.2) | 32.8 (14.1) | 56.9 (3.6) | 33.0 (13.3) | 51.8 (7.0) |
| 4 | 76.1 (9.2) | 86.8 (0.8) | 32.5 (12.1) | 56.9 (3.0) | 31.9 (11.3) | 54.2 (3.6) |
| 5 | 81.0 (5.6) | 86.4 (0.9) | 34.0 (12.4) | 56.1 (4.7) | 26.8 (8.7) | 42.7 (4.3) |
| 6 | 78.0 (5.4) | 84.3 (2.2) | 30.0 (9.7) | 53.7 (3.6) | 31.5 (7.8) | 44.1 (6.1) |

¹Overlap volume in % given as mean (standard deviation).

²Overlap before registration calculated after translation to the center mass.

Validation of the registration algorithm using consistency measurements lead to errors similar to those obtained with simulations and in vitro measurements (Table 5.1). The transformation for the registration calculated as the product of the transformation to the principal axes and the optimization transformation showed a mean rotation around the AP, LR and CC directions (Euler angles in the XYZ convention) of 1.8° , 1.8° , 2.5° (maximum rotations of $(7.0^\circ, 7.9^\circ, 8.4^\circ)$) and a mean translation of 5.1, 5.3, and 20.9 mm in the LR, AP and CC directions.

Voxel-based T_2 reproducibility

Considering all registered voxels together (371 600 voxels), the CVs of the T_2 showed a distribution with a median of 10.1%, with 90% of all voxels having a CV lower than 29.4%. Fig 5.3 shows the mean CV in each of the regions; the medians of the CVs in each of the 72 elemental regions are presented in Fig 5.4. The mean number of voxels per elemental region was 5 160 ranging from 2 856 to 8 210. A first interesting observation was that the CVs in T_2 showed differences between the regions. In the AP direction CV of T_2 ranged between 8.8% and 11.5% and was significantly ($P < 0.001$) larger in the elemental regions located at the articular surface than in the other regions. The lowest errors (between 7.2% and 8.2%) were found in the central part of the patellar cartilage. Larger CVs occurred in the regions close to the bone-cartilage interface with errors typically around 10.4%. The LR direction regions at the left facet exhibited larger CVs (between 8.2% and 15.5%)

5.4 Discussion

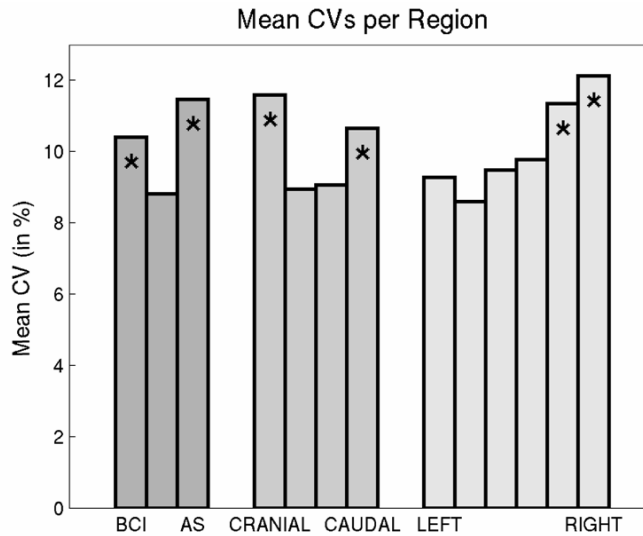


Figure 5.3: Histogram of the mean CVs of T_2 in each one of the regions: 6 in the LR direction, 4 in the CC direction and 3 in the AP (from bone-cartilage interface, BCI, to articular surface, AS) direction. Asterisks denote those regions which showed significantly higher CVs ($P < 0.001$, U-test).

than the central part of the patellar cartilage (between 7.5% and 11.6%). The distal and proximal regions in the CC direction showed significantly ($P < 0.001$) higher CVs (mean CV 11.0%) than in the central regions (mean CV 9.0%).

5.4 Discussion

5.4.1 The registration algorithm

The registration algorithm presented in this work is very simple to implement, since in contrast to other registration algorithms [Hill01], no interpolation or re-slicing of the data is needed at any stage of the registration. Yet, despite its simplicity, our data indicate that the registration algorithm is robust against segmentation errors and has an average accuracy better than 25% of the voxel dimension.

A key point in the 3D-rigid registration algorithm presented here is the election of the overlap volume as similarity function. The overlap volume is straightforward to calculate within the parallel-voxel approximation (Eq. [5.2]). Careful patient positioning and slice selection during in vivo measurements guarantee that only small transformations are required to register images. The low rotation angles with largest values of 9° can be considered as an a posteriori justification of the parallel-voxel approximation. However, in simulations, which included deviations up to 30° , this approximation also led to very accurate results.

The use of the overlap volume as a similarity function makes the registration accuracy partially dependent on the concrete shape of the registered object. For example, the slimness of patellar cartilage in the AP direction results in larger sensitivity of the overlap volume to misalignment in this direc-

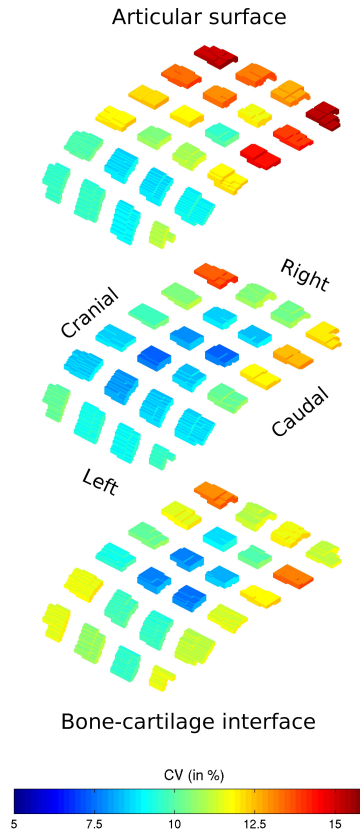


Figure 5.4: T_2 CVs of all 126 registrations are summarized in this figure. All patellae have been divided into same number of regions. Regions were selected by dividing the number of voxels equally. The median of the absolute value of the relative errors of all voxels belonging to the same region in all patellae was used to characterize errors in each region.

tion. A small erroneous displacement in the AP direction would result in misregistration of numerous voxels located at the surface. In contrast, incorrect positioning in the LR direction mostly misaligns voxels located at the peripheral facets, which represent just a small proportion of the total voxel number. This explains why the registration accuracy differs between the equally resolved LR and AP directions (Table 5.1). Although the largest registration errors are found in the CC direction, these errors only represent 8% of the voxel size (3 mm). The low relative errors in the CC direction are a consequence of the high resolution in the AP and LR directions, which penalizes large displacements in the CC direction with rapid decrease of the cost function.

Important for registration is the previous alignment of the principal inertial axes of the source dataset to the ones of the target dataset. This transformation works well for objects like patellar cartilage, which possess well differentiated principal moments of inertia, thus guaranteeing a good initial positioning near to the final solution and allowing a separate optimization by small translations and rotations. It is noteworthy that the rotations and translations in the subsequent optimization

5.4 Discussion

process were indeed quite small with maximal values of 8° and 0.7 mm supporting a posteriori this separated optimization approach.

Although the registration algorithm has been tested for axial images of the patellar cartilage in this study, there is no reason to limit its use to this case alone. Femoral and tibial cartilage, which can be imaged either coronally or sagittally, also present an irregular shape which is very well suited for registration with the method proposed in this article. Experiences on femoral and tibial cartilage (see section 5.5) have demonstrated similar registration errors as for the patella (proven by the method of Hill et al. [Hill01]). Other trivial extensions of the registration algorithm include registration of images with different resolutions and registration of images acquired with different orientations (i.e. registration of sagittal and coronal images).

5.4.2 Validation of the registration algorithm

Since the similarity function only depends on the shape of the patellar cartilage, registration errors can be estimated accurately with numerical simulations. Quantification of registration errors in simulations of the complete patellar cartilage yield mean MREs of less than one fourth of a voxel dimension. The registration of the bone-cartilage interface also leads to subvoxel accuracy, although it showed larger errors than the registration of the complete patellar cartilage due to the smaller number of voxels of the bone-cartilage interface. However, the registration of the bone-cartilage interface may be useful in long-term studies with osteoarthritis patients, since the shape of the bone-cartilage interface usually tends to remain fairly unaffected over time. Interestingly, the registration of the articular surface of the in vivo datasets led to larger errors than the registration of the bone-cartilage interface (Table 5.1). This is probably a consequence of larger segmentation errors at the articular surface, where the low contrast between the cartilage and the synovial fluid made the segmentation more difficult.

The sensitivity of the registration algorithm to segmentation errors has been analyzed in vitro. Segmentation errors of in vitro measurements were mostly found at the periphery of the cartilage and at the bone-cartilage interface. Registration errors of the (segmented) MRI datasets were smaller than in the simulations, especially in the CC direction, confirming the robustness of the algorithm against segmentation errors.

The evaluation of registration algorithms is a delicate question since, with few exceptions, errors cannot be directly calculated. One method which allows estimating errors is the point-based registration of fiducial points [Fitzpatrick98, Fitzpatrick01]. This algorithm is based on the rigid registration of accurately positioned fiducial points, which can be identified either anatomically or with external or surgically implanted markers. Registration errors can be estimated from errors in locating these fiducial markers. Fitzpatrick and collaborators [Fitzpatrick98, Fitzpatrick01] found in simulations that 50 markers located with a 0.3 mm error lead to a mean squared registration error of 0.087 mm^2 , which corresponded to a standard deviation of 0.30 mm (assuming zero mean for the errors). Using 3-5 surgically implanted fiducial markers, in vivo registration errors oscillated between 0.5 mm and 1 mm [Maurer97, West01].

Using in vitro measurements on a sheep brain, Lazebnik and collaborators [Lazebnik03] reported a mean registration error smaller than 0.54 mm using needle path and landmark points for registration of 1 mm^3 isotropic voxel datasets. Woods and collaborators [Woods98a, Woods98b] used consistency measurements on eight MR brain datasets of the same volunteer. In contrast to the method used in this study, they registered the eight images at the same time in order to minimize consistency errors.

5 Voxel based reproducibility of T_2 with a new registration algorithm

Depending on the registration algorithm, errors in consistency measurements ranging from 4 μm to 40 μm were found.

To the best of our knowledge only two registration methods have been applied to the cartilage and both are based on the registration of the subchondral bone. In the registration algorithm of Stammberger et al. [Stammberger00], the principal inertial axes of the source dataset are firstly aligned to the inertial axes of the target dataset and then elastically registered by the definition of a local, iteratively calculated force field. The intensity and direction of the local field are calculated at each iteration from the distance of each voxel of the source dataset to the target surface. This method is a first attempt to deal with the problem of elastic registration of the cartilage and is, therefore, considerably more (algorithmically) complex and less time-efficient than any rigid-registration approaches. In addition, the algorithm cannot deal with datasets in which some surface voxels are missing in one of the two acquisitions (e.g. due to slightly different slice positioning), and it is very sensitive to the result of the alignment of the principal inertial axes.

A more recent approach is the one of Carballido-Gamio et al. [Carballido-Gamio08], which uses a shape-context-based registration algorithm to register the entire subchondral bone. In this registration algorithm, the same number of landmarks is identified in both the target and the source datasets. For each selected landmark in each dataset a coarse histogram of the relative distribution of the other landmarks in the same dataset is generated. Each landmark in the source dataset is associated to a landmark in the target dataset by maximizing the histogram similarity of all pairwise associations. Once this association has been performed, the transformation is calculated, which transforms the source landmarks to their corresponding landmarks in the target dataset. The principal advantage of this method is that it allows inter-individual registration of datasets. However this method is time consuming, the registration error is not available and the robustness of the method against the number of landmarks and their distribution must be investigated.

5.4.3 Reproducibility of cartilage T_2

Patellar cartilage is an important entity in the diagnosis of OA. Recent publications demonstrated a more frequent involvement of the patellofemoral joint in the process of OA than the tibiofemoral joint [Duncan06, Hinman07]. T_2 values in the patellar cartilage investigated in this study showed a distribution comparable to previously published data [Dardzinski97, Mosher00, Liess02, Mosher04a, Glaser06, Glaser07, Koff09]. In the radial zone, which represents 60%-80% of the deepest cartilage, the collagen fibrils are mostly arranged perpendicular to the bone-cartilage interface (and also to the magnetic field), so that it presents the lowest T_2 values (range: 20 ms at the bone-cartilage interface to 40 ms near to the transitional zone) [Dardzinski97, Mosher00, Liess02, Glaser02]. The transitional zone, which occupies the 25%-35% of the cartilage, is characterized by a random organization of fibrils resulting in a higher percentage of collagen fibrils oriented in the magic angle so that T_2 values further increase to 40-50 ms. The tangential zone of the cartilage (5%-10%) is characterized by orientation of collagen parallel to the articular surface [Glaser02], but it is not resolved by the image resolution of this measurements [Dardzinski97, Glaser02].

A rigid-registration algorithm offers a practical approach, since no substantial deformation of the cartilage is expected in short-term studies on healthy volunteers [Eckstein98b, Liess02]. In long-term studies with OA patients the registration method based on the overlap of the complete cartilage may lead to errors, since a cartilage loss of 4-6%/y is normal (see Section 3.3.1). Nevertheless, the

5.4 Discussion

registration of bone-cartilage interface may be still useful for long-term studies, since its shape usually remains fairly unaffected over time.

The combination of the measurement errors of T_2 caused by the low SNR, the errors from differences in T_2 due to magic-angle effects, and the errors due to the registration and interpolation lead to a mean CV of 10.1% and a 90% confidence interval of 29.4%. The CVs clearly showed spatial differences in cartilage. The statistically significantly larger CVs in the regions situated close to the AS may be explained by the presence of partial-volume effects. The large T_2 of the synovial fluid (between 400 and 600 ms [Düewell95]) leads to contamination of cartilage T_2 values by increasing T_2 of all voxels affected by partial-volume effects. Lowest CVs in T_2 (mean CV of 7.2%) were found in the central part of the patellar cartilage, where collagen fibres are predominantly oriented radially, i.e. perpendicular to the bone-cartilage interface and therefore to the external magnetic field. Near to the bone-cartilage interface the reproducibility of T_2 probably decreases since the characteristic low T_2 values and water content in this region cause the SNR to drop (see Section 4.3.3 and Fig. 4.6). In the periphery the CVs increased up to 11.0%, presumably due to partial-volume effects being more pronounced in the (thinner) periphery of the cartilage.

Although the T_2 values in articular cartilage are dominated by the orientation of the collagen fibrils in the external magnetic field, the magic-angle effect is not a significant factor for the reproducibility of T_2 . As the registration of the patellar datasets demonstrated, repositioning of the knee results only in small rotations of the patella (mean rotation angle of 2.5°), which cause errors lower than the measurement errors.

Since the T_2 relaxation time was not measured with different orientations, it is not possible to give any direct estimation of the magic-angle effect in our data. However, the results of previously published studies [Xia98, Mosher01], which have quantified the magic-angle effects in cartilage, can be used to give a worst case estimation of the changes in T_2 . In vivo at 3 T, Mosher et al. [Mosher01] used sagittal images of the femoral cartilage to assess the variations in T_2 with fibril orientation. Based on Fig. 3 of Mosher et al. [Mosher04a], the worst-case change of T_2 caused by a rotation angle of 2.5° (which is the mean rotation angle needed in our study to register two datasets), is around 3%. If we consider the largest T_2 times at the articular surface of 55 ms (again as worst-case estimation, Fig. 5.2), the resulting magic-angle-related error in T_2 , δT_2 , is 1.7 ms, which is lower than the expected noise-induced T_2 error of 4.2 ms due to the low SNR (see Chapter 4).

A similar estimation can be obtained assuming the heuristic dependence of T_2 with the orientation introduced by Xia [Xia98],

$$T_2(\theta) = T_2^{\min} + (T_2^{\max} - T_2^{\min}) \left(3 \cos^2(2\theta) - 1 \right)^2, \quad (5.5)$$

with T_2^{\min} and T_2^{\max} being the minimum and maximum T_2 values measured in a voxel for varying orientations θ . The infinitesimal variation $dT_2(\theta)$ due to an infinitesimal change in the orientation $d\theta$ is

$$\frac{dT_2(\theta)}{d\theta} = -\frac{3}{4} (T_2^{\max} - T_2^{\min}) \sin(2\theta) \left(3 \cos(2\theta) + 1 \right), \quad (5.6)$$

which is zero at 0 , $\pi/2$ and the magic angle. The maximum variation of $T_2(\theta)$ takes place for an angle of 25.5° with a variation rate of $|dT_2(\theta)/d\theta|_{\max} = 1.68 (T_2^{\max} - T_2^{\min})$. This maximal variation allows estimating an upper bound to δT_2 due to a small rotation angle, $\Delta\theta$,

$$\delta T_2 \leq \left| \frac{dT_2(\theta)}{d\theta} \right|_{\max} \Delta\theta = 1.68 (T_2^{\max} - T_2^{\min}) \Delta\theta \leq 1.68 (\max(T_2) - \min(T_2)) \Delta\theta, \quad (5.7)$$

5 Voxel based reproducibility of T_2 with a new registration algorithm

where $\max(T_2)$ and $\min(T_2)$ refer to the maximum and the minimum T_2 in the *whole* cartilage respectively, which for the patellar cartilage are 25 and 50 ms (Fig. 5.2). For a rotation of 2.5° , which is the averaged rotation used to register two datasets, this upper bound result in $\delta T_2 \leq 1.8$ ms, which is approximately one-half of the T_2 measurement error due to the low SNR (see Chapter 4). It must be pointed out that both estimations of the maximal δT_2 are worst-case estimations, and normally the errors in T_2 due to knee reposition are much lower than the measurement errors.

It is very interesting that the reproducibility (CVs) obtained by pixel-based analysis using 3D registration in this study are of comparable order of magnitude to reproducibility data obtained by former 2D region-based analysis without registration. In the 2D-method, each segmented slice of the cartilage is divided into the same number of regions. It is assumed that these regions occupy the same position in all images, so that no registration is needed. In the region-based method the reproducibility of each region is assessed with the mean root square of the mean T_2 values of this region in all reproducibility measurements.

The T_2 reproducibility of the region-based approach in the patella has been analyzed in several studies [Glaser06, Glaser07]. In a first systematic study [Glaser06] a regional analysis of patellar cartilage T_2 reproducibility was performed using identical sequences as in this article; a mean error of $(4.4 \pm 1.4)\%$ in the central part and of $(5.4 \pm 1.8)\%$ in the peripheral facets was reported. In a subsequent study, Glaser et al. [Glaser07] investigated global and regional T_2 reproducibility of patellar cartilage at 1.5-T and 3-T. Mean global and regional reproducibility errors for T_2 were $(3.5 \pm 0.4)\%$ and $(8.6 \pm 2.6)\%$ at 1.5-T and $(3.3 \pm 0.6)\%$ and $(9.7 \pm 3.4)\%$ at 3-T. Recently, Koff et al. [Koff09] analyzed the inter- and intraobserver T_2 reproducibility in the patellar cartilage globally and in layers (deep, middle and superficial). In this study, slightly lower global and regional CVs than in the intersession reproducibility studies [Glaser06, Glaser07] were found (global intraobserver CV 1.9%, interobserver CV 3.3%).

Since the region-based method uses averaged T_2 values to assess the reproducibility, better CVs are expected than when using a voxel-based reproducibility analysis. However, our work demonstrates that the voxel-based CVs are only slightly larger than the region-based CVs, making it possible to apply voxel-based methods for monitoring of the cartilage, which can increase the diagnostic sensitivity of T_2 measurements (see Chapter 6). For instance, the 3D method must be expected to be superior if very small lesions occur (lesions substantially smaller than the 2D regions) or if pathological changes manifest as increased T_2 variability within the region (without changing the mean T_2 value of this region).

5.5 Further applications of the registration algorithm

The registration algorithm presented in this chapter has been used in other studies of the cartilage apart from the ones described in this and the next chapter. Since a detailed description of these studies would take much space and depart from the scope of this thesis, only the principal results are outlined here.

5.5.1 Reproducibility of cartilage thickness

In quantitative cartilage morphology the progression of OA is assessed by the changes in the cartilage volume and mean thickness measured in follow-up examinations (see Section 3.3.1). However, due

5.5 Further applications of the registration algorithm

to their global character these parameters are not very sensitive to detect focal lesions in follow-up examinations of the cartilage. Using the thickness at a voxel basis for the detection of focal lesions would be possible only if the reproducibility of thickness is known at a voxel basis. Therefore, aim of this study was to assess the voxel-based reproducibility of the thickness of the cartilage.

In close analogy to the study of T_2 reproducibility presented in this chapter, 6 healthy volunteers were imaged at 7 different time points with a FLASH WE sequence with the imaging parameter described in section 5.2.3. Cartilage was segmented and the bone-cartilage interface and articular surface automatically separated for calculation of the thickness. Cartilage thickness was calculated for each voxel at the bone-cartilage interface with two methods: the minimal distance, which is the minimal distance from each voxel at the bone-cartilage interface to the articular surface, and the normal-based distance, which is the distance from each voxel at the bone-cartilage interface to the articular surface along the normal vector to the bone-cartilage interface at each voxel.

CVs for the thickness were calculated after registration, similarly as for T_2 (see Section 5.1.4). Median CV over all volunteers and all registrations was 12.80% with the minimal distance and 14.47% with the normal-based distance. To study regional variations all bone-cartilage interfaces were divided into an identical number of regions (6 in the CC direction and 4 in the LR direction). All voxels pertaining to the same region were pooled together, and their average CV used to characterize the region (Fig.).

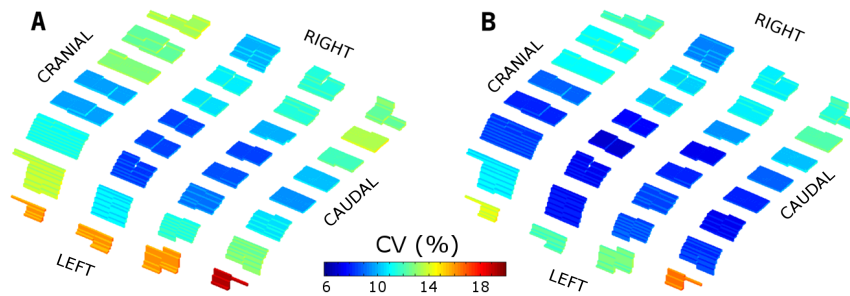


Figure 5.5: Regional differences in the reproducibility of thickness with the minimal distance (A) and the normal-based distance (B). All bone-cartilage interfaces have been divided into same number of regions ($6(\text{CC}) \times 4(\text{LR}) = 24$). Regions were selected by equally dividing the number of voxels. The median of the absolute value of the CV of all voxels belonging to the same region in all patellae was used to characterize errors in each region.

5.5.2 Cartilage deformation after exercise

Alterations in cartilage volume, maximal thickness and mean thickness have been reported as response of cartilage to mechanical load after different types of exercises [Eckstein00, Stammberger00]. A voxel-based analysis of the changes in cartilage thickness after exercise can help to identify the load areas of the cartilage and may be useful to evaluate the risk of certain exercises for OA.

10 healthy volunteers without any episode of knee pain in the last three years ($n = 5$ male and $n = 5$ female, mean age of 23 ± 5 y), were recruited for this study. Each volunteer was examined in four

5 Voxel based reproducibility of T_2 with a new registration algorithm

different imaging sessions. In each image session sagittal high-resolution FLASH WE images of the volunteers (image resolution $0.31 \times 0.31 \times 1.5 \text{ mm}^3$, the remaining MR parameters as indicated in section 4.2.1), were acquired after 45 min at rest. Afterwards, volunteers were asked to perform one of the following tasks for 20 min: kneel, squat, bend and sitting on the calf. In each imaging session a different task was performed. Immediately after exercise, volunteers underwent imaging with the same FLASH WE sequence. To assess the degree of recovery of the cartilage, a third MRI with the FLASH sequence was performed after one hour at rest.

Femoral, patellar and tibial (medial and lateral) cartilages of all volunteers were segmented in all images. In each segmented cartilage the bone-cartilage interface and the articular surface were automatically identified and cartilage thickness calculated with the minimum distance method. The first image in each imaging session was considered as the baseline examination for comparison with the acquisitions after exercise and after one hour at rest. The bone-cartilage interface of the examinations direct after exercise and one hour after exercise were registered to the bone-cartilage interface of the baseline. After registration differences in thickness with respect to the baseline were calculated. Maps of the significant changes (changes larger than the reproducibility) were produced (Fig. 5.6).

Although a careful analysis of the results of this study must still be performed, first inspection of the data showed differentiated patterns of load for the different exercises and cartilages, thus indicating the feasibility and potential of the technique.

5.5.3 Interindividual model using clustering

Data illustrating interindividual variability in cartilage T_2 are of potential interest for the workup of cartilage disease in OA, e.g. by providing a base to differentiate any individual data set from a healthy reference. In this study we used a hierarchical clustering method for interindividual analysis of the T_2 of healthy human patellar cartilage.

Anatomical images for measurement of patellar cartilage thickness were acquired in 10 healthy volunteers with a T_1 -weighted FLASH WE sequence. Images for T_2 calculation were acquired with the MSME sequence with the same parameters given in section 4.2.1. After cartilage segmentation, T_2 maps were calculated with the NCEXP method (see Section 4.1). All segmented cartilage of the same patient were registered together and divided into regions: eight regions in the CC direction, three in the AP and nine in the LR direction. Regions were defined so that they contain approximately an equal number of voxels. The distribution of the T_2 values of all voxels in one region in all 10 volunteers was used to define a measurement of similarity, which varies between 0 (non T_2 value in common) and 1 (exactly the same distribution of T_2 values). Regions in the patella were grouped according to their similarity using a hierarchical clustering method. Quality of the clustering was assessed with the cophenetic correlation coefficient (ρ), which is 0 for inconsistent clustering and 1 for perfectly consistent clustering.

Distribution of T_2 allowed a clustering of data (Fig. 1) with ρ of 0.85. Clusters include regions which were neighbors and coincide with the expected anatomical regions of the patellar cartilage. This is noteworthy, since the similarity did not include any spatial information. Hierarchical clustering allows regional interindividual characterization of patellar cartilage T_2 . It may provide insight into interindividual differences and in their relationship to structural properties of the cartilage.

5.6 Conclusion

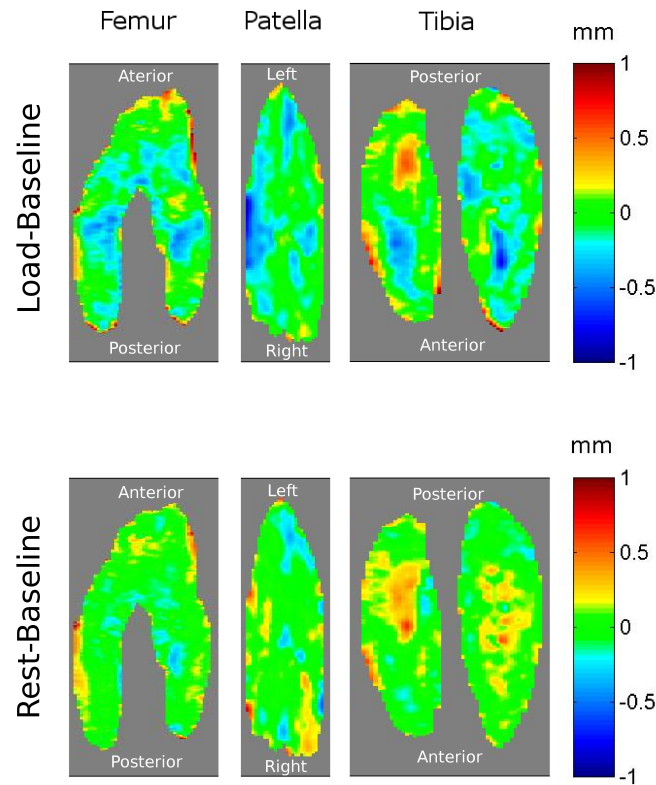


Figure 5.6: Regional differences in the reproducibility of thickness with the minimal distance (A) and the normal-based distance (B). All bone-cartilage interface have been divided into same number of regions ($6(CC) \times 4(LR) = 24$). Regions were selected by equally dividing the number of voxels. The median of the absolute value of the CV of all voxels belonging to the same region in all patellae was used to characterize errors in each region.

5.6 Conclusion

The registration algorithm proposed in this paper is simple to implement and provides an average registration accuracy lower than 25% of a voxel dimension. Registrations errors of the same order of magnitude were found for simulations, in vitro and in vivo measurements indicating robustness of the registration algorithm against segmentation errors. The voxel-based reproducibility of T_2 of patellar cartilage was in the same order of magnitude as previously published region-based or global reproducibility data, with a median CV of 10.1%. Reproducibility clearly had regional differences. Largest CVs of 15.5% were found near the articular surface, whereas the central part of the cartilage showed the lowest CVs (7.2%). Lateral parts of cartilage presented a reproducibility of 11.3%. The data presented in this chapter represent the first milestone for the method to identify significant T_2 changes in follow-up examinations of cartilage in OA, which is described in chapter 6. The regis-

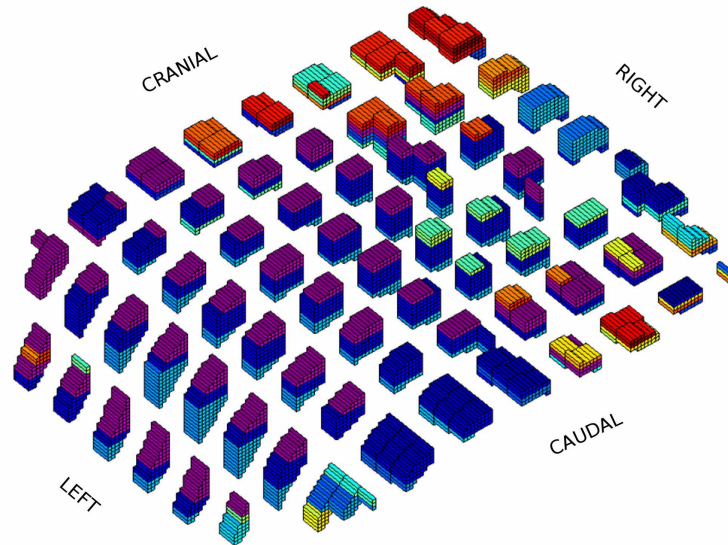


Figure 5.7: Result of hierarchical clustering of the patellar cartilage according to the T_2 values including the data of 10 healthy volunteers. Clusters of regions are encoded with different colors. Observe that the regions clustered together present coherent spatial location, although no spatial information was used in the clustering.

tration algorithm presented here has been shown to be of great use in many studies of the cartilage, where its application led to more detailed results.

Chapter 6 Application to disease monitoring

The relaxation time T_2 is known as a reliable indicator of the process of degeneration of the collagen cartilage matrix (see Section 3.2.1). However, the clinical relevance of the T_2 relaxation time in articular cartilage remains questioned due to the large acquisition time of the MSME sequences, the necessity of image processing and the difficulties in interpreting the T_2 maps. Nevertheless, little effort has been invested in exploiting the great advantage of T_2 quantification for follow-up examinations. Since OA has a long natural history, long-term follow-up examinations are required to diagnose the progression of OA, and the possible effect of any therapeutic intervention. Nowadays, a considerable limitation in the assessment of new therapies and drugs for OA is the absence of robust non-invasive methods for monitoring the progression of joint disease [Eckstein07].

In published longitudinal studies, changes in T_2 have been investigated using the bulk T_2 values or regional T_2 values in 2D ROIs, and in most cases without considering the error (reproducibility) in T_2 [Blumenkrantz04, Trattinig07a, Welsch08b, Welsch08c]. Few studies have been concerned with the reproducibility of bulk and regional T_2 in articular cartilage [Glaser06, Glaser07, Koff09]. In the ROI-based 2D method the cartilage is segmented in each measured slice and divided in the same number of regions (layers and sectors). The mean T_2 value in each region is used for comparison with the mean T_2 value in the equivalent region in the follow-up examination. Therefore, the ROI-based 2D method is insensitive to subtle changes which may occur between two follow-up examinations, so that much of the information contained in the T_2 maps is lost.

Trying to get the maximal information from follow-up T_2 examinations requires developing methods to detect changes in T_2 at a voxel basis. Such a voxel-based method unavoidable requires image registration and a good knowledge of the T_2 measurement errors to discriminate true T_2 changes. The concept of measurement errors is used here in a broad sense including all source of errors involved in the process of comparison of two datasets. Additionally to the SNR (see Chapter 4), which is the most important source of T_2 measurement errors, other sources of errors are the magic-angle effect (Section 5.4), the registration method (Section 5.3), the segmentation, the image interpolation ... The straightforward method to assess the measurement errors in T_2 is based on repeated acquisitions of healthy and OA-diseased volunteers. Since in short-term acquisitions no physiologic change in the cartilage is expected, the differences in T_2 are only a consequence of the measurement errors.

The objectives of this chapter are:

1. To establish a method for the calculation of the error in T_2 .
2. To develop a method for voxel-based monitoring of T_2 changes in the articular cartilage.
3. To demonstrate the value of the method on matrix-associated autologous chondrocyte transplanted (MACT) patients.

6.1 Methods

6.1 Methods

6.1.1 MRI measurement protocol

Measurements of the tibial and femoral cartilage were performed on two 1.5-T whole-body scanners (Magnetom Symphony and Magnetom Sonata; Siemens Healthcare, Erlangen, Germany) using a circularly polarized knee coil (the same model in both scanners). For T_2 measurements, the MSME sequence described in section 3.2.1 was used with the same parameters as described in section 4.2.1 with the only exception of the orientation of the slice, which was chosen sagittal. For cartilage segmentation, additional images were acquired with a T_1 -weighted FLASH WE sequence with the same slice positioning as for the MSME sequence. Segmentation of the tibial cartilage was performed in the FLASH dataset and transferred to the MSME dataset. T_2 was calculated for each voxel using the NCEXP method described in Section 4.1.

6.1.2 Volunteers

The error in T_2 was estimated on consecutive measurements of healthy and OA-diseased volunteers. Healthy volunteers ($n=12$, 7 male, 5 female, mean age (27 ± 9) y) with no history of knee injury or surgery and no episodes of knee pain in the past 3 years were examined at three different time points separated by 1 week. Radiologically diagnosed OA volunteers ($n=12$, 5 male, 7 female, mean age (52 ± 11) y. Kellgren-Lawrence 1 and 2), were examined two times in the same imaging session with repositioning of the knee between acquisitions. All volunteers were asked to rest 45 min before examination in order to avoid any influence from physical exercise [Eckstein98b]; all volunteers gave informed consent to participate in the study.

6.1.3 Calculation of the T_2 errors

All possible combinations of the images acquired on the same volunteer were registered using the algorithm described in Chapter 5. For consistency, the same notation of Chapter 5 is used, so that the first acquired dataset is called target, while the second (follow-up) dataset is termed source. After registration, the T_2 values of the source dataset were interpolated to the positions of the target voxels, so that for each target voxel there are two T_2 values, the original target T_2 , $T_{2,Trg}$, and the interpolated source T_2 , $T_{2,Src}$.

Since in consecutive acquisitions no change in the collagen-matrix occurred, all differences between $T_{2,Trg}$ and $T_{2,Src}$ in each voxel were only attributable to measurement errors (including all sources of errors). Therefore, the statistic of the pairs $(T_{2,Trg}, T_{2,Src})$ was used to characterize the T_2 measurement errors. All the pairs $(T_{2,Trg}, T_{2,Src})$ obtained in all healthy and OA-diseased volunteers, were pooled together and grouped according to their $T_{2,Trg}$ in units of 1 ms (from 10 to 11 ms, from 12 to 13 ms, ...). For each group the standard deviation of all their corresponding $T_{2,Src}$ values was calculated, $\sigma_{T_2}(T_2)$. The dependence on T_2 is kept explicit to remember that the standard deviation σ_{T_2} varies with the T_2 value.

The $\sigma_{T_2}(T_2)$ characterizes the measurement error in T_2 including all source of errors and allows identifying significant changes in T_2 . If one target voxel has a measured $T_{2,Trg}$ of T_2 , in the follow-up examination it is expected with a probability of 95% that the $T_{2,Src}$ in the same voxel takes values

between $T_2 - 2\sigma_{T_2}(T_2)$ and $T_2 + 2\sigma_{T_2}(T_2)$. However, if the measured $T_{2,src}$ lay outside of this interval the value of $T_{2,src}$ is likely to reflect an underlying change in the cartilage matrix.

A theoretical model for the calculation of $\sigma_{T_2}(T_2)$ has been developed (see Appendix C). The theoretical model only considers the errors due to the low SNR, which is by far the most relevant source of T_2 measurement errors. The great advantage of the theoretical model is that it does not require reproducibility measurements to calculate $\sigma_{T_2}(T_2)$. Only an accurate description of the T_2 errors due to SNR (CRLB, Appendix A), and the distribution of measured T_2 values are required. The $\sigma_{T_2}(T_2)$ calculated with the theoretical model has been compared with the $\sigma_{T_2}(T_2)$ obtained from repeated acquisitions of volunteers.

6.1.4 2σ -significance map

It remains to relate the significant changes in T_2 in follow-up examinations with the undergoing physiological changes in the cartilage. Although a significant reduction in T_2 is interpreted as a sign of healing, and a significant increase as an indication of worsening, knowledge of the range of healthy and pathological T_2 values is needed to accurately diagnose the complete healing. As cut-off between healthy and pathological the 99%-percentile of the distribution of all T_2 measured in the healthy volunteers was used.

The standard deviation $\sigma_{T_2}(T_2)$ and the cut-off of healthy T_2 can be combined in the 2σ -significance chart (Fig. 6.1). The $T_{2,Trg}$ and the $T_{2,Src}$ are plotted along the X- and Y-axis of the 2σ -significance chart, so that all possible outcomes in a follow-up examination are represented by a point in this map. The diagonal of the diagram represents the perfect concordance between $T_{2,Trg}$ and $T_{2,Src}$. The $T_2 \pm 2\sigma_{T_2}(T_2)$ interval around this line includes all pairs $(T_{2,Trg}, T_{2,Src})$, which do not undergo any significant change ($P < 0.05$, shaded area in Fig. 6.1). All points located outside of the $T_2 \pm 2\sigma_{T_2}(T_2)$ region represent a significant change. The cut-off of healthy T_2 is represented in the 2σ -significance chart as horizontal and vertical red lines, which divide the map into four parts, one for each combination of healthy and pathologic T_2 in the two measurements.

The resulting 2σ -significance chart has 7 different regions each one with a different diagnostic information (Table 6.1). The region I is the $T_2 \pm 2\sigma_{T_2}(T_2)$ region and includes all points which do not significantly change in the follow-up examination. The region II contains all points, which have pathologic $T_{2,Trg}$ and significantly increased pathologic $T_{2,Src}$, thus representing a worsening of the voxel. Points in region III have a healthy $T_{2,Trg}$ but a pathologic $T_{2,Src}$, thus representing voxels falling ill in follow-up. Points in region IV show healthy T_2 in both examinations but with significantly increased $T_{2,Src}$. This might be a first sign of a pathological process in this voxel. On the contrary, region V represents all voxels with healthy values in both examinations but with significantly reduced $T_{2,Src}$. Region VI comprises all voxels with pathologic $T_{2,Trg}$ and healthy $T_{2,Src}$, i.e. healed voxels. In region VII are included all voxels, whose $T_{2,Src}$ although still pathologic is significantly reduced from the initial pathological $T_{2,Trg}$. Therefore points in region VII represent voxels most likely in the process of healing.

6.1.5 Evaluation in MACT patients

To test the usefulness of the method, a small cohort of patients who had undergone MACT was randomly selected from the MACT patients included in an ongoing study in our department ($n = 5$, (31 ± 9) y). In all patients, MACT was performed in the femoral cartilage (medial femoral condyle

6.1 Methods

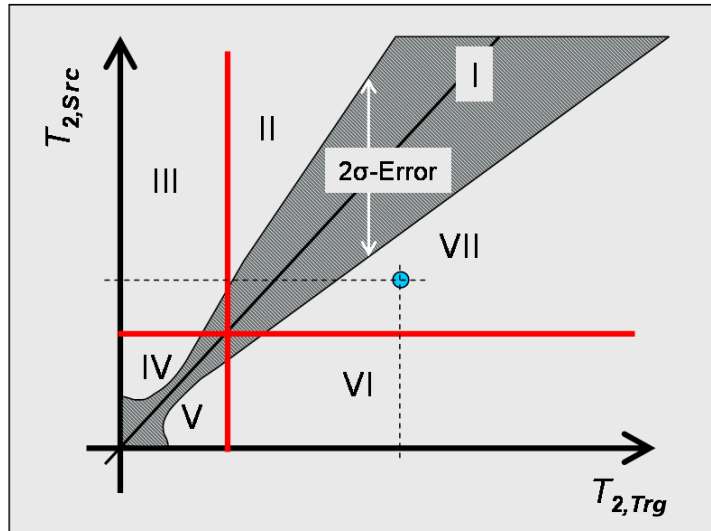


Figure 6.1: Construction of the 2σ -significance chart. $T_{2,Trg}$ and $T_{2,src}$ are plotted along the X- and Y-axis respectively. Each voxel in a follow-up examination is represented as a point in this map. The red straight lines represent the 99%-percentile of all healthy T_2 . The diagonal line represents the perfect concordance between $T_{2,Trg}$ and $T_{2,src}$. The $T_2 \pm 2\sigma_{T_2}(T_2)$ region is represented by the dashed area in the figure. The diagram presents 7 different regions with different diagnostic information (see text for explanation).

$n=3$, lateral femoral condyle $n=2$). At surgery, a sample was taken from the collagen scaffold used for cartilage regeneration. Histological cuts of the scaffold samples were stained with Toluidine blue O for cell counting with a light microscope. In each field the total number of cells, the number of cells which were stained, the number of cells which did not stain and the number of apoptosed cells were counted.

The knee condition was assessed with the subjective knee evaluation form of the International Knee Documentation Committee (IKDC) [Irrgang01] before surgery and 3, 6 and 12 months after surgery. The scoring of the IKDC is summarized in a number ranging from 0, for the lowest level of function or highest level of symptoms, to 100, when neither symptoms nor limitations of activities of daily living or sports are present.

All patients were MRI follow-up examined 1.5, 3, 6 and 12 months after intervention using the same protocol described in section 6.1.1. The first examination of each patient was considered as the baseline for comparison with all posterior follow-up examinations. In the baseline examination, the regions of pathologic T_2 values (i.e., T_2 larger than the cut-off of healthy T_2), were identified as the baseline lesion. Each posterior follow-up examination was registered to the baseline. After registration, all the pairs formed by the T_2 values of the baseline and the follow-up examinations were plotted in the 2σ -significance chart and classified according to the region they occupied (Fig. 6.4). This classification allowed plotting color-encoded significance maps of the cartilage.

The mean significant T_2 change, ΔT_2 , which is defined as the average of all significant differences in T_2 between the follow-up and the baseline (i.e. including all voxels classified in regions II to VII),

Table 6.1: Regions in the 2σ -significance chart

| Region | Signif cant ($P < 0.05$) | $T_{2,Trg}$ (Baseline) | $T_{2,Src}$ (Follow-up) | Diagnosis |
|--------|-------------------------------|---------------------------|----------------------------|-------------------------|
| I | – | Healthy, Pathologic | Healthy, Pathologic | Unchanged |
| II | + | Pathologic | Pathologic | Pathologic but worsened |
| III | + | Pathologic | Healthy | Fall ill |
| IV | + | Healthy | Healthy | Healthy but worsened |
| V | + | Healthy | Healthy | Healthy but improved |
| VI | + | Healthy | Pathologic | Healed |
| VII | + | Pathologic | Pathologic | Pathologic but improved |

was used to characterize the global change which had occurred in the cartilage. The clinical value of ΔT_2 has been assessed by comparison with the results of histology and the IKDC form. The count of chondrocytes was correlated with the mean value of the measured ΔT_2 , $\langle \Delta T_2 \rangle$, averaged over the ΔT_2 in all follow-ups. The results of the IKDC were correlated with $\langle \Delta T_2 \rangle$ averaged over the follow-up measurement until the evaluation of the form (6 or 12 months).

6.2 Results

6.2.1 Calculation of the T_2 errors

The distribution of T_2 values measured in the healthy and OA-diseased volunteers is presented in Fig. 6.2. The total number of voxels included in the histograms are 899 000 for healthy and 538 000 for OA. The 99%-percentile of all healthy values was 75 ms.

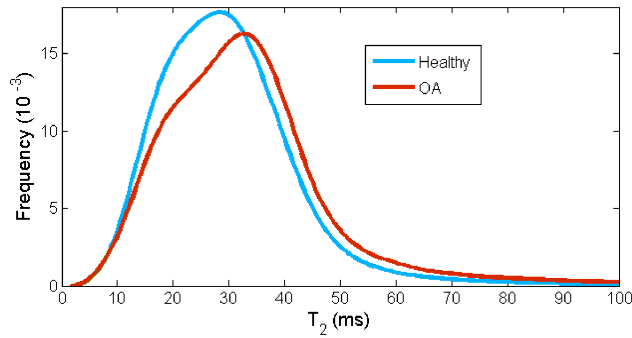


Figure 6.2: Measured distribution of T_2 in all healthy (blue) and OA-diseased (red) volunteers.

The T_2 measurement error $\sigma_{T_2}(T_2)$ is presented in Fig. 6.3. The dark-gray line in Fig. 6.3 is a spline fit to the measured points. Due to the high errors in $\sigma_{T_2}(T_2)$ for $T_2 \geq 120$ ms, $\sigma_{T_2}(T_2)$ is represented

6.2 Results

by a worst-case line for $T_2 \leq 120$ ms with values larger than all measured $\sigma_{T_2}(T_2)$. The theoretical curve calculated with the method described in Appendix C is plotted as a bright-gray line in Fig. 6.3 and coincides pretty well with the measured curve in the range between 10 and 50 ms, which include 92% of all healthy voxels.

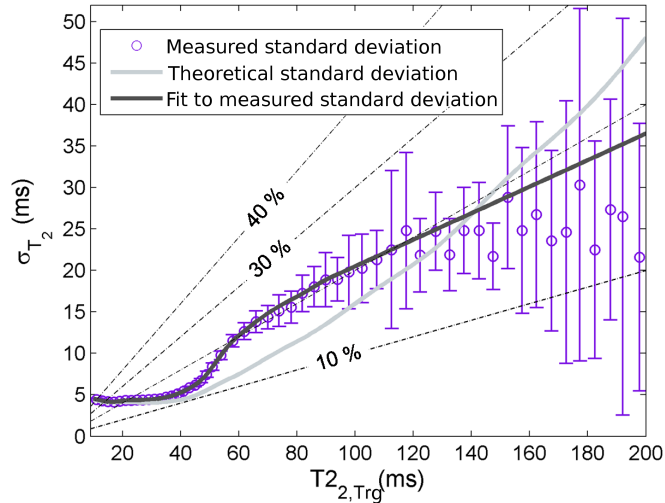


Figure 6.3: Measured $\sigma_{T_2}(T_2)$ in healthy and OA diseased volunteers. Error bars represent the 99% confidence interval of $\sigma_{T_2}(T_2)$. The dark-gray line is a spline fit to the measured data and the bright-gray line is the theoretical prediction calculated as described in Appendix C. The thin dash-dotted black lines indicate the relative error of T_2 .

6.2.2 2σ -significance chart

The 2σ -significance chart obtained with the $\sigma_{T_2}(T_2)$ and the 99%-percentile of all healthy T_2 values is presented in Fig. 6.4.

In Fig. 6.5, the use of the 2σ -significance chart is demonstrated in reproducibility measurements. The diagram represents the result of two reproducibility acquisitions in a healthy volunteer. 99.4% of all points ($N=19\,234$) were included under the red lines with $T_{2,Trg}$ and $T_{2,Src}$ lower than 75 ms. Region I included 93.4% all voxels, which is very near to the expected 95% if any change in the cartilage matrix occurred. The rest of the points were predominantly located in region IV (2.5%) and region V (3.6%).

6.2.3 Evaluation on MACT patients

The clinical evaluation of the patients and the result of the histology are summarized in the Table 6.2.

In Fig. 6.6, an example of an ACT patient in follow-up examinations is presented. The baseline lesions were identified in the baseline examination 1.5 months after intervention. The color-encoded

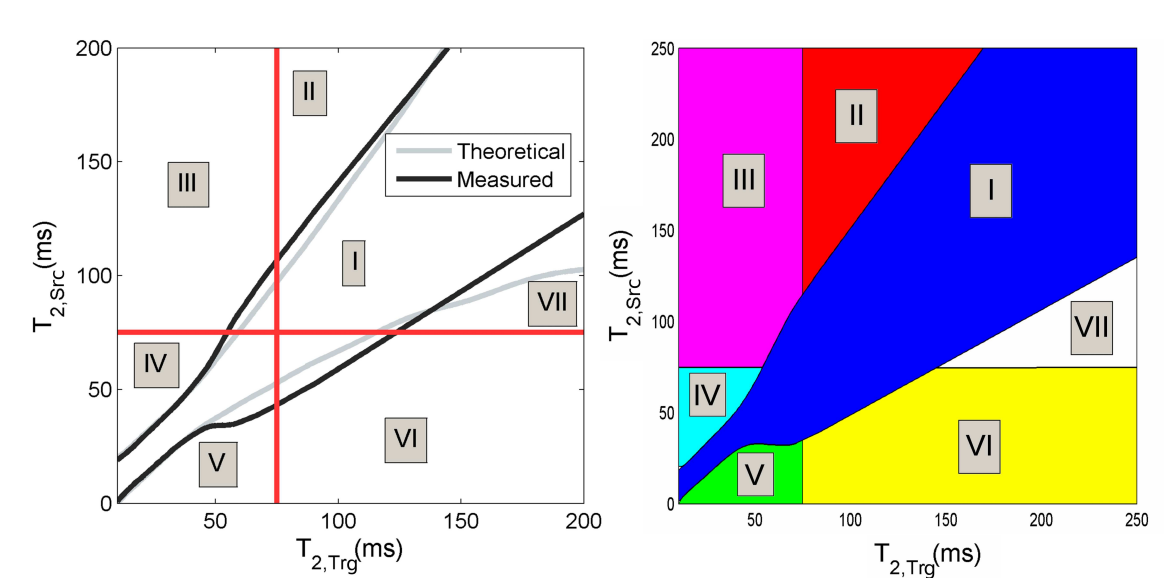


Figure 6.4: Left: Calculated 2σ -significance chart from reproducibility measurements (dark gray) and the theoretical calculation of the $2\sigma_{T_2}(T_2)$ (bright gray). Red lines represent the 99% percentile of the healthy T_2 values. Right: Color-encoding of the regions of the 2σ -significance chart, which is consistently used below in all significance maps of the cartilage.

significance maps of the cartilage in the first follow-up at 3 months showed worsening of the superficial lesion in the central part of the medial femoral cartilage (baseline lesion 1 in Fig. 6.6). Some voxels in the lesion presented significant increase of their initial pathologic T_2 values (red). Even more, many of the voxels near to the lesion 1 turned pathological (magenta) or presented significantly increased healthy T_2 values (turquoise). The baseline lesion in the lateral part of the medial femoral cartilage (indicated with the number 2 in Fig. 6.6) showed healing in the first follow-up. Interestingly, the voxels around lesion 2 showed significantly reduced T_2 values (green, yellow), which constitutes an additional indication of a healing process in this area. In the second follow-up examination at 6 months both lesions had normal T_2 values.

In Table 6.3 the cartilage volume (in baseline), the mean and standard deviation of T_2 in each examination and the mean significant T_2 change, ΔT_2 , for the follow-up examinations are summarized for the 5 MACT patients. The results of Table 6.3 are graphically represented in Fig. 6.7. The error bars represent the averaged 2σ error both in bulk T_2 and in ΔT_2 as calculated in the reproducibility measurements of healthy volunteers. Frequently the bulk T_2 did not present any significant difference to the mean T_2 in the baseline, whereas ΔT_2 was significantly changed.

The mean ΔT_2 , $\langle \Delta T_2 \rangle$, is presented in the last column of Table 6.3. $\langle \Delta T_2 \rangle$ showed a significant (t -test, $P < 0.05$) correlation ($r^2 = 0.92 \pm 0.13$) with the total number of chondrocytes and with the number of apoptosed cells ($r^2 = 0.89 \pm 0.15$) (Fig. 6.8). Non-significant correlation was found with the stained ($r^2 = 0.85 \pm 0.22$) and non-stained ($r^2 = 0.75 \pm 0.16$) number of chondrocytes (Fig. 6.8). A significant ($P < 0.05$) correlation ($r^2 = 0.72 \pm 0.20$) was found between $\langle \Delta T_2 \rangle$ and the results of the IKDC (Fig. 6.8).

6.3 Discussion

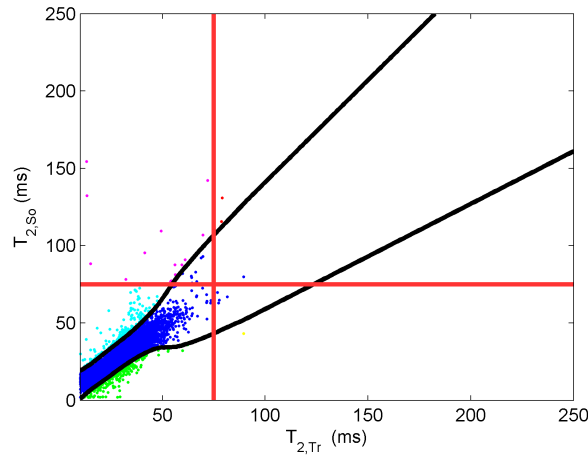


Figure 6.5: Example of 2σ -significance chart in a reproducibility measurement of a healthy volunteer.

Table 6.2: Summary of the results of the IKDC form and histology

| Patient | Preop. | IKDC form (%) ^{1,2} | | | | Total | Number of chondrocytes | | |
|---------|--------|------------------------------|---------|----------|---------|-------|------------------------|-----------|--|
| | | 3 month | 6 month | 12 month | Stained | | Non stained | Apoptosed | |
| 1 | 10.3 | 44.8 | 83.9 | 85.6 | 131 | 85 | 46 | 19 | |
| 2 | 6.9 | – | 39.1 | 73.6 | 56 | 47 | 9 | 13 | |
| 3 | 99.6 | – | 43.3 | 49.8 | 99 | 86 | 13 | 15 | |
| 4 | 34.5 | 32.2 | 43.7 | 52.9 | 13 | 9 | 4 | 1 | |
| 5 | 41.5 | – | 42.5 | 67.8 | 101 | 91 | 10 | 26 | |

¹Preop. = Preoperative

²– = no evaluation form available

6.3 Discussion

In this chapter, a voxel-based method for monitoring of disease progression based on careful calculation of errors in T_2 is proposed. The method aims to be a first attempt to deal with the problem of disease progression at a voxel basis and offers new diagnostic information, whose value has been preliminarily tested in a small group of MACT patients. Although the proposed method centers on the T_2 relaxation time, the principles used to develop the method are generally applicable and can be used with any other MRI parameter such as ADC, FA, T_1 , $T_{1\rho}$, ...

6.3.1 Calculation of the T_2 errors

For T_2 monitoring of the articular cartilage it is necessary to know the expected range of $T_{2,src}$ values in a follow-up examination for *each measured* $T_{2,Trg}$ value. The calculation of this range bases

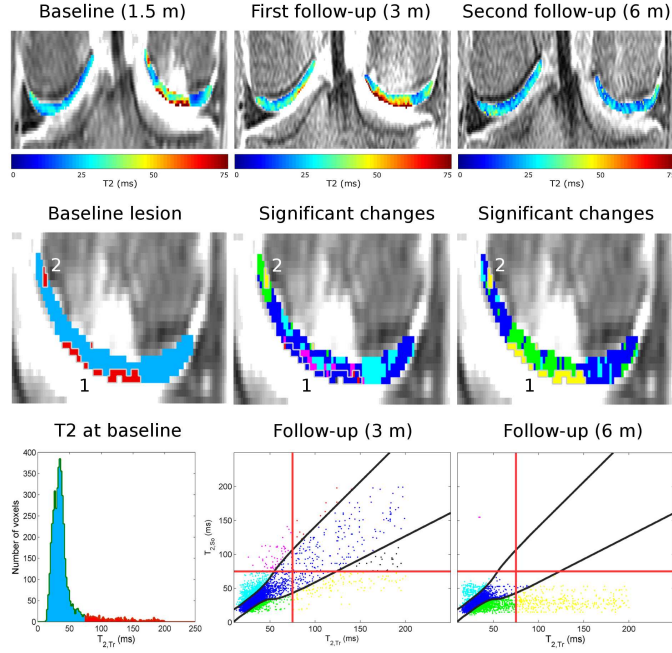


Figure 6.6: Follow-up examinations on a 39-year-old patient with a MACT in the right knee. First row. From left to right, T_2 maps of examinations at 1.5, 3 and 6 months after intervention. Second row. Significant changes. Baseline lesions were identified in the baseline (red voxels, hell gray contoured). Follow-up examination at 3 months showed healing of lesion 1 and worsening of lesion 2 with increased number of pathological voxels in its neighbour. Follow-up at 6 months demonstrated complete healing. MR images have been stretched in the vertical direction in order to improve visibility of the thin cartilage. Third row. Histogram of the T_2 values at baseline and 2σ -significance charts at the first and second follow-up.

on the empirical estimation of the joint probability function, $P(T_{2,Trg}, T_{2,Src} | \sigma)$ of Eq. [C.2], which gives for each $T_{2,Trg}$ the distribution of expected $T_{2,Src}$. The joint probability function is the only accessible probability function since the exact T_2 values, T_2^e , are unknown, and was estimated with reproducibility measurements.

In Appendix C a method for the calculation of the $\sigma_{T_2}(T_2)$ is presented, which solely uses the distribution of T_2 values as input. This means a great advantage, since it makes the method applicable without having to perform repeated measurements on the same subjects. The theoretical model relies on two assumptions. First, it is assumed a Rician distribution for the probability $P(T_{2,Trg} | T_2^e, \sigma)$ (Eq. [C.3]). This is justified with numerical simulations (see Section 4.2.4), where the T_2^e is known. Second, the method assumes that the CRLB (see Appendix A) correctly describes the accuracy of the fit method. Since all T_2 values have been calculated with the NCEXP method described in section 4.1, and the NCEXP method was compatible with the CRLB for almost every T_2 and SNR_0 level (see section 4.3.1), this assumption seems reasonable.

In the range of $T_2 \leq 50$ ms (including 92% of all voxels in healthy and OA-diseased cartilage) the

6.3 Discussion

Table 6.3: Summary of the T_2 changes in ACT patients

| Pat | Baseline (1.5 months) ^{1,2} | | Follow-up (3 months) ^{2,3} | | Follow-up (6 months) ^{2,3} | | Follow-up (12 months) ^{2,3} | | $\langle \Delta T_2 \rangle$ |
|-----|---|-------------|--|--------------|--|--------------|---|--------------|------------------------------|
| | Vol. | T_2 | T_2 | ΔT_2 | T_2 | ΔT_2 | T_2 | ΔT_2 | |
| 1 | 2.41 | 38.7 (15.4) | 35.7 (12.7) | -21.2 | 36.8 (12.7) | -21.9 | 34.8 (12.0) | -8.7 | -17.3 |
| 2 | 1.93 | 39.2 (12.8) | 36.4 (9.8) | 1.5 | 36.1 (10.2) | 1.0 | 33.6 (8.2) | -8.6 | -2.1 |
| 3 | 3.08 | 34.6 (10.4) | 35.1 (10.2) | 6.3 | 33.0 (9.9) | -2.4 | 31.3 (8.3) | -7.5 | -1.2 |
| 4 | 2.28 | 33.9 (10.1) | 35.5 (11.2) | 11.1 | 37.0 (11.6) | 13.1 | 36.8 (12.1) | 12.0 | 12.3 |
| 5 | 2.75 | 35.5 (11.8) | 38.7 (13.2) | 2.1 | 30.2 (8.7) | -22.5 | 36.1 (11.0) | -14.1 | -11.5 |

¹Vol. = Volume (in cm^3)

²Mean (bulk) T_2 (standard deviation) over the complete cartilage (in ms)

³ ΔT_2 : averaged significant T_2 change (in ms)

theoretical $\sigma_{T_2}(T_2)$, which only considered SNR as source of errors, was only slightly better than the measured $\sigma_{T_2}(T_2)$, which includes all sources of errors (see Fig. 6.3).

In the range from 50 to 140 ms, the measured $\sigma_{T_2}(T_2)$ was significantly larger than the theoretical $\sigma_{T_2}(T_2)$. There are two effects which can explain these differences. In diseased cartilage, large T_2 is a sign of disease, whereas in healthy cartilage it is more likely to be an artificially increased T_2 value due to partial volume effects with the synovial liquid, which has a T_2 value around 250 ms. A voxel affected by partial volume contributions is prone to be affected in a follow-up examination by a different amount of partial volume contributions, thus exhibiting larger standard deviations. This observation is consistent with the low reproducibility of T_2 observed at the articular surface of the patellar cartilage (Fig. 5.4).

For $T_2 \geq 140$ ms the small number of voxels resulted in large uncertainties for $\sigma_{T_2}(T_2)$ (observe the large error bars in Fig. 6.3), so that the fit to those points is less precise. Therefore, in the spline fit a worse-case line was used.

A last important remark about the strength of the magnetic field. All measurements presented in this thesis have been acquired on a 1.5-T scanner. Since the SNR grows linearly with the magnetic field, increasing the magnetic field to 3 T or to 7 T would cause a gain in SNR of a factor of 2 or 4.7. Usually, a better SNR is used to improve the spatial resolution. For example, at 3 T and 7 T an in-plane resolution of 70% and 46% of the resolution at 1.5 T can be achieved with the same SNR level as at 1.5 T. The method presented in this chapter suggests another possibility of using the gain in SNR. Since the error in T_2 also grows with the square root of the standard deviation of noise (see Eqs. [A.4,A.6] in Appendix A), the improvement in SNR can be invested in improvement of $\sigma_{T_2}(T_2)$ instead of increasing the resolution. This would allow a much more sensitive detection of the changes in T_2 .

6.3.2 2σ -significance chart

The 2σ -significance chart allows easily classifying the changes in T_2 that occurred between two acquisitions of the same subject. This classification differentiates between 7 possible outcomes, thus

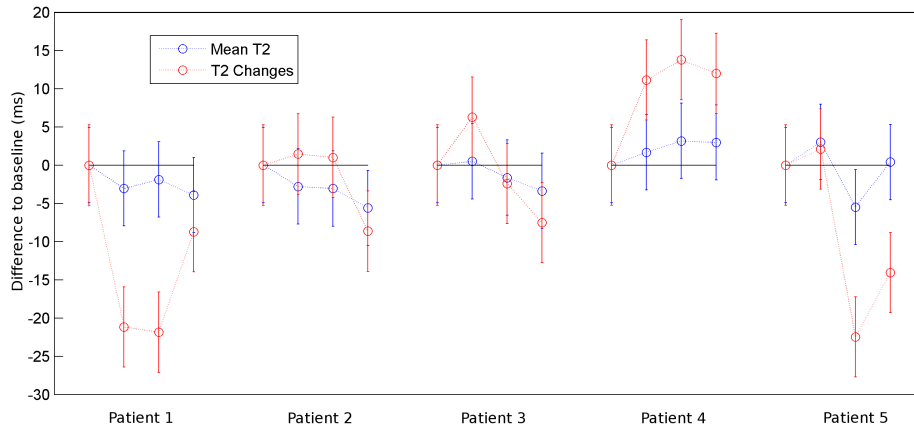


Figure 6.7: Changes in T_2 measured in all ACT patients. For each ACT patient the difference in mean T_2 to the baseline mean T_2 (blue lines), and the ΔT_2 (red lines) is represented (Table 6.3). Error bars represent the averaged 2σ error expected for the mean T_2 and the ΔT_2 . The black lines represent the data at baseline for comparison with the follow-up.

providing manifold diagnostic information. Perhaps the regions 2, 4, 5 and 7 are the most interesting for the diagnosis, since points in these regions represent a trend of healing or worsening before complete healing or before the onset of disease. Significance color maps of the cartilage calculated from the 2σ -significance chart represent a great simplification in the comparison of T_2 maps in follow-up examinations.

In healthy volunteers, the 2σ -significance chart presented around 95% of the voxels in the region I of the 2σ -significance chart, and the rest distribute equally between the regions IV and V (Fig. 6.5). However, in follow-up examinations of MACT patients, a much smaller fraction of voxels remains unchanged (mean fraction of unchanged voxels of 72.4% ranging from 60% to 87%), thus indicating that changes in the cartilage occurred. The significance color maps showed spatial coherence in the significant changes (Fig. 6.6), although the classification did not contain any spatial information. This again corroborates the idea that the significant changes in T_2 really reflect physiological changes in the cartilage.

6.3.3 Evaluation on MACT

Although T_2 has demonstrated to be sensitive to the degradation of the cartilage matrix, its use in the clinical routine has not yet become established. This is partially caused by the long acquisition times of the sequences for T_2 measurement, and more principally by the difficulties in the interpretation of the T_2 maps. As can be seen in Fig. 6.2, the distribution of T_2 in healthy and OA-diseased volunteers is very similar, so that global T_2 estimators, such as the bulk mean or standard deviation, cannot sensitively and specifically discriminate healthy from early-OA cartilage. Only if a focal lesion with high T_2 values is present, the T_2 maps can be easily interpreted. Indeed, quantitative T_2 mapping has been revealed to be more sensitive for the detection of focal lesions than the standard MRI protocol

6.3 Discussion

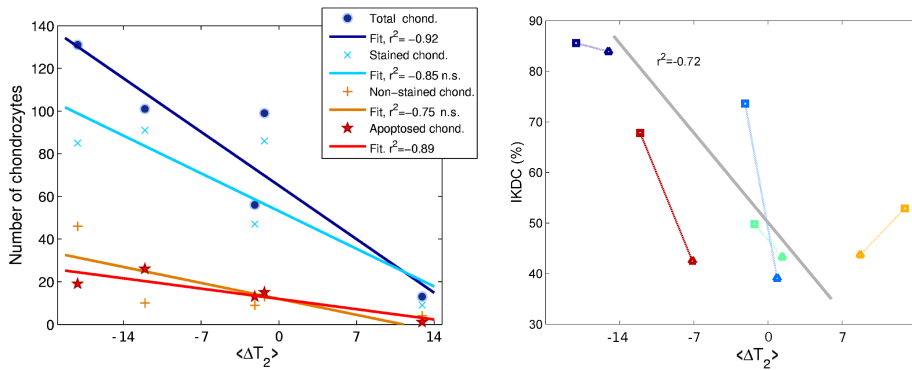


Figure 6.8: Left: The total number of chondrocytes (dark blue), the number of stained chondrocytes (bright blue), the number of non-stained chondrocytes (bright brown) and the number of apoptosed chondrocytes (red) are plotted against the $\langle \Delta T_2 \rangle$. Color lines represent the linear fit to the data; correlation coefficients are given in the legend. Right: The IKDC index versus $\langle \Delta T_2 \rangle$. Different colors were used for each patient. Triangles are used for the data at 6 months and squares for the data at 12 months. Thick gray line represents the linear fit to the data.

[Hannila07]. Twenty-eight lesions were detected both on MRI and T_2 maps, while eight lesions were only visible on T_2 maps. Even more, the lesions appeared significantly wider and thicker in T_2 than in standard images.

T_2 has a great potential in follow-up examinations which has been poorly exploited, essentially due to the lack of tools for comparison of T_2 maps acquired in successive examinations. Long-term studies of T_2 in articular cartilage used T_2 averaged either over the complete cartilage [Blumenkrantz04, Stahl07], or over a ROI defined on a lesion [Trattnig07a, Welsch08a, Domayer09, Welsch09]. In longitudinal studies on OA patients, the mean T_2 over the complete cartilage was not significantly increased in one-year follow-up [Stahl07], but in two-year follow-up examinations [Blumenkrantz04].

In MACT patients the T_2 relaxation time can assess the grade of cartilage repair, since T_2 is sensitive to the progressive restructuring of the collagen matrix, which occurs in a positive response to transplantation. Therefore, in follow-up studies of MACT patients it is a usual practice to use the mean T_2 over a ROI covering the full thickness (or a fraction of the thickness) of cartilage repair tissue. This ROI-based T_2 value is compared with the averaged T_2 measured in an analogous ROI defined on adjacent healthy cartilage [Trattnig07a, Welsch08a, Domayer09, Welsch09]. Significant changes of mean T_2 in ROIs defined on the cartilage repair tissue was found in the first year after transplantation and non-significant differences were found in the second year after transplantation [Trattnig07a, Welsch08a, Welsch09]. This change was more evident near the bone-cartilage interface than at the articular surface [Trattnig07a, Welsch08a, Welsch09].

In follow-up examinations the use of the mean T_2 (either over the complete cartilage (bulk) or over a ROI) to assess changes in cartilage has the advantage of being straightforward to calculate, but represents a coarse and not very sensitive measure of the changes undergoing in cartilage. The method presented in this chapter requires more image processing (which is performed automatically within few minutes once the segmentation is completed), but provides more diagnostic information. In color-encoded significance maps the areas of significant changes can be easily identified in the

whole cartilage, and not only in the lesion. This opens the possibility of investigating the reaction in adjacent healthy cartilage to the surgery and the process of healing.

As a measure of the global changes occurring in the cartilage, the mean significant T_2 change, ΔT_2 , has been introduced. ΔT_2 is positive when the follow-up examination has significantly larger T_2 values, and negative when the follow-up examination presents decreased T_2 values. If no change has occurred between both acquisitions a ΔT_2 near zero is expected, since in this case the 5% of the significant different voxels equally distribute between longer and shorter T_2 . Since a dataset of the femur has around 15 000 voxels the calculation of ΔT_2 involve at least 750 voxels.

The clinical value of ΔT_2 has been tested in 5 MACT patients. The average ΔT_2 , $\langle \Delta T_2 \rangle$, showed an excellent correlation with the number of chondrocytes in the transplanted allograft. The $\langle \Delta T_2 \rangle$ depends both on how large the significant change in T_2 was and on how fast it occurred. For example, patients 1 and 5 had similar decrements in ΔT_2 (around -22 ms), but at different time points, thus resulting in well differentiated $\langle \Delta T_2 \rangle$. The positive correlation between $\langle \Delta T_2 \rangle$ and the number of chondrocytes may indicate that the number of chondrocytes are critical for the restructuring of the implanted graft, and, thus, for the success of the transplantation. For example, patient 4, who presented a very low number of chondrocytes (Table 6.2), demonstrated systematically increased ΔT_2 (Table 6.3). On the contrary, patient 1, who had the largest number of chondrocytes, presented the fastest recuperation of all patients (Fig. 6.7). $\langle \Delta T_2 \rangle$ also demonstrated a positive correlation with the subjective knee evaluation as assessed with the IKDC form. Thus, the presented results indicate that changes in T_2 are closely related with the process of healing and the outcome of the patient.

6.4 Conclusion

In this chapter a method for monitoring the articular cartilage with follow-up examinations of T_2 is proposed. The method bases on careful calculation of errors in T_2 and offers new statistically significant information of disease progression, which would remain hidden with a more coarse evaluation based on global or regional mean T_2 . The method has been proven on a small cohort of MACT patients demonstrating a good correlation between the significant T_2 changes and the outcome of the patient. The average significant change in the follow-up was very well correlated with the number of chondrocytes in the transplanted graft. This might indicate that the number of chondrocytes is a very relevant parameter determining the success of surgery and the speed of the healing process. Although the diagnostic relevance of the method must still be confirmed in larger patient groups and, more important, on OA patients, the first promising results in MACT patients open a new way to look at T_2 in articular cartilage.

Chapter 7 Conclusions

This PhD thesis has been devoted to the development of a method for the voxel-based assessment of disease progression with MRI follow-up examinations of the T_2 relaxation time in articular cartilage. This method is based on an accurate and precise calculation of T_2 relaxation times in the articular cartilage, an accurate registration of cartilage datasets acquired in follow-up examinations and a deep knowledge of the T_2 measurement errors in the comparison of follow-up examinations.

In Chapter 4 it has been demonstrated that the traditional methods for T_2 calculation (linear regression (LR) and nonlinear fit to an exponential (EXP)) lead to a huge loss of accuracy at low T_2 and SNR_0 due to the Rician noise distribution in MR images. In simulations and phantom measurements, the T_2 values calculated with the traditional methods showed systematic deviations of up to 500% with respect to the true T_2 values. Therefore it was essential to introduce new voxel-based noise-corrected fit methods for accurate and precise T_2 calculation. Two new fit methods, SQEXP and NCEXP, have been introduced, which use the averaged decay of the measured signal intensity as the fit function for T_2 calculation. T_2 values calculated with the SQEXP and NCEXP methods did not deviate from the true T_2 value in average (i.e. they were very accurate). Even more, the T_2 values calculated with the NCEXP method showed a precision comparable with the best achievable precision (Cramér-Rao lower bound, Appendix A) for almost all T_2 and SNR_0 . Thus, NCEXP is the method of choice for T_2 calculation, since it has the best possible achievable precision and accuracy and provides the highest sensitive-to-change evaluation of T_2 values in follow-up examinations.

The other element necessary to implement the method presented in this thesis is the registration algorithm. Since in follow-up examinations the datasets are acquired with different orientations, it is necessary to align the data prior to comparison of their T_2 values on a voxel basis. The registration algorithm introduced in Chapter 5 is robust against segmentation errors and is able to register cartilage datasets with an error lower than 25% of the voxel size. This registration algorithm has been demonstrated to be very suitable for comparison of follow-up examinations where the morphology of the cartilage do not significantly change. Indeed, the low differences between the $\sigma_{T_2}(T_2)$ calculated from repeated acquisitions and from the theoretical model (Fig. 6.3), which assumes perfect registration, is very small for T_2 lower than 50 ms (92% of all voxels), thus indicating a very small contribution of any source of error other than the SNR.

With the fit method and the registration algorithm comparison of longitudinally acquired cartilage datasets becomes possible. Aim of the comparison of follow-up examinations is to detect changes in the measured parameter, which may be attributable to a physiological change in the cartilage. However, differences in T_2 between acquisitions occur due to the measurement errors in T_2 . Therefore, in order to discriminate true changes in T_2 a perfect knowledge of the T_2 measurement errors is mandatory. Errors have been characterized with repeated acquisitions of healthy and OA-diseased

patients.

The method presented in this thesis is based on the detection of significant changes in T_2 and aims to be a first step forward in the use of quantitative follow-up examinations on a voxel-basis. The advantages of the method are the new diagnostic information provided, the enormous simplification in the comparison of follow up examinations and the higher sensitivity-to-change than previous global evaluations based on the mean T_2 (which are up to now the only method used to evaluate follow-up examinations). The potential of the method has been demonstrated in MACT patients. In spite of the small number of patients included, the preliminary results are very promising. The mean change in T_2 represents in vivo evidence that the number of chondrocytes may be a critical parameter in the success of the MACT transplantation. Even more, the change in T_2 is also demonstrated to be significantly correlated with the subjective knee evaluation as assessed with the IKDC form .

In the near future it is planned to apply the method to OA-patients, to investigate the progression of disease. A validation of the preliminary results obtained in MACT patients in a larger collective would be of outstanding interest. Although the method has been developed for its use on T_2 follow-up examinations of the articular cartilage, its principles are completely general and can be adapted to use with any other MRI parameter and/or entity. In particular, it would be very interesting to use the method with the $T_{1\rho}$ or the dGEMRIC index, which are sensitive to the PG content of the cartilage. The theoretical method implemented in Appendix C is of great utility for the calculation of the measurement errors in the dGEMRIC index, since it avoids repeated injections of $\text{Gd}(\text{DTPA})^{2-}$ to healthy volunteers. A combination of significant changes in T_2 and $T_{1\rho}$ (or dGEMRIC) would allow for a deep insight in all changes undergoing in cartilage and might be a powerful tool to analyze the progression of OA.

Appendix A Cramér-Rao lower bound (CRLB)

Typically T_2 is calculated by sampling the signal intensity at different equidistant TEs, $\text{TE}_i = i \cdot \text{TE}$, with $i = 1, \dots, N$. If the noise-free signal intensity at the TEs Eq. [4.1] is denoted as $\vec{S} = (S_1, \dots, S_N)^t$, the probability of measuring the signal intensities $\vec{S}_M = (S_{M,1}, \dots, S_{M,N})^t$ can be written as

$$P_{S_M}(\vec{S}_M | \vec{S}, \sigma) = \prod_{i=1}^N \frac{S_{M,i}}{\sigma^2} \exp\left(-\frac{S_{M,i}^2 + S_i^2}{2\sigma^2}\right) I_0\left(\frac{S_{M,i} S_i}{\sigma^2}\right). \quad (\text{A.1})$$

In its simplest form, the Cramér-Rao lower bound states that the variance of any unbiased estimator is at least as high as the inverse of the Fisher information matrix, \mathcal{F} , [Brandt89]

$$\mathcal{F} = E \left[\vec{\nabla}_\theta \ln P_{S_M}(\vec{S}_M | \vec{S}, \sigma) \cdot (\vec{\nabla}_\theta \ln P_{S_M}(\vec{S}_M | \vec{S}, \sigma))^t \right] \quad (\text{A.2})$$

$$\sigma(\hat{\theta}_k)^2 \geq (\mathcal{F}^{-1})_{kk} \quad (\text{A.3})$$

where $k = 1, 2$ with $\theta_1 = S_0$ and $\theta_2 = T_2$, $E[\cdot]$ represents the expectation value with respect to the probability $P_{S_M}(\vec{S}_M | \vec{S}, \sigma)$, $\vec{\nabla}_\theta = (\frac{\partial}{\partial \theta_1}, \frac{\partial}{\partial \theta_2})^t$, and $\sigma(\hat{\theta}_k)$ represents the standard deviation of the unbiased estimator $\hat{\theta}_k$ of the parameter θ_k . Using the probability of Eq. [A.1] the Fisher information can be calculated analytically,

$$\mathcal{F} = \frac{1}{\sigma^2} \begin{pmatrix} \sum_{i=1}^N \left(\mathcal{J}\left(\frac{S_i}{\sigma}\right) - \frac{S_i^2}{\sigma^2} \right) \exp\left(-\frac{2i\text{TE}}{T_2}\right) & \sum_{i=1}^N i \frac{S_0 \text{TE}}{T_2^2} \left(\mathcal{J}\left(\frac{S_i}{\sigma}\right) - \frac{S_i^2}{\sigma^2} \right) \exp\left(-\frac{2i\text{TE}}{T_2}\right) \\ \sum_{i=1}^N i \frac{S_0 \text{TE}}{T_2^2} \left(\mathcal{J}\left(\frac{S_i}{\sigma}\right) - \frac{S_i^2}{\sigma^2} \right) \exp\left(-\frac{2i\text{TE}}{T_2}\right) & \sum_{i=1}^N i^2 \left(\frac{S_0 \text{TE}}{T_2^2} \right)^2 \left(\mathcal{J}\left(\frac{S_i}{\sigma}\right) - \frac{S_i^2}{\sigma^2} \right) \exp\left(-\frac{2i\text{TE}}{T_2}\right) \end{pmatrix}, \quad (\text{A.4})$$

where $\mathcal{J}(s)$ is defined as

$$\mathcal{J}(s) = \int_0^\infty x^3 \frac{I_1^2(xs)}{I_0(xs)} \exp\left(-\frac{x^2 + s^2}{2}\right) dx. \quad (\text{A.5})$$

It can be demonstrated that $\mathcal{J}(0) = 0$ and that $\mathcal{J}(s)$ is a strictly increasing function of s , whose asymptotic expansion is $\mathcal{J}(s) = s^2 + 1 + \mathcal{O}(s^{-2})$. In the asymptotic limit the Fisher information matrix reduces to that of a Gaussian distribution, so that the Cramér-Rao lower bound can be analytically calculated,

$$\sigma(\hat{T}_2)^2 = \frac{\left(\frac{\sigma T_2^2}{S_0 \text{TE}}\right)^2 (1 - r^N)(1 - r)^3 r^{-2}}{r^{2N} - N^2 r^{N+1} + 2(N^2 - 1)r^N - N^2 r^{N-1} + 1}$$

where $r = \exp(-\frac{TE}{T_2})$.

A last remark concerning the CRLB is that any bijective transformation of the random variable S_M , such as $S_V = S_M^2$, results in the same CRLB for T_2 and S_0 . Let us consider a general transformation to the variable S_M defined by $\vec{S}_V = f(\vec{S}_M)$, where the function f is bijective and at least of class \mathcal{C}^1 . In this case the Jacobian matrix for the transformation f , $J = \frac{\partial(S_{M,1} \dots S_{M,N})}{\partial(S_{V,1} \dots S_{V,N})}$, is well defined and f is invertible. The probability distribution of the variable \vec{S}_V is,

$$P_{S_M}(\vec{S}_M | \vec{S}, \sigma) d^N \vec{S}_M = P_{S_M}(f^{-1}(\vec{S}_V) | \vec{S}, \sigma) |J| d^N \vec{S}_V = P_{S_V}(\vec{S}_V | \vec{S}, \sigma) d^N \vec{S}_V, \quad (\text{A.6})$$

where $|\cdot|$ indicates the absolute value of the determinant. To demonstrate the equivalence of the CRLB it will be demonstrated that the Fisher matrix of S_M and $S_V = f(S_M)$ are the same,

$$\vec{\nabla}_\theta \ln P_{S_V}(\vec{S}_V | \vec{S}, \sigma) = \vec{\nabla}_\theta \ln \left(P_{S_M}(f^{-1}(f(\vec{S}_M)) | \vec{S}, \sigma) |J| \right) = \vec{\nabla}_\theta \ln P_{S_M}(\vec{S}_M | \vec{S}, \sigma), \quad (\text{A.7})$$

since the transformation of variables does not involve the parameters T_2 and S_0 . Thus, from the theoretical point of view, there is now drawback in using the SQEXP method for T_2 calculation.

Appendix B Noise-corrected exponential for images acquired with multi-channel coils

For multi-channels acquisitions where the image is reconstructed as the sum-of-squares of all images acquired with each single coil, the measured signal intensity of the final image, S_M , follows a noncentral Chi-square distribution,

$$P_{S_M}(S_M|S, \sigma, n) = \frac{S}{\sigma^2} \left(\frac{S_M}{S}\right)^n \exp\left(-\frac{S^2 + S_M^2}{2\sigma^2}\right) I_{n-1}\left(\frac{S_M S}{\sigma^2}\right), \quad (\text{B.1})$$

where S is the noise-free signal intensity of the final image, σ the noise standard deviation in each channel and n is the number of channels. The noise-corrected signal intensity is then defined analogously as with the single-channel acquisition (see Section 4.1, Eq [4.5]),

$$\Sigma(S, \sigma, n) = \sigma \sqrt{\frac{\pi}{2}} \frac{(2n-1)!!}{(n-1)! 2^{n-1}} M\left(-\frac{1}{2}, n, -2\alpha\right) \quad (\text{B.2})$$

where M is the confluent hypergeometric function [Slater72], and α has the same definition as in section 4.1, i.e. $\alpha = \left(\frac{S}{2\sigma}\right)^2$. Substituting the noise-free signal decay model of Eq. [4.1] in the noise corrected signal intensity Eq. [B.2] results in the noise-corrected exponential function, $\Sigma_{TE} = \Sigma(S_0 \exp(-TE/T_2), \sigma, n)$, which describes the decay of S_M with TE.

For nonlinear fit methods it is convenient to know the derivatives of Σ_{TE} with respect to T_2 and S_0 [Slater72],

$$\begin{aligned} \frac{\partial \Sigma_{TE}}{\partial T_2} &= \frac{\partial \Sigma}{\partial S} \frac{\partial S}{\partial T_2} = \frac{\partial \Sigma_{TE}}{\partial S} \frac{S_0 TE}{T_2^2} \exp\left(-\frac{TE}{T_2}\right), \\ \frac{\partial \Sigma_{TE}}{\partial S_0} &= \frac{\partial \Sigma}{\partial S} \frac{\partial S}{\partial S_0} = \frac{\partial \Sigma_{TE}}{\partial S} \exp\left(-\frac{TE}{T_2}\right), \\ \frac{\partial \Sigma}{\partial S} &= \sqrt{\frac{\alpha \pi}{2}} \frac{(2n-1)!!}{n! 2^{n-1}} M\left(\frac{1}{2}, n+1, -2\alpha\right), \end{aligned} \quad (\text{B.3})$$

and the asymptotic expansions [Slater72] of Eqs. [B.2,B.3],

$$\begin{aligned} \frac{\Sigma}{\sigma} &= 2\alpha^{\frac{1}{2}} + \frac{2n-1}{4}\alpha^{-\frac{1}{2}} + \frac{(2n-1)(2n-3)}{64}\alpha^{-\frac{3}{2}} + O(\alpha^{-\frac{5}{2}}) \\ \frac{\partial \Sigma}{\partial S} &= 1 - \frac{2n-1}{8\alpha} + \frac{(2n-3)(2n-1)}{128\alpha^2} + O(\alpha^{-3}). \end{aligned} \quad (\text{B.4})$$

For $n = 1$ these results coincide with the results for the single-channel acquisitions (Eqs. [4.7,4.8]).

Appendix C Derivation of the theoretical 2σ -significance chart

To estimate the errors in T_2 for the 2σ -significance chart the T_2 values measured in the same voxel in two consecutive acquisitions are used (perfect registration is assumed). For consistency in notation with Chapter 5, the T_2 values measured in the first acquisition will be denoted as target, $T_{2,Trg}$, and the T_2 values in the second as source $T_{2,Src}$.

The probability density of measuring a $T_{2,Trg}$ from an image with a noise level σ for a voxel whose exact T_2 value is T_2^e will be denoted as $P(T_{2,Trg}|T_2^e, \sigma)$. If a second measurement is performed on the same voxel, the joint probability of measuring $T_{2,Src}$ after $T_{2,Trg}$ is $P(T_{2,Trg}, T_{2,Src}|T_2^e, \sigma)$. Due to the statistical independence of the two measurements (i.e. of $T_{2,Trg}$ and $T_{2,Src}$), the joint probability is the product of the probabilities of $T_{2,Trg}$ and $T_{2,Src}$,

$$P(T_{2,Trg}, T_{2,Src}|T_2^e, \sigma) = P(T_{2,Trg}|T_2^e, \sigma) \cdot P(T_{2,Src}|T_2^e, \sigma). \quad (C.1)$$

In vivo, T_2^e remains unknown and only $T_{2,Trg}$ and $T_{2,Src}$ are known. The 2σ -significance chart is calculated from the distribution of the $T_{2,Src}$ after selecting all voxels with the same $T_{2,Trg}$ *independently* of their T_2^e . Therefore, the relevant distribution for the 2σ -significance chart is the summed joint probability distribution, $P(T_{2,Trg}, T_{2,Src}|\sigma)$,

$$P(T_{2,Trg}, T_{2,Src}|\sigma) = \int_0^\infty dT_2^e \rho(T_2^e) \cdot P(T_{2,Trg}|T_2^e, \sigma) \cdot P(T_{2,Src}|T_2^e, \sigma), \quad (C.2)$$

where $\rho(T_2^e)$ is the distribution of the T_2^e in the cartilage. Once this probability distribution is known the calculation of the 2σ -significance chart is straightforward, since for a given $T_{2,Trg}$ Eq. [C.2] is up to a constant the probability of measuring $T_{2,Src}$. Thus, the standard deviation of the distribution of $T_{2,Src}$ for a given $T_{2,Trg}$, which represents the range of expected errors for this given $T_{2,Trg}$, can be easily calculated.

In order to calculate the theoretical prediction of the 2σ -significance chart (Eq. [C.2]), it is necessary to know the probability of measuring $T_{2,Trg}$, $P(T_{2,Trg}|T_2^e, \sigma)$, and the distribution of T_2^e , $\rho(T_2^e)$. The distribution of $P(T_{2,Trg}|T_2^e, \sigma)$ is assumed to be a Rician distribution (Eq. [4.4]),

$$P(T_{2,Trg}|T_2^e, \sigma) = \frac{T_{2,Trg}}{\sigma_{T_2}^2(T_2^e, \sigma)} \exp\left(-\frac{T_{2,Trg}^2 + (T_2^e)^2}{2\sigma_{T_2}^2(T_2^e, \sigma)}\right) I_0\left(\frac{T_{2,Trg}T_2^e}{\sigma_{T_2}^2(T_2^e, \sigma)}\right), \quad (C.3)$$

where $\sigma_{T_2}(T_2^e, \sigma)$ is the standard deviation of the measured T_2 , which depends on T_2^e and σ . The validity of the Rician distribution has been empirically assessed with numerical simulations. The

function $\sigma_{T_2}(T_2^e, \sigma)$ can be well approximated by the Cramér-Rao lower bound (CRLB) as calculated in Appendix A (Fig. 4.3), since as demonstrated in Chapter 4 the fit to a noise-exponential function result in $\sigma_{T_2}(T_2^e, \sigma)$ compatible with the CRLB.

Once the probability of measuring $T_{2,Trg}$ is known, $\rho(T_2^e)$ can be calculated from the distribution of the measured T_2 values, $\rho_m(T_2, \sigma)$,

$$\rho_m(T_2, \sigma) = \int_0^\infty dT_2^e \rho(T_2^e) \cdot P(T_2|T_2^e, \sigma), \quad (C.4)$$

Technically, the calculation of the $\rho(T_2^e)$ reduces to solve the Fredholm equation of the first kind¹ [Polyanin08]. Fredholm integral equations of the first kind like Eq. [C.4] are a special case of ill-posed inverse problems. In ill-posed problems small changes in the experimental data, in this case $\rho_m(T_2, \sigma)$, due to measurement errors cause large instabilities in the solution. Handling with ill-posed problems requires careful use of regularization methods or other special numerical algorithms. In this case, the L-curve regularization method was used [Johnston00].

The calculation of the joint probability for the 2σ -significance chart (Eq. [C.2]) involves the following steps:

1. Calculate the CRLB for the noise level σ and define $P(T_{2,Trg}|T_2^e, \sigma)$.
2. Solve the Fredholm integral Eq. [C.4] using $\rho_m(T_2, \sigma)$.
3. Use the calculated $\rho(T_2^e)$ to numerically integrate Eq. [C.2].
4. Calculate for each $T_{2,Trg}$ the standard deviation of $T_{2,Trg}$ using $P(T_{2,Trg}, T_{2,Src}|\sigma)$.

The great advantage of this theoretical calculation is that it does not require successive acquisitions on a cohort of volunteers to assess the reproducibility. Indeed, it only bases on the calculation of the CRLB, which is easy to implement, and the distribution of the measured parameters. Therefore, this theoretical method allows an easy extension of the 2σ -significance chart to many other situations apart from cartilage and T_2 .

Although this method allows calculating a solution to Eq. [C.2], it is useful to gain some intuition about the joint probability. With this aim let us consider some approximations simplifying Eq. [C.2]. In the limit of $T_2^e \gg \sigma_{T_2}$ the Rician distribution can be very good approximated by a normal distribution.

$$P(T_{2,Trg}, T_{2,Src}|\sigma) = \int_0^\infty dT_2^e \frac{1}{2\pi\sigma_{T_2}^2(T_2^e, \sigma)} \cdot \exp\left(-\frac{(T_2^e - T_{2,Src})^2 + (T_2^e - T_{2,Trg})^2}{2\sigma_{T_2}^2(T_2^e, \sigma)^2}\right). \quad (C.5)$$

Changing to the variables $\mu_+ = (T_{2,Trg} + T_{2,Src})/2$ and $\mu_- = (T_{2,Trg} - T_{2,Src})/2$, the Eq. [C.5] takes the form,

$$P(T_{2,Trg}, T_{2,Src}|\sigma) = \int_0^\infty dT_2^e \frac{1}{2\pi\sigma_{T_2}^2(T_2^e, \sigma)} \cdot \exp\left(-\frac{(T_2^e - \mu_+)^2}{\sigma_{T_2}^2(T_2^e, \sigma)^2}\right) \cdot \exp\left(-\frac{\mu_-^2}{\sigma_{T_2}^2(T_2^e, \sigma)^2}\right). \quad (C.6)$$

¹Although Eq. [C.4] is very similar to a convolution equation, it differs from a convolution equation in that the probability $P(T_2|T_2^e, \sigma)$ is not a function of $T_2 - T_2^e$. In this context, the Fredholm equation represents a generalization of a convolution equation.

C Derivation of the theoretical 2σ -significance chart

In Eq. [C.6] the term depending on μ_+ and the term depending on μ_- are coupled through the measurement error in T_2 , $\sigma_{T_2}^2(T_2^e, \sigma)$. Let us also additionally assume the condition of constant $\sigma_{T_2}(T_2^e, \sigma) = \sigma$, which occurs when $d\sigma_{T_2}/dT_2^e \ll 1$ (i.e. the variation of sigma is much smaller than sigma). Under this approximation Eq. [C.2] is,

$$P(T_{2,Trg}, T_{2,Src} | \sigma) = \frac{1}{\sqrt{2\pi\sigma^2}} \exp\left(-\frac{\mu_+^2}{\sigma^2}\right) \int_0^\infty dT_2^e \frac{\rho(T_2^e)}{\sqrt{2\pi\sigma^2}} \cdot \exp\left(-\frac{(T_2^e - \mu_+)^2}{\sigma^2}\right). \quad (C.7)$$

The integral in Eq. [C.7] is the probability of measuring a T_2 of μ_+ (Eq. [C.4]),

$$P(T_{2,Trg}, T_{2,Src} | \sigma) = \frac{1}{\sqrt{4\pi\sigma}} \exp\left(-\frac{(T_{2,Trg} - T_{2,Src})^2}{4\sigma}\right) \cdot \rho_m((T_{2,Trg} - T_{2,Src})/2, \sigma). \quad (C.8)$$

Eq. [C.8] can be easily interpreted. The probability of measuring $T_{2,Trg}$ and $T_{2,Src}$ consecutively in the same voxel are given by a normal distribution of their difference with a standard deviation of 2σ , multiplied by the probability of measuring their mean.

Bibliography

- [Abragam04] Abragam A (2004). Principles of nuclear magnetism. Oxford University Press, New York, NY.
- [Akella01] Akella SV, Regatte RR, Gougoutas AJ, Borthakur A, Shapiro EM, Kneeland JB, Leigh JS, Reddy R (2001). Proteoglycan-induced changes in T1rho-relaxation of articular cartilage at 4T. *Magn Reson Med* 46:419–423.
- [Akella03] Akella SV, Regatte RR, Borthakur A, Kneeland JB, Leigh JS, Reddy R (2003). T1rho MR imaging of the human wrist in vivo. *Acad Radiol* 10:614–619.
- [Altman86] Altman R, Asch E, Bloch D, Bole G, Borenstein D, Brandt K, Christy W, Cooke TD, Greenwald R, Hochberg M (1986). Development of criteria for the classification and reporting of osteoarthritis. Classification of osteoarthritis of the knee. Diagnostic and Therapeutic Criteria Committee of the American Rheumatism Association. *Arthritis Rheum* 29:1039–1049.
- [Amin95] Amin AR, Di Cesare PE, Vyas P, Attur M, Tzeng E, Billiar TR, Stuchin SA, Abramson SB (1995). The expression and regulation of nitric oxide synthase in human osteoarthritis-affected chondrocytes: evidence for up-regulated neuronal nitric oxide synthase. *J Exp Med* 182:2097–2102.
- [Arden06] Arden N, Nevitt MC (2006). Osteoarthritis: epidemiology. *Best Pract Res Clin Rheumatol* 20:3–25.
- [Aydelotte88a] Aydelotte MB, Greenhill RR, Küttner KE (1988). Differences between subpopulations of cultured bovine articular chondrocytes, II: Proteoglycan metabolism. *Connect Tissue Res* 18:223–234.
- [Aydelotte88b] Aydelotte MB, Küttner KE (1988). Differences between subpopulations of cultured bovine articular chondrocytes, I: Morphology and cartilage matrix production. *Connect Tissue Res* 18:205–222.
- [Aydelotte92] Aydelotte MB, Schumacher BL, Küttner KE (1992). Articular cartilage and Osteoarthritis. Raven Press, New York, NY.
- [Bank00] Bank RA, Soudry M, Maroudas A, Mizrahi J, TeKoppele JM (2000). The increased swelling and instantaneous deformation of osteoarthritic cartilage is highly correlated with collagen degradation. *Arthritis Rheum* 43:2202–2210.
- [Bashir96] Bashir A, Gray ML, Burstein D (1996). Gd-DTPA2- as a measure of cartilage degradation. *Magn Reson Med* 36:665–673.
- [Bashir97] Bashir A, Gray ML, Boutin RD, Burstein D (1997). Glycosaminoglycan in articular cartilage: in vivo assessment with delayed Gd(DTPA)(2-)-enhanced MR imaging. *Radiology* 205:551–558.

Bibliography

- [Bashir99] Bashir A, Gray ML, Hartke J, Burstein D (1999). Nondestructive imaging of human cartilage glycosaminoglycan concentration by MRI. *Magn Reson Med* 41:857–865.
- [Bastin98] Bastin ME, Armitage PA, Marshall I (1998). A theoretical study of the effect of experimental noise on the measurement of anisotropy in diffusion imaging. *Magn Reson Imaging* 16:773–785.
- [Baur98] Baur A, Stähler A, Brüning R, Bartl R, Krödel A, Reiser M, Deimling M (1998). Diffusion-weighted MR imaging of bone marrow: differentiation of benign versus pathologic compression fractures. *Radiology* 207:349–356.
- [Bayliss83] Bayliss MT, Venn M, Maroudas A, Ali SY (1983). Structure of proteoglycans from different layers of human articular cartilage. *Biochem J* 209:387–400.
- [Bayliss99] Bayliss MT, Osborne D, Woodhouse S, Davidson C (1999). Sulfation of chondroitin sulfate in human articular cartilage. The effect of age, topographical position, and zone of cartilage on tissue composition. *J Biol Chem* :15892–15900.
- [Bella94] Bella J, Eaton M, Brodsky B, Berman HM (1994). Crystal and molecular structure of a collagen-like peptide at 1.9 Å resolution. *Science* 266:75–81.
- [Benninghoff25] Benninghoff A (1925). Form und bau der gelenkknorpel in ihren beziehungen zur funktion. *Z Zellforsch Mikrosk Anat* 2:783–825.
- [Berendsen62] Berendsen HJC (1962). Nuclear magnetic resonance study of collagen hydration. *J Chem Phys* 36:3297–3305.
- [Blumenkrantz04] Blumenkrantz G, Lindsey CT, Dunn TC, Jin H, Ries MD, M LT, Steinbach LS, Majumdar S (2004). A pilot, two-year longitudinal study of the interrelationship between trabecular bone and articular cartilage in the osteoarthritic knee. *Osteoarthritis Cartilage* 12:997–1005.
- [Bonny96] Bonny JM, Zanca M, Boire JY, Veyre A (1996). T_2 maximum likelihood estimation from multiple spin-echo magnitude images. *Magn Reson Med* 36:287–296.
- [Borthakur03] Borthakur A, Wheaton A, Charagundla SR, Shapiro EM, Regatte RR, Akella SV, Kneeland JB, Reddy R (2003). Three-dimensional T1rho-weighted MRI at 1.5 Tesla. *J Magn Reson Imaging* 17:730–736.
- [Borthakur06] Borthakur A, Mellon E, Niyogi S, Witschey W, Kneeland JB, Reddy R (2006). Sodium and T1rho MRI for molecular and diagnostic imaging of articular cartilage. *NMR Biomed* 19:781–821.
- [Brandt89] Brandt S (1989). *Statistical and computational methods in data analysis*. North-Holland publishing company, Amsterdam.
- [Brodsky08] Brodsky B, Thiagarajan G, Madhan B, Kar K (2008). Triple-helical peptides: an approach to collagen conformation, stability, and self-association. *Biopolymers* 89:345–353.
- [Brown98] Brown MP, West LA, Merritt KA, Plaas AH (1998). Changes in sulfatation patterns of chondroitin sulfate in equine articular cartilage and synovial fluid in response to aging and osteoarthritis. *Am J Ver Res* 59:786–791.
- [Buckwalter85] Buckwalter JA, Küttner KE, Thoner EJM (1985). Age-related changes in articular cartilage proteoglycans: Electron microscopic studies. *J Orthop Res* 3:251–257.
- [Buckwalter94] Buckwalter JA, Roughley PJ, Rosenberg LC (1994). Age-related changes in cartilage proteoglycans: Quantitative electron microscopic studies. *Microsc Res and Tech* 28:398–408.

- [Buckwalter98a] Buckwalter JA, Mankin HJ (1998). Articular cartilage: degeneration and osteoarthritis, repair, regeneration, and transplantation. *Instr Course Lect* 47:487–504.
- [Buckwalter98b] Buckwalter JA, Mankin HJ (1998). Articular cartilage. Part I: Tissue design and chondrocyte-matrix interactions. *Instr Course Lect* 47:600–611.
- [Bull92] Bull TE (1992). Relaxation in the rotation frame in liquids. *Prog NMR Spectrosc* 24:377.
- [Bundestamt08] Bundestamt S (2008). *Gesundheit - Krankheitskosten 2002 2004 2006*. Statistisches Bundesamt, Wiesbaden, Germany.
- [Burk86] Burk DL, Kanal E, Brunberg JA, Johnstone GF, Swensen HE, Wolf GL (1986). 1.5-T surface-coil MRI of the knee. *AJR Am J Roentgenol* 147:293–300.
- [Burstein93] Burstein D, Gray ML, Hartman AL, Gipe R, Foy BD (1993). Diffusion of small solutes in cartilage as measured by nuclear magnetic resonance (NMR) spectroscopy and imaging. *J Orthop Res* 11:465–478.
- [Burstein01] Burstein D, Velyvis J, Scott KT, Stock KW, Kim YJ, Jaramillo D, Boutin RD, Gray ML (2001). Protocol issues for delayed Gd(DTPA)(2-)-enhanced MRI (dGEMRIC) for clinical evaluation of articular cartilage. *Magn Reson Med* 45:36–41.
- [Bydder09] Bydder GM, Chung CB (2009). Magnetic resonance imaging of short T2 relaxation components in the musculoskeletal system. *Skeletal Radiol* 38:201–205.
- [Byers70] Byers PD, Contepomi CA, Farkas TA (1970). A post mortem study of the hip joint. Including the prevalence of the features of the right side. *Ann Rheum Dis* 29:15–31.
- [Carballido-Gamio08] Carballido-Gamio J, Link TM, Majumdar S (2008). New techniques for cartilage magnetic resonance imaging relaxation time analysis: texture analysis of flattened cartilage and localized intra- and inter-subject comparisons. *Magn Reson Med* 59:1472–1477.
- [Cicuttini00] Cicuttini F, Forbes A, Asbeutah A, Morris K, Stuckey S (2000). Comparison and reproducibility of fast and conventional spoiled gradient-echo magnetic resonance sequences in the determination of knee cartilage volume. *J Orthop Res* 18:580–584.
- [Cicuttini01] Cicuttini FM, Wluka AE, Stuckey SL (2001). Tibial and femoral cartilage changes in knee osteoarthritis. *Ann Rheum Dis* 60:977–980.
- [Cicuttini02] Cicuttini F, Wluka A, Wang Y, Stuckey S (2002). The determinants of change in patella cartilage volume in osteoarthritic knees. *J Rheumatol* 29:2615–2619.
- [Cicuttini04a] Cicuttini FM, Jones G, Forbes A, Wluka AE (2004). Rate of cartilage loss at two years predicts subsequent total knee arthroplasty: a prospective study. *Ann Rheum Dis* 63:1124–1127.
- [Cicuttini04b] Cicuttini FM, Wluka AE, Wang Y, Stuckey SL (2004). Longitudinal study of changes in tibial and femoral cartilage in knee osteoarthritis. *Arthritis Rheum* 50:94–97.
- [Cicuttini05] Cicuttini FM, Teichtahl AJ, Wluka AE, Davis S, Strauss BJ, Ebeling PR (2005). The relationship between body composition and knee cartilage volume in healthy, middle-aged subjects. *Arthritis Rheum* 52:461–467.
- [Clarke71] Clarke IC (1971). Articular cartilage: A review and scanning electron microscope study. 1. The interterritorial fibrillar architecture. *J Bone Joint Surg* 53B:732–750.
- [Cohen99] Cohen ZA, McCarthy DM, Kwak SD, Legrand P, Fogarasi F, Ciaccio EJ, Ateshian GA (1999). Knee cartilage topography, thickness, and contact areas from MRI: in-vitro calibration and in-vivo measurements. *Osteoarthr Cartil* 7:95–109.

Bibliography

- [Conaghan08] Conaghan PG, Dickson J, Grant RL (2008). Care and management of osteoarthritis in adults: summary of NICE guidance. *BMJ* 336:502–503.
- [Constantinides97] Constantinides CD, Atalar E, R ME (1997). Signal-to-noise measurements in magnitude images from NMR phased arrays. *Magn Reson Med* 38:852–857.
- [Cooper00] Cooper C, Snow S, McAlindon TE, Kellingray S, Stuart B, Coggon D, Dieppe PA (2000). Risk factors for the incidence and progression of radiographic knee osteoarthritis. *Arthritis Rheum* 43:995–1000.
- [Cova98] Cova M, Toffanin R, Frezza F, Pozzi-Mucelli M, Mlynárik V, Pozzi-Mucelli RS, Vittur F, Dalla-Palma L (1998). Magnetic resonance imaging of articular cartilage: ex vivo study on normal cartilage correlated with magnetic resonance microscopy. *Eur Radiol* 8:1130–1136.
- [Cushnaghan91] Cushnaghan J, Dieppe P (1991). Study of 500 patients with limb joint osteoarthritis. I. Analysis by age, sex, and distribution of symptomatic joint sites. *Ann Rheum Dis* 50:8–13.
- [Dardzinski97] Dardzinski BJ, Mosher TJ, Li S, van Slyke MA, Smith MB (1997). Spatial variation of T₂ in human articular cartilage. *Radiology* 205:546–550.
- [Dardzinski02] Dardzinski BJ, Laor T, Schmithorst VJ, Klosterman L, Graham TB (2002). Mapping T₂ relaxation time in the pediatric knee: feasibility with a clinical 1.5-T MR imaging system. *Radiology* 225:233–239.
- [David-Vaudey04] David-Vaudey E, Ghosh S, Ries M, Majumdar S (2004). T₂ relaxation time measurements in osteoarthritis. *Magn Reson Imaging* 22:673–682.
- [Deng07] Deng X, Farley M, Nieminen MT, Gray M, Burstein D (2007). Diffusion tensor imaging of native and degenerated human articular cartilage. *Magn Reson Imaging* 25:168–171.
- [Dietrich01] Dietrich O, Heiland S, Sartor K (2001). Noise correction for the exact determination of apparent diffusion coefficients at low SNR. *Magn Reson Med* 45:448–453.
- [Dietrich08] Dietrich O, Raya JG, Reeder SB, Ingrisch M, Reiser MF, Schoenberg SO (2008). Influence of multichannel combination, parallel imaging and other reconstruction techniques on MRI noise characteristics. *Magn Reson Imaging* 26:754–762.
- [Domayer09] Domayer SE, Welsch GH, Nehrer S, Chiari C, Dorotka R, Szomolanyi P, Mamisch TC, Yayon A, Trattig S (2009). T₂ mapping and dGEMRIC after autologous chondrocyte implantation with a fibrin-based scaffold in the knee: Preliminary results. *Eur J Radiol* .
- [Duewell95] Duewell SH, Ceckler TL, Ong K, Wen H, Jaffer FA, Chesnick SA, Balaban RS (1995). Musculoskeletal MR imaging at 4 T and at 1.5 T: comparison of relaxation times and image contrast. *Radiology* 196:551–555.
- [Duncan06] Duncan RC, Hay EM, Saklatvala J, Croft PR (2006). Prevalence of radiographic osteoarthritis—it all depends on your point of view. *Rheumatology (Oxford)* 45:757–760.
- [Dunn04] Dunn TC, Lu Y, Jin H, Ries MD, Majumdar S (2004). T₂ relaxation time of cartilage at mr imaging: comparison with severity of knee osteoarthritis. *Radiology* 232:592–598.
- [Duvvuri97] Duvvuri U, Reddy R, Patel SD, Kaufman JH, Kneeland JB, Leigh JS (1997). T₁rho-relaxation in articular cartilage: effects of enzymatic degradation. *Magn Reson Med* 38:863–867.
- [Duvvuri98] Duvvuri U, Kaufman JH, Patel SD, Bolinger L, Kneeland JB, Leigh JS, Reddy R (1998). Sodium multiple quantum spectroscopy of articular cartilage: effects of mechanical compression. *Magn Reson Med* 40:370–375.

- [Duvvuri01] Duvvuri U, Charagundla SR, Kudchodkar SB, Kaufman JH, Kneeland JB, Rizi R, Leigh JS, Reddy R (2001). Human knee: in vivo T1(rho)-weighted MR imaging at 1.5 T—preliminary experience. *Radiology* 220:822–826.
- [Eckstein96] Eckstein F, Gavazzeni A, Sittek H, Haubner M, Lösch A, Milz S, Englmeier KH, Schulte E, Putz R, Reiser M (1996). Determination of knee joint cartilage thickness using three-dimensional magnetic resonance chondro-crassometry (3D MR-CCM). *Magn Reson Med* 36:256–265.
- [Eckstein98a] Eckstein F, Schnier M, Haubner M, Priebsch J, Glaser C, Englmeier KH, Reiser M (1998). Accuracy of cartilage volume and thickness measurements with magnetic resonance imaging. *Clin Orthop Relat Res* :137–148.
- [Eckstein98b] Eckstein F, Tieschky M, Faber SC, Haubner M, Kolem H, Englmeier KH, Reiser MF (1998). Effect of physical exercise on cartilage volume and thickness in vivo: MR imaging study. *Radiology* 207:243–248.
- [Eckstein00] Eckstein F, Lemberger B, Stammberger T, Englmeier KH, Reiser M (2000). Patellar cartilage deformation in vivo after static versus dynamic loading. *J Biomech* 33:819–825.
- [Eckstein02] Eckstein F, Heudorfer L, Faber SC, Burgkart R, Englmeier KH, Reiser M (2002). Long-term and resegmentation precision of quantitative cartilage MR imaging (qMRI). *Osteoarthr Cartil* 10:922–928.
- [Eckstein05] Eckstein F, Charles HC, Buck RJ, Kraus VB, Remmers AE, Hudelmaier M, Wirth W, Evelhoch JL (2005). Accuracy and precision of quantitative assessment of cartilage morphology by magnetic resonance imaging at 3.0T. *Arthritis Rheum* 52:3132–3136.
- [Eckstein06a] Eckstein F, Ateshian G, Burgkart R, Burstein D, Cicuttini F, Dardzinski B, Gray M, Link TM, Majumdar S, Mosher T, Peterfy C, Totterman S, Waterton J, Winalski CS, Felson D (2006). Proposal for a nomenclature for magnetic resonance imaging based measures of articular cartilage in osteoarthritis. *Osteoarthr Cartil* 14:974–983.
- [Eckstein06b] Eckstein F, Burstein D, Link TM (2006). Quantitative mri of cartilage and bone: degenerative changes in osteoarthritis. *NMR Biomed* 19:822–854.
- [Eckstein07] Eckstein F, Mosher TJ, Hunter D (2007). Imaging of knee osteoarthritis: data beyond the beauty. *Curr Opin Rheumatol* 19:435–443.
- [Eckstein08a] Eckstein F, Wirth W, Hudelmaier M, Stein V, Lengfelder V, Cahue S, Marshall M, Prasad P, Sharma L (2008). Patterns of femorotibial cartilage loss in knees with neutral, varus, and valgus alignment. *Arthritis Rheum* 59:1563–1570.
- [Eckstein08b] Eckstein F, Wirth W, Hudelmaier M, Stein V, Lengfelder V, Cahue S, Marshall M, Prasad P, Sharma L (2008). Patterns of femorotibial cartilage loss in knees with neutral, varus, and valgus alignment. *Arthritis Rheum* 59:1563–1570.
- [Eckstein09] Eckstein F, Wyman BT, Buck RJ, Wirth W, Maschek S, Hudelmaier M, Hellio Le Graverand MP (2009). Longitudinal quantitative MR imaging of cartilage morphology in the presence of gadopentetate dimeglumine (Gd-DTPA). *Magn Reson Med* .
- [Erickson91] Erickson SJ, Cox IH, Hyde JS, Carrera GF, Strandt JA, Estkowski LD (1991). Effect of tendon orientation on MR imaging signal intensity: a manifestation of the "magic angle" phenomenon. *Radiology* 181:389–392.
- [Eyre02] Eyre D (2002). Collagen of articular cartilage. *Arthritis Res* 4:30–35.

Bibliography

- [Fernandes02] Fernandes JC, Martel-Pelletier J, Pelletier JP (2002). The role of cytokines in osteoarthritis pathophysiology. *Biorheology* 39:237–246.
- [Filidoro05] Filidoro L, Dietrich O, Weber J, Rauch E, Oerther T, Wick M, Reiser MF, Glaser C (2005). High-resolution diffusion tensor imaging of human patellar cartilage: feasibility and preliminary findings. *Magn Reson Med* 53:993–998.
- [Filidoro08] Filidoro L, Weber DL, Arnoldi AP, Weber J, Raya JG, Jakob PM, Dietrich O, Reiser MF, Putz R, Mützel E, C G (2008). Wien, Austria, pp. B–578.
- [Fitzpatrick98] Fitzpatrick JM, West JB, Maurer CRJ (1998). Predicting error in rigid-body point-based registration. *IEEE Trans Med Imaging* 17:694–702.
- [Fitzpatrick01] Fitzpatrick JM, West JB (2001). The distribution of target registration error in rigid-body point-based registration. *IEEE Trans Med Imaging* 20:917–927.
- [Fletcher00] Fletcher R (2000). Practical methods of optimization. John Wiley and Sons, New York, NY.
- [Fullerton85] Fullerton GD, Cameron IL, Ord VA (1985). Orientation of tendons in the magnetic field and its effect on T2 relaxation times. *Radiology* 155:433–435.
- [Gatehouse04a] Gatehouse PD, He T, Puri BK, Thomas RD, Resnick D, Bydder GM (2004). Contrast-enhanced MRI of the menisci of the knee using ultrashort echo time (UTE) pulse sequences: imaging of the red and white zones. *Br J Radiol* 77:641–647.
- [Gatehouse04b] Gatehouse PD, Thomas RW, Robson MD, Hamilton G, Herlihy AH, Bydder GM (2004). Magnetic resonance imaging of the knee with ultrashort TE pulse sequences. *Magn Reson Imaging* 22:1061–1067.
- [Gillis01] Gillis A, Bashir A, McKeon B, Scheller A, Gray ML, Burstein D (2001). Magnetic resonance imaging of relative glycosaminoglycan distribution in patients with autologous chondrocyte transplants. *Invest Radiol* 36:743–748.
- [Glaser02] Glaser C, Putz R (2002). Functional anatomy of articular cartilage under compressive loading: Quantitative aspects of global, local and zonal reactions of the collagenous network with respect to the surface integrity. *Osteoarthritis Cartilage* 10:83–99.
- [Glaser03] Glaser C, Burgkart R, Kutschera A, Englmeier KH, Reiser M, Eckstein F (2003). Femoro-tibial cartilage metrics from coronal MR image data: Technique, test-retest reproducibility, and findings in osteoarthritis. *Magn Reson Med* 50:1229–1236.
- [Glaser05] Glaser C (2005). New techniques for cartilage imaging: T₂ relaxation time and diffusion-weighted MR imaging. *Radiol Clin North Am* 43:641–653.
- [Glaser06] Glaser C, Mendlik T, Dinges J, Weber J, Stahl R, Trumm C, Reiser MF (2006). Global and regional reproducibility of T₂ relaxation time measurements in human patellar cartilage. *Magn Reson Med* 56:527–534.
- [Glaser07] Glaser C, Horng A, Mendlik T, Weckbach S, Hoffmann RT, Wagner S, Raya JG, Horger W, Reiser MF (2007). Global and regional reproducibility of T₂ relaxation time measurements in human patellar cartilage. *Röfo* 179:146–152.
- [Goldring06] Goldring MB, Tsuchimochi K, Ijiri K (2006). The control of chondrogenesis. *J Cell Biochem* 97:33–44.
- [Goldring07] Goldring MB, Goldring SR (2007). Osteoarthritis. *J Cell Physiol* 213:626–634.
- [Goldring08] Goldring MB, Otero M, Tsuchimochi K, Ijiri K, Li Y (2008). Defining the roles of inflammatory and anabolic cytokines in cartilage metabolism. *Ann Rheum Dis* 67 Suppl 3:75–82.

- [Goodwin98] Goodwin DW, Dunn JF (1998). High-resolution magnetic resonance imaging of articular cartilage: correlation with histology and pathology. *Top Magn Reson Imaging* 9:337–347.
- [Goodwin00] Goodwin DW, H Z, Dunn JF (2000). In vitro MR imaging of hyaline cartilage: correlation with scanning electron microscopy. *AJR Am J Roentgenol* 174:405–409.
- [Graham96] Graham SJ, Stanchev PL, Bronskill MJ (1996). Criteria for analysis of multicomponent tissue T₂ relaxation data. *Magn Reson Med* 35:370–378.
- [Gray08] Gray ML, Burstein D, Kim YJ, Maroudas A (2008). 2007 Elizabeth Winston Lanier Award Winner. Magnetic resonance imaging of cartilage glycosaminoglycan: basic principles, imaging technique, and clinical applications. *J Orthop Res* 26:281–291.
- [Gudbjartsson95] Gudbjartsson H, Patz S (1995). The rician distribution of noisy MRI data. *Magn Reson Med* 34:910–914.
- [Guilak95] Guilak F (1995). Compression-induced changes in the shape and volume of the chondrocyte nucleus. *J Biomech* 28:1529–1541.
- [Gyls-Morin87] Gyls-Morin VM, Hajek PC, Sartoris DJ, Resnick D (1987). Articular cartilage defects: detectability in cadaver knees with MR. *AJR Am J Roentgenol* 148:1153–1157.
- [Hancock08] Hancock CM, Riegger-Krug C (2008). Modulation of pain in osteoarthritis: the role of nitric oxide. *Clin J Pain* 24:353–365.
- [Hannila07] Hannila I, Nieminen MT, Rauvala E, Tervonen O, Ojala R (2007). Patellar cartilage lesions: comparison of magnetic resonance imaging and T2 relaxation-time mapping. *Acta Radiol* 48:444–448.
- [Henkelman85] Henkelman RM (1985). Measurement of signal intensities in the presence of noise in MR images. *Med Phys* 12:232–237.
- [Henkelman94] Henkelman RM, Stanisz GJ, Kim JK, Bronskill MJ (1994). Anisotropy of NMR properties of tissues. *Magn Reson Med* 32:592–601.
- [Hill01] Hill DL, Batchelor PG, Holden M, Hawkes DJ (2001). Medical image registration. *Phys Med Biol* 46:R1–R45.
- [Hinman07] Hinman RS, Crossley KM (2007). Patellofemoral joint osteoarthritis: an important subgroup of knee osteoarthritis. *Rheumatology (Oxford)* 46:1057–1062.
- [Hohe02] Hohe J, Faber S, Muehlbauer R, Reiser MF, Englmeier KH, Eckstein F (2002). Three-dimensional analysis and visualization of regional mr signal intensity distribution of articular cartilage. *Med Eng Phys* 24:219–227.
- [Holden86] Holden JE, Halama JR, Hasegawa BH (1986). The propagation of stochastic pixel noise magnitude and phase values in the fourier analysis of digital images. *Phys Med Biol* 31:383–396.
- [Horton06] Horton WE, Bennion P, Yang L (2006). Cellular, molecular, and matrix changes in cartilage during aging and osteoarthritis. *J Musculoskelet Neuronal Interact* 6:379–381.
- [Hoshino87] Hoshino A, Wallace WA (1987). Impact-absorbing properties of the human knee. *J Bone Joint Surg Br* 69:807–811.
- [Huber00] Huber M, Trattig S, Lintner F (2000). Anatomy, biochemistry, and physiology of articular cartilage. *Invest Radiology* 35:573–580.
- [Hunter43] Hunter W (1743). On the structure and diseases of articulating cartilage. *Phil Trans Royal Soc London* 42:514–580.

Bibliography

- [Hunter03] Hunter DJ, March L, Sambrook PN (2003). The association of cartilage volume with knee pain. *Osteoarthr Cartil* 11:725–729.
- [Imhof00] Imhof H, Sulzbacher I, Grampp S, Czerny C, Youssefzadeh S, Kainberger F (2000). Subchondral bone and cartilage disease: a rediscovered functional unit. *Invest Radiol* 35:581–588.
- [Inglis07] Inglis D, Pui M, Ioannidis G, Beattie K, Boulos P, Adachi JD, Webber CE, Eckstein F (2007). Accuracy and test-retest precision of quantitative cartilage morphology on a 1.0 T peripheral magnetic resonance imaging system. *Osteoarthr Cartil* 15:110–115.
- [Insko97] Insko EK, Reddy R, Leigh JS (1997). High resolution, short echo time sodium imaging of articular cartilage. *J Magn Reson Imaging* 7:1056–1059.
- [Insko99] Insko EK, Kaufman JH, Leigh JS, Reddy R (1999). Sodium NMR evaluation of articular cartilage degradation. *Magn Reson Med* 41:30–34.
- [Irrgang01] Irrgang JJ, Anderson AF, Boland AL, Harner CD, Kurosaka M, Neyret P, Richmond JC, Shelborne KD (2001). Development and validation of the international knee documentation committee subjective knee form. *Am J Sports Med* 29:600–613.
- [Johnston00] Johnston PR, Gulrajani RM (2000). Selecting the corner in the L-curve approach to Tikhonov regularization. *IEEE Trans Biomed Eng* 47:1293–1296.
- [Jones96] Jones JA, Hodgkinson P, Barker AL, Hore PJ (1996). Optimal sampling strategies for measurement of spin-spin relaxation times. *J Magn Reson* B113:25–34.
- [Jordan03] Jordan KM, Arden NK, Doherty M, Bannwarth B, Bijlsma JW, Dieppe P, Gunther K, Hauselmann H, Herrero-Beaumont G, Kaklamanis P, Lohmander S, Leeb B, Lequesne M, Mazieres B, Martin-Mola E, Pavelka K, Pendleton A, Punzi L, Serni U, Swoboda B, Verbruggen G, Zimmerman-Gorska I, Dougados M (2003). EULAR Recommendations 2003: an evidence based approach to the management of knee osteoarthritis: Report of a Task Force of the Standing Committee for International Clinical Studies Including Therapeutic Trials (ESCISIT). *Ann Rheum Dis* 62:1145–1155.
- [Kadler08] Kadler KE, Hill A, Canty-LairdKaedler EG (2008). Collagen fibrillogenesis: fibronectin, integrins, and minor collagens as organizers and nucleators. *Curr Opin Cell Biol* 20:495–501.
- [Keene95] Keene DR, Oxford JT, Morris NP (1995). Ultrastructural localization of collagen types II, IX, and XI in the growth plate of human rib and fetal bovine epiphyseal cartilage: type XI collagen is restricted to thin fibrils. *J Histochem Cytochem* 43:967–979.
- [Kellgren57] Kellgren JH, Lawrence JS (1957). Radiological assessment of osteo-arthrosis. *Ann Rheum Dis* 16:494–502.
- [Kiani02] Kiani C, Chen L, Wu YJ, Yee AJ, Yang BB (2002). Structure and function of aggrecan. *Cell Res* 12:19–32.
- [King04] King KB, Lindsey CT, Dunn TC, Ries MD, Steinbach LS, Majumdar S (2004). A study of the relationship between molecular biomarkers of joint degeneration and the magnetic resonance-measured characteristics of cartilage in 16 symptomatic knees. *Magn Reson Imaging* 22:1117–1123.
- [Knudson01] Knudson CB, Knudson W (2001). Cartilage proteoglycans. *Semin Cell Dev Biol* 12:69–78.
- [Koay06] Koay CG, Basser PJ (2006). Analytically exact correction scheme for signal extraction from noisy magnitude MR signals. *J Magn Reson* 179:317–322.

- [Koch-Institut06] Koch-Institut R (2006). *Gesundheit in Deutschland. Gesundheitsberichterstattung des Bundes*. Robert Koch-Institut, Berlin, Germany.
- [Koff07] Koff MF, Amrami KK, Kaufman KR (2007). Clinical evaluation of T2 values of patellar cartilage in patients with osteoarthritis. *Osteoarthr Cartil* 15:198–204.
- [Koff08] Koff MF, Amrami KK, Felmlee JP, Kaufman KR (2008). Bias of cartilage T2 values related to method of calculation. *Magn Reson Imaging* 26:1236–1243.
- [Koff09] Koff MF, Parratte S, Amrami KK, Kaufman KR (2009). Examiner repeatability of patellar cartilage T(2) values. *Magn Reson Imaging* 27:131–136.
- [Koo05] Koo S, Gold GE, Andriacchi TP (2005). Considerations in measuring cartilage thickness using MRI: factors influencing reproducibility and accuracy. *Osteoarthr Cartil* 13:782–789.
- [Krasnokutsky07] Krasnokutsky S, Samuels J, Abramson SB (2007). Osteoarthritis in 2007. *Bull NYU Hosp Jt Dis* 65:222–228.
- [Kurkijärvi07] Kurkijärvi JE, Mattila L, Ojala RO, Vasara AI, Jurvelin JS, Kiviranta I, Nieminen MT (2007). Evaluation of cartilage repair in the distal femur after autologous chondrocyte transplantation using T2 relaxation time and dGEMRIC. *Osteoarthr Cartil* 15:372–378.
- [Kurkijärvi08] Kurkijärvi JE, Nissi MJ, Rieppo J, Töyräs J, Kiviranta I, Nieminen MT, Jurvelin JS (2008). The zonal architecture of human articular cartilage described by T2 relaxation time in the presence of Gd-DTPA²⁻. *Magn Reson Imaging* 26:602–607.
- [Laws04] Laws A (2004). *Principles of nuclear magnetism*. Oxford University Press, New York, NY.
- [Lazebnik03] Lazebnik RS, Lancaster TL, S BM, S LJ, L WD (2003). Volume registration using needle paths and point landmarks for evaluation of interventional MRI treatments. *IEEE Trans Med Imaging* 22:653–660.
- [Le Bihan86] Le Bihan D, Breton E, Lallemand D, Grenier P, Cabanis E, Laval-Jeantet M (1986). MR imaging of intravoxel incoherent motions: application to diffusion and perfusion in neurologic disorders. *Radiology* 161:401–407.
- [Le Bihan01] Le Bihan D, Mangin JF, Poupon C, Clark CA, Pappata S, Molko N, Chabriat H (2001). Diffusion tensor imaging: concepts and applications. *J Magn Reson Imaging* 13:534–546.
- [Lehner89] Lehner KB, Rechl HP, Gmeinwieser JK, Heuck AF, Lukas HP, Kohl HP (1989). Structure, function, and degeneration of bovine hyaline cartilage: assessment with MR imaging in vitro. *Radiology* 170:495–499.
- [Levenberg44] Levenberg K (1944). A method for the solution of certain problems in Least Squares. *Quart Appl Math* 2:164–168.
- [Levene60] Levene H (1960). *Contributions to probability and statistics: Essays in honor of Harold Hotelling*. Stanford University Press, Stanford, CA, pp. 288–292.
- [Liess02] Liess C, Lüsse S, Karger N, Heller M, Glüer CC (2002). Detection of changes in cartilage water content using MRI T₂-mapping in vivo. *Osteoarthritis Cartilage* 10:907–913.
- [Ling08] Ling W, Regatte RR, Navon G, Jerschow A (2008). Assessment of glycosaminoglycan concentration in vivo by chemical exchange-dependent saturation transfer (gagCEST). *Proc Natl Acad Sci USA* 105:2266–2270.
- [Lotz95] Lotz M, Blanco FJ, von Kempis J (1995). Cytokine regulation of chondrocyte functions. *J Rheumatol* 43 (suppl):104–108.

Bibliography

- [Lüsse95] Lüsse S, Knauss R, Werner A, Gründer W, Arnold K (1995). Action of compression and cations on the proton and deuterium relaxation in cartilage. *Magn Reson Med* 33:483–489.
- [MacFall86] MacFall JR, Riederer SJ, Wang HZ (1986). An analysis of noise propagation in computed T₂, pseudodensity, and synthetic spin-echo images. *Med Phys* 13:285–292.
- [Maroudas68] Maroudas A (1968). Physicochemical properties of cartilage in the light of ion exchange theory. *Biophys J* 8:575–595.
- [Maroudas69] Maroudas A, Muir H, Wingham J (1969). The correlation of fixed negative charge with glycosaminoglycan content of human articular cartilage. *Biochim Biophys Acta* 177:492–500.
- [Maroudas76] Maroudas A (1976). Balance between swelling pressure and collagen tension in normal and degenerate cartilage. *Nature* 260:808–809.
- [Maroudas77] Maroudas A, Venn M (1977). Chemical composition and swelling of normal and osteoarthrotic femoral head cartilage. II. Swelling. *Ann Rheum Dis* 36:399–406.
- [Maroudas80] Maroudas A, Bayliss MT, Venn MF (1980). Further studies on the composition of human femoral head cartilage 260:808–809.
- [Maroudas85] Maroudas A, Ziv I, Weisman N, Venn M (1985). Studies of hydration and swelling pressure in normal and osteoarthrotic cartilage. *Biorheology* 22:159–169.
- [Maroudas98] Maroudas A, Bayliss MT, Uchitel-Kaushanskya N, Schneidermana R, Gilav E (1998). Ag-grecan turnover in human articular cartilage: Use of aspartic acid racemization as a marker of molecular age. *Arch Biochem Biophys* 350:61–71.
- [Marquardt63] Marquardt D (1963). An algorithm for Least Squares estimation of nonlinear parameters. *SIAM J Appl Math* 11:431–441.
- [Mattiello97] Mattiello J, Basser PJ, Le Bihan D (1997). The b matrix in diffusion tensor echo-planar imaging. *Magn Reson Med* 37:292–300.
- [Maurer97] Maurer CRJ, Fitzpatrick JM, Wang MY, Jr GRL, J MR, S AG (1997). Registration of head volume images using implantable fiducial markers. *IEEE Trans Med Imaging* 16:447–462.
- [Meder06] Meder R, de Visser SK, Bowden JC, Bostrom T, Pope JM (2006). Diffusion tensor imaging of articular cartilage as a measure of tissue microstructure. *Osteoarthr Cartil* 14:875–881.
- [Mendlik04] Mendlik T, Faber SC, Weber J, Hohe J, Rauch E, Reiser M, Glaser C (2004). T₂ quantitation of human articular cartilage in a clinical setting at 1.5 T: implementation and testing of four multiecho pulse sequence designs for validity. *Invest Radiol* 39:288–299.
- [Miller93] Miller AJ, Joseph PM (1993). The use of power images to perform quantitative analysis on low SNR MR images. *Magn Reson Imaging* 11:1051–1056.
- [Mintorovitch91] Mintorovitch J, Moseley ME, Chileuitt L, Shimizu H, Cohen Y, Weinstein PR (1991). Comparison of diffusion- and T₂-weighted MRI for the early detection of cerebral ischemia and reperfusion in rats. *Magn Reson Med* 18:39–50.
- [Mlynárik99] Mlynárik V, Trattnig S, Huber M, Zemsch A, Imhof H (1999). The role of relaxation times in monitoring proteoglycan depletion in articular cartilage. *J Magn Reson Imaging* 10:497–502.
- [Mlynárik04] Mlynárik V, Szomolányi P, To R (2004). Transverse relaxation mechanisms in articular cartilage. *J Magn Reson* 169:300–307.

- [Modl91] Modl JM, Sether LA, Haughton VM, Kneeland JB (1991). Articular cartilage: correlation of histologic zones with signal intensity at MR imaging. *Radiology* 181:853–855.
- [Mollenhauer84] Mollenhauer J, Bee JA, Lizarbe MA, von der Mark K (1984). Role of anchorin CII, a 31,000-mol-wt membrane protein, in the interaction of chondrocytes with type II collagen. *J Cell Biol* 98:1572–1579.
- [Morales07] Morales TI (2007). Chondrocyte moves: clever strategies? *Osteoarthr Cartil* 15:861–871.
- [Mosher00] Mosher TJ, Dardzinski BJ, Smith H (2000). Human articular cartilage: influence of aging and early symptomatic degeneration on the spatial variation of T₂—preliminary findings at 3 T. *Radiology* 214:259–266.
- [Mosher01] Mosher TJ, Smith H, Dardzinski BJ, Schmithorst VJ, Smith MB (2001). MR imaging and T₂ mapping of femoral cartilage: in vivo determination of the magic angle effect. *AJR Am J Roentgenol* 177:665–669.
- [Mosher04a] Mosher TJ, Dardzinski BJ (2004). Cartilage MRI T₂ relaxation time mapping: overview and applications. *Semin Musculoskelet Radiol* 8:355–368.
- [Mosher04b] Mosher TJ, Liu Y, Yang QX, Yao J, Smith R, Dardzinski BJ, Smith MB (2004). Age dependency of cartilage magnetic resonance imaging T₂ relaxation times in asymptomatic women. *Arthritis Rheum* 50:2820–2828.
- [Muir70] Muir H, Bullough P, Maroudas A (1970). The distribution of collagen in human articular cartilage with some of its physiological implications. *J Bone Joint Surg Br* 52:554–563.
- [Multanen08] Multanen J, Rauvala E, Lammentausta E, Ojala R, Kiviranta I, Häkkinen A, Nieminen MT, Heinonen A (2008). Reproducibility of imaging human knee cartilage by delayed gadolinium-enhanced MRI of cartilage (dGEMRIC) at 1.5 Tesla. *Osteoarthr Cartil* .
- [Myers92] Myers SL, Flusser D, Brandt KD, Heck DA (1992). Prevalence of cartilage shards in synovium and their association with synovitis in patients with early and endstage osteoarthritis. *J Rheumatol* 19:1247–1251.
- [Nieminen01] Nieminen MT, Rieppo J, Töyräs J, Hakumäki JM, Silvennoinen J, Hyttinen MM, Helminen HJ, Jurvelin JS (2001). T₂ relaxation reveals spatial collagen architecture in articular cartilage: a comparative quantitative mri and polarized light microscopic study. *Magn Reson Med* 46:487–493.
- [Nieminen04] Nieminen MT, Menezes NM, Williams A, Burstein D (2004). T₂ of articular cartilage in the presence of Gd-DTPA²⁻. *Magn Reson Med* 51:1147–1152.
- [Oliveria95] Oliveria SA, Felson DT, Reed JI, Cirillo PA, Walker AM (1995). Incidence of symptomatic hand, hip, and knee osteoarthritis among patients in a health maintenance organization. *Arthritis Rheum* 38:1134–1141.
- [Oliveria96] Oliveria SA, Felson DT, Klein RA, Reed JI, Walker AM (1996). Estrogen replacement therapy and the development of osteoarthritis. *Epidemiology* 7:415–419.
- [Olver72] Olver FWJ (1972). *Handbook of mathematical functions*. Dover Publications Inc, New York, NY.
- [Parkkinen96] Parkkinen JJ, Häkkinen TP, Savolainen S, Wang C, Tammi R, Agren UM, Lammi MJ, Arokoski J, Helminen HJ, Tammi MI (1996). Distribution of hyaluronan in articular cartilage as probed by a biotinylated binding region of aggrecan. *Histochem Cell Biol* 105:187–194.

Bibliography

- [Paul93] Paul PK, Jasani MK, Sebok D, Rakhit A, Dunton AW, Douglas FL (1993). Variation in MR signal intensity across normal human knee cartilage. *J Magn Reson Imaging* 3:569–574.
- [Polyanin08] Polyanin AD, Manzhiro AV (2008). *Handbook of Integral Equations*. Chapman & Hall/CRC Press, Boca Ratón, FL.
- [Poole97] Poole CA (1997). Articular cartilage chondrons: Form,function and failure: A review. *J Anat* 1991:1–13.
- [Poon92] Poon CS, Henkelman RM (1992). Practical T2 quantitation for clinical applications. *J Magn Reson Imaging* 2:541–553.
- [Quinn05] Quinn TM, Hunziker EB, Häuselmann HJ (2005). Variation of cell and matrix morphologies in articular cartilage among locations in the adult human knee. *Osteoarthr Cartil* 13:672–678.
- [Ratcliffe84] Ratcliffe A, Fryer PR, Hardingham TE (1984). The distribution of aggregating proteoglycans in the articular cartilage: Comparisson of quantitative immunoelectron microscopy with radioimmunoassay and biochemical analysis. *J Histochem Cytochem* 32:193–201.
- [Raya05] Raya JG, Dietrich O, Reiser MF, Baur-Melnyk A (2005). Techniques for diffusion-weighted imaging of bone marrow. *Eur J Radiol* 55:64–73.
- [Raya06] Raya JG, Dietrich O, Reiser MF, Baur-Melnyk A (2006). Methods and applications of diffusion imaging of vertebral bone marrow. *J Magn Reson Imaging* 24:1207–1220.
- [Raya07] Raya JG, Dietrich O, Birkenmaier C, Sommer J, Reiser MF, Baur-Melnyk A (2007). Feasibility of a RARE-based sequence for quantitative diffusion-weighted MRI of the spine. *Eur Radiol* 17:2872–2879.
- [Raya08a] Raya JG, Melkus G, Dietrich O, Filidoro L, Weber D, Reiser MF, Jakob PM, Glaser C (2008). Multiparametric characterization of healthy and diseased cartilage at 17.6-T: Early results. Toronto, Canada, p. 330.
- [Raya08b] Raya JG, Melkus G, Dietrich O, Mützel E, Gruber E, Reiser MF, Jakob PM, Glaser C (2008). Cartilage imaging multiparametric characterization of healthy and diseased articular cartilage at 17.6-T. In 94th congress of the Radiologic Society of North America. Valencia, Spain, p. 242.
- [Raya08c] Raya JG, Melkus G, Dietrich O, Mützel E, Reiser MF, Jakob PM, Glaser C (2008). chapter Multiparametric characterization of healthy and diseased cartilage under loading conditions at 17.6-T. European Society of Magnetic Resonance in the Medicin and Biology, Valencia, Spain, p. 242.
- [Raya09] Raya JG, Horng A, Dietrich O, Weber J, Dinges J, Mützel E, Reiser MF, Glaser C (2009). Voxel-based reproducibility of T2 relaxation time in patellar cartilage at 1.5 T with a new validated 3D rigid registration algorithm. *Magn Reson Mater Phys* 22:229–239.
- [Raynauld08] Raynauld JP, Martel-Pelletier J, Abram F, Dorais M, Haraoui B, Choquette D, Bias P, Emmermert KH, Laufer S, Pelletier JP (2008). Analysis of the precision and sensitivity to change of different approaches to assess cartilage loss by quantitative MRI in a longitudinal multi-centre clinical trial in patients with knee osteoarthritis. *Arthritis Res Ther* 10:R129.
- [Reddy95] Reddy R, Insko EK, Kaufmann JH, Bolinger L, Kneeland JB, Leigh JS (1995). Mr of the cartilage under spin-locking. In Proc 2nd annual meeting of the International Society of Magnetic Resonance in the Medicine. Nice, France, p. 1535.

- [Reddy97] Reddy R, Li S, Noyszewski EA, Kneeland JB, Leigh JS (1997). In vivo sodium multiple quantum spectroscopy of human articular cartilage. *Magn Reson Med* 38:207–214.
- [Reddy98] Reddy R, Insko EK, Noyszewski EA, Dandora R, Kneeland JB, Leigh JS (1998). Sodium MRI of human articular cartilage in vivo. *Magn Reson Med* 39:697–701.
- [Redfield55] Redfield AG (1955). Nuclear magnetic resonance saturation and rotary saturation in solids. *Phys Rev* 98:1787–1809.
- [Regatte02] Regatte RR, Akella SV, Borthakur A, Kneeland JB, Reddy R (2002). Proteoglycan depletion-induced changes in transverse relaxation maps of cartilage: comparison of T2 and T1rho. *Acad Radiol* 9:1388–1394.
- [Regatte03a] Regatte RR, Akella SV, Borthakur A, Kneeland JB, Reddy R (2003). In vivo proton MR three-dimensional T1rho mapping of human articular cartilage: initial experience. *Radiology* 229:269–274.
- [Regatte03b] Regatte RR, Akella SV, Wheaton AJ, Borthakur A, Kneeland JB, Reddy R (2003). T1rho-relaxation mapping of human femoral-tibial cartilage in vivo. *J Magn Reson Imaging* 18:336–341.
- [Regatte04] Regatte RR, Akella SV, Wheaton AJ, Lech G, Borthakur A, Kneeland JB, Reddy R (2004). 3D-T1rho-relaxation mapping of articular cartilage: in vivo assessment of early degenerative changes in symptomatic osteoarthritic subjects. *Acad Radiol* 11:741–749.
- [Regatte06] Regatte RR, Akella SV, Lonner JH, Kneeland JB, Reddy R (2006). T1rho relaxation mapping in human osteoarthritis (OA) cartilage: comparison of T1rho with T2. *J Magn Reson Imaging* 23:547–553.
- [Reicher85] Reicher MA, Rauschnig W, Gold RH, Bassett LW, Lufkin RB, Glen W (1985). High-resolution magnetic resonance imaging of the knee joint: normal anatomy. *AJR Am J Roentgenol* 145:895–902.
- [Rice54] Rice SO (1954). Selected papers on noise and stochastic processes. Dover Publications Inc, New York, NY.
- [Robson03] Robson MD, Gatehouse PD, Bydder M, Bydder GM (2003). Magnetic resonance: an introduction to ultrashort TE (UTE) imaging. *J Comput Assist Tomogr* 27:825–846.
- [Robson06] Robson MD, Bydder GM (2006). Clinical ultrashort echo time imaging of bone and other connective tissues. *NMR Biomed* 19:765–780.
- [Roos05] Roos EM, Dahlberg L (2005). Positive effects of moderate exercise on glycosaminoglycan content in knee cartilage: a four-month, randomized, controlled trial in patients at risk of osteoarthritis. *Arthritis Rheum* 52:3507–3514.
- [Rubenstein93] Rubenstein JD, Kim JK, Morova-Protzner I, Stanchev PL, Henkelman RM (1993). Effects of collagen orientation on MR imaging characteristics of bovine articular cartilage. *Radiology* 188:219–226.
- [Saase89] van Saase JL, van Romunde LK, Cats A, Vandenbroucke JP, Valkenburg HA (1989). Epidemiology of osteoarthritis: Zoetermeer survey. Comparison of radiological osteoarthritis in a Dutch population with that in 10 other populations. *Ann Rheum Dis* 48:271–280.
- [Schick97] Schick F (1997). SPLICE: sub-second diffusion-sensitive MR imaging using a modified fast spin-echo acquisition mode. *Magn Reson Med* 38:638–644.

Bibliography

- [Schneider08] Schneider E, NessAiver M, White D, Purdy D, Martin L, Fanella L, Davis D, Vignone M, Wu G, Gullapalli R (2008). The osteoarthritis initiative (OAI) magnetic resonance imaging quality assurance methods and results. *Osteoarthr Cartil* 16:994–1004.
- [Shapiro00] Shapiro EM, Borthakur A, Dandora R, Kriss A, Leigh JS, Reddy R (2000). Sodium visibility and quantitation in intact bovine articular cartilage using high field (23)Na MRI and MRS. *J Magn Reson* 142:24–31.
- [Shinar06] Shinar H, Navon G (2006). Multinuclear NMR and microscopic MRI studies of the articular cartilage nanostructure. *NMR Biomed* 19:877–893.
- [Shrager98] Shrager RI, Weiss GH, Spencer RG (1998). Optimal time spacings for T₂ measurements: monoexponential and biexponential systems. *NMR Biomed* 11:297–305.
- [Slater72] Slater LY (1972). *Handbook of mathematical functions*. Dover Publications Inc., New York, NY.
- [Slowman86] Slowman SD, Brandt KD (1986). Composition and glycosaminoglycan metabolism of articular cartilage from habitually loaded and habitually unloaded sites. *Arthritis Rheum* 29:88–94.
- [Smith01] Smith HE, Mosher TJ, Dardzinski BJ, Collins BG, Collins CM, Yang QX, Schmithorst VJ, Smith MB (2001). Spatial variation in cartilage T₂ of the knee. *J Magn Reson Imaging* 14:50–55.
- [Stahl07] Stahl R, Blumenkrantz G, Carballido-Gamio J, Zhao S, Munoz T, Hellio Le Graverand-Gastineau MP, Li X, Majumdar S, Link TM (2007). MRI-derived T₂ relaxation times and cartilage morphometry of the tibio-femoral joint in subjects with and without osteoarthritis during a 1-year follow-up. *Osteoarthr Cartil* 15:1225–1234.
- [Stammberger99] Stammberger T, Eckstein F, Englmeier KH, Reiser M (1999). Determination of 3D cartilage thickness data from MR imaging: computational method and reproducibility in the living. *Magn Reson Med* 41:529–536.
- [Stammberger00] Stammberger T, Hohe J, Englmeier KH, Reiser M, Eckstein F (2000). Elastic registration of 3D cartilage surfaces from MR image data for detecting local changes in cartilage thickness. *Magn Reson Med* 44:592–601.
- [Stejskal65] Stejskal EO, Tanner JE (1965). Spin diffusion measurements: Spin echoes in the presence of time-dependent field gradient. *J Chem Phys* 42:288–292.
- [Stockwell67] Stockwell RA, Scott JE (1967). Distribution of acid glycosaminoglycans in human articular cartilage. *Nature* 215:1376–1378.
- [Tallheden06] Tallheden T, Brittberg M, Peterson L, Lindahl A (2006). Human articular chondrocytes—plasticity and differentiation potential. *Cells Tissues Organs* (Print) 184:55–67.
- [Trattnig07a] Trattnig S, Mamisch TC, Welsch GH, Glaser C, Szomolanvi P, Gebetsroither S, Stastny O, Horger W, Millington S, Marlovits S (2007). Quantitative T₂ mapping of matrix-associated autologous chondrocyte transplantation at 3 tesla: an in vivo cross-sectional study. *Invest Radiol* 42:442–448.
- [Trattnig07b] Trattnig S, Marlovits S, Gebetsroither S, Szomolanyi P, Welsch GH, Salomonowitz E, Watanabe A, Deimling M, Mamisch TC (2007). Three-dimensional delayed gadolinium-enhanced MRI of cartilage (dGEMRIC) for in vivo evaluation of reparative cartilage after matrix-associated autologous chondrocyte transplantation at 3.0T: Preliminary results. *J Magn Reson Imaging* 26:974–982.

- [Tyrrell88] Tyrrell RL, Gluckert K, Pathria M, Modic MT (1988). Fast three-dimensional MR imaging of the knee: comparison with arthroscopy. *Radiology* 166:865–872.
- [Uhl98] Uhl M, Ihling C, Allmann KH, Laubenberger J, Tauer U, Adler CP, Langer M (1998). Human articular cartilage: in vitro correlation of MRI and histologic findings. *Eur Radiol* 8:1123–1129.
- [Vasara05] Vasara AI, Nieminen MT, Jurvelin JS, Peterson L, Lindahl A, Kiviranta I (2005). Indentation stiffness of repair tissue after autologous chondrocyte transplantation. *Clin Orthop Relat Res* :233–242.
- [Venn77] Venn MF, Maroudas A (1977). Chemical composition and swelling of normal and osteoarthrotic femoral head cartilage. I. Chemical composition. *Ann Rheum Dis* 36:121–129.
- [Venn78] Venn MF (1978). Variation of chemical composition with age in human femoral head cartilage. *Ann Rheum Dis* 37:168–174.
- [Verzijl00] Verzijl N, DeGroot J, Thorpe SR, Bank RA, Shaw JN, Lyons TJ, Bijlsma JW, Lafeber FP, Baynes JW, TeKoppele JM (2000). Effect of collagen turnover on the accumulation of advanced glycation end products. *J Biol Chem* 275:39027–39031.
- [Visser08a] de Visser SK, Bowden JC, Wentrup-Byrne E, Rintoul L, Bostrom T, Pope JM, Momot KI (2008). Anisotropy of collagen fibre alignment in bovine cartilage: comparison of polarised light microscopy and spatially resolved diffusion-tensor measurements. *Osteoarthr Cartil* 16:689–697.
- [Visser08b] de Visser SK, Crawford RW, Pope JM (2008). Structural adaptations in compressed articular cartilage measured by diffusion tensor imaging. *Osteoarthr Cartil* 16:83–89.
- [Weiss68] Weiss C, Rosenberg L, Helfet AJ (1968). An ultrastructural study of normal young adult human articular cartilage. *J Bone Joint Surg* 50:663–674.
- [Welsch08a] Welsch GH, Mamisch TC, Domayer SE, Dorotka R, Kutscha-Lissberg F, Marlovits S, White LM, Trattnig S (2008). Cartilage T2 assessment at 3-T MR imaging: in vivo differentiation of normal hyaline cartilage from reparative tissue after two cartilage repair procedures—initial experience. *Radiology* 247:154–161.
- [Welsch08b] Welsch GH, Mamisch TC, Hughes T, Zilkens C, Quirbach S, Scheffer K, Kraff O, Schweitzer ME, Szomolanyi P, Trattnig S (2008). In vivo biochemical 7.0 Tesla magnetic resonance: preliminary results of dGEMRIC, zonal T2, and T2* mapping of articular cartilage. *Invest Radiol* 43:619–626.
- [Welsch08c] Welsch GH, Mamisch TC, Weber M, Horger W, Bohndorf K, Trattnig S (2008). High-resolution morphological and biochemical imaging of articular cartilage of the ankle joint at 3.0 T using a new dedicated phased array coil: in vivo reproducibility study. *Skeletal Radiol* 37:519–526.
- [Welsch09] Welsch GH, Mamisch TC, Marlovits S, Glaser C, Friedrich K, Hennig FF, Salomonowitz E, Trattnig S (2009). Quantitative T2 mapping during follow-up after matrix-associated autologous chondrocyte transplantation (MACT): Full-thickness and zonal evaluation to visualize the maturation of cartilage repair tissue. *J Orthop Res* .
- [West01] West JB, Fitzpatrick JM, Toms SA, Maurer CRJ, Maciunas RJ (2001). Fiducial point placement and the accuracy of point-based, rigid body registration. *Neurosurgery* 48:810–816.
- [Wheaton04a] Wheaton AJ, Borthakur A, Dodge GR, Kneeland JB, Schumacher HR, Reddy R (2004). Sodium magnetic resonance imaging of proteoglycan depletion in an in vivo model of osteoarthritis. *Acad Radiol* 11:21–28.

Bibliography

- [Wheaton04b] Wheaton AJ, Casey FL, Gougoutas AJ, Dodge GR, Borthakur A, Lonner JH, Schumacher HR, Reddy R (2004). Correlation of T1rho with fixed charge density in cartilage. *J Magn Reson Imaging* 20:519–525.
- [Wheaton05] Wheaton AJ, Dodge GR, Elliott DM, Nicoll SB, Reddy R (2005). Quantification of cartilage biomechanical and biochemical properties via T1rho magnetic resonance imaging. *Magn Reson Med* 54:1087–1093.
- [Whittall99] Whittall KP, MacKay AL, Li DK (1999). Are mono-exponential fits to a few echoes sufficient to determine T₂ relaxation for in vivo human brain? *Magn Reson Med* 41:1255–1257.
- [Wight92] Wight TN, Kinsella MG, Qwarnstrom EE (1992). The role of proteoglycans in cell adhesion, migration and proliferation. *Curr Opin Cell Biol* 4:793–801.
- [Williams03] Williams A, Oppenheimer RA, Gray ML, Burstein D (2003). Differential recovery of glycosaminoglycan after IL-1-induced degradation of bovine articular cartilage depends on degree of degradation. *Arthritis Res Ther* 5:97–105.
- [Williams05] Williams A, Sharma L, McKenzie CA, Prasad PV, Burstein D (2005). Delayed gadolinium-enhanced magnetic resonance imaging of cartilage in knee osteoarthritis: findings at different radiographic stages of disease and relationship to malalignment. *Arthritis Rheum* 52:3528–3535.
- [Wilson90] Wilson MG, Michet CJ, Ilstrup DM, Melton LJ (1990). Idiopathic symptomatic osteoarthritis of the hip and knee: a population-based incidence study. *Mayo Clin Proc* 65:1214–1221.
- [Wirth08] Wirth W, Eckstein F (2008). A technique for regional analysis of femorotibial cartilage thickness based on quantitative magnetic resonance imaging. *IEEE Trans Med Imaging* 27:737–744.
- [Wluka02] Wluka AE, Stuckey S, Snaddon J, Cicuttini FM (2002). The determinants of change in tibial cartilage volume in osteoarthritic knees. *Arthritis Rheum* 46:2065–2072.
- [Woods98a] Woods RP, Grafton ST, Holmes CJ, Cherry SR, Mazziotta JC (1998). Automated image registration: I. general methods and intrasubject, intramodality validation. *J Comput Assist Tomogr* 22:139–152.
- [Woods98b] Woods RP, Grafton ST, Watson JD, Sicotte NL, Mazziotta JC (1998). Automated image registration: II. intersubject validation of linear and nonlinear models. *J Comput Assist Tomogr* 22:153–165.
- [Xia94] Xia Y, Farquhar T, Burton-Wurster N, Ray E, Jelinski LW (1994). Diffusion and relaxation mapping of cartilage-bone plugs and excised disks using microscopic magnetic resonance imaging. *Magn Reson Med* 31:273–282.
- [Xia98] Xia Y (1998). Relaxation anisotropy in cartilage by NMR microscopy (muMRI) at 14-microm resolution. *Magn Reson Med* 39:941–949.
- [Xia00] Xia Y (2000). Magic-angle effect in magnetic resonance imaging of articular cartilage: a review. *Invest Radiol* 35:602–621.
- [Xia01] Xia Y, Moody JB, Burton-Wurster N, Lust G (2001). Quantitative in situ correlation between microscopic MRI and polarized light microscopy studies of articular cartilage. *Osteoarthr Cartil* 9:393–406.
- [Yao96] Yao L, Gentili A, Thomas A (1996). Incidental magnetization transfer contrast in fast spin-echo imaging of cartilage. *J Magn Reson Imaging* 6:180–184.

- [Zhang08] Zhang W, Moskowitz RW, Nuki G, Abramson S, Altman RD, Arden N, Bierma-Zeinstra S, Brandt KD, Croft P, Doherty M, Dougados M, Hochberg M, Hunter DJ, Kwoh K, Lohmander LS, Tugwell P (2008). OARSI recommendations for the management of hip and knee osteoarthritis, Part II: OARSI evidence-based, expert consensus guidelines. *Osteoarthritis Cartilage* 16:137–162.

Bibliography

Index of Notation

| Notation | Description | Page List |
|--------------------------------|---|--------------|
| 2D | Two dimensional | 72 |
| 3D | Three dimensional | 6 |
| ACT | Autologous chondrocyte transplantation | 30 |
| ADC | Apparent diffusion coefficient | 33 |
| AP | Anterior-posterior | 62 |
| b | b -value (in s/mm^2) | 34 |
| CC | Cranio-caudal direction | 62 |
| CRLB | Crámer Rao lower bound | 42 |
| CV | Coefficient of variation | 30 |
| dGEMRIC | Delayed Gadolinium enhanced magnetic resonance imaging of the cartilage | 23 |
| DTI | Diffusion tensor imaging | 34 |
| DWI | Diffusion-weighted imaging | 33 |
| EXP | Nonlinear fit method to an exponential function | 42 |
| \mathcal{F} | Fisher information matrix | 94 |
| FA | Fractional anisotropy | 34 |
| ϕ | Phase of the Gaussian white noise | 39 |
| FLASH | Fast low angle shot pulse sequence | 23 |
| FOV | Field of view | 29 |
| GAG | Glycosaminoglycan | 11 |
| γ | Gyromagnetic ratio | 22 |
| $\text{Gd} - \text{DTPA}^{-2}$ | A complex of gadolinium with a chelating agent, diethylenetriamine penta-acetic acid (DTPA) | 21 |
| GE | Gradient echo | 26 |

Index of Notation

| Notation | Description | Page List |
|-----------------------|---|-----------|
| $\mathcal{I}(s)$ | Integral for the information matrix | 94 |
| IKDC | International knee documentation committee | 7 |
| I_ν | Modified Bessel function of the first kind of ν -th order | 39 |
| LR | Left-right direction | 62 |
| LR | Linear least squares regression fit method | 42 |
| MACT | Matrix-associated autologous chondrocyte transplantation | 7 |
| MARE | Maximal registration error | 61 |
| MRE | Mean registration error | 61 |
| MRI | Magnetic resonance imaging | 5 |
| MSME | Multi-slice multi-echo sequence | 28 |
| n | Magnitude of Gaussian white noise | 39 |
| $^{23}\text{Na-MRI}$ | Magnetic resonance imaging of the nucleus ^{23}Na | 22 |
| NCEXP | Nonlinear fit of S_M to a noise-corrected exponential function, Σ_{TE} | 42 |
| \circ | Operation of registration of two datasets | 62 |
| OA | Osteoarthritis | 5 |
| Ω | Overlap volume | 59 |
| $P_\phi(\phi)$ | Probability density function of the phase of noise | 39 |
| PG | Proteoglycan | 10 |
| RF | Radio frequency | 24 |
| ρ | Cophenetic correlation coefficient | 74 |
| $\rho_m(T_2, \sigma)$ | Distribution of the measured T_2 values at a noiselevel of σ | 99 |
| $\rho(T_2^e)$ | Distribution of the exact T_2 values | 98 |
| ROI | Region of interest | 5 |
| S | Noise-free signal intensity | 39 |
| S_0 | Noise-free signal intensity at zero echo time | 39 |
| SAR | Specific absorption rate | 25 |
| SD | Standard deviation | 42 |
| SE | Spin echo | 26 |
| SEM | Scanning electron microscopy | 13 |
| $\Sigma(S, \sigma)$ | Noise-corrected signal intensity | 40 |
| σ | Standard deviation of the noise | 39 |

| Notation | Description | Page List |
|-------------------------|---|-----------|
| $\sigma_{\sigma_{T_2}}$ | Standard deviation of the standard deviation of T_2 | 54 |
| $\sigma_{T_2}(T_2)$ | Standard deviation of T_2 | 79 |
| $\Sigma(\text{TE})$ | Noise-corrected exponential decay | 40 |
| S_M | Measured signal intensity | 39 |
| SNR | Signal to noise ratio | 6 |
| SNR ₀ | Signal to noise ratio measured a zero echo time | 42 |
| SQEXP | Nonlinear fit of $S_M^2 - 2\sigma^2$ to an exponential function | 42 |
| $T_{1\rho}$ | Longitudinal relaxation time in the rotating frame | 21 |
| ΔT_2 | Mean significant T_2 change | 81 |
| δT_2 | Error in T_2 due to the magic-angle effect | 71 |
| $h\Delta T_2 B$ | Averaged mean significant T_2 change | 82 |
| TE | Echo time | 6 |
| TR | Repetition time | 27 |
| TSE | Turbo-spin echo sequence | 23 |
| TSL | Spin lock time | 25 |
| UTE | Ultrashort echo | 36 |
| v | Overlap volume of two voxels | 59 |
| V_{Src} | Volume of the source dataset | 59 |
| V_{Trg} | Volume of the target dataset | 59 |
| $V_{Trg \cap Src}$ | Intersection volume of the target and source datasets | 59 |
| WVF | Water volume fraction | 10 |

Acknowledgments

In the first place I would like to acknowledge Prof. Maximilian Reiser for offering me the possibility to carry out my research at the *Institut für Klinische Radiologie* and for his constant support through the different phases of the development of this PhD thesis. Working at the *Institut für Klinische Radiologie* has always been a source of inspiration and a continuous challenge due to the multidisciplinary nature and the variety of the scientific projects at the department.

I would also like to thank Prof. Peter Jakob of the university of Würzburg for permitting me to carry out several MRI experiments on the articular cartilage (not included in this PhD thesis) at the 17.6-T scanner of the university of Würzburg. I am grateful to Prof. Peter Müller of the *Orthopädische Klinik und Poliklinik* for allowing me to use the clinical data of the MACT patients.

This PhD Thesis had not been possible without the continuous encouragement and support of Priv.-Doz. Christian Glaser, who has introduced me into the research of articular cartilage. The constant scientific interaction about the different aspects of MRI of the cartilage and the collaboration in several projects has not only been reflected in the ideas of this work but also has resulted in a friendly relationship.

Dr. Olaf Dietrich has been my mentor in the world of MRI. His extensive knowledge of magnetic resonance, his impressive professional competence and his extraordinary patience with my deficient English (and German) has left an indelible imprint in this PhD thesis. Even more, Dr. Olaf Dietrich has been an ideal roommate (well Olaf, a very conservative estimation demonstrates that since I am in the hospital we sat face to face for over 7800 hours (325 days)). I would also like to thank Dr. Andrea Baur-Melnyk, whose research project about DWI of the bone marrow was my first contact with MRI.

Working on the department would not be the same without all those persons who have formed part of the physics group (Andi, Herbert, Lucianna, Michi, Michael, Olaf, Steven and Ulrike). The friendly and collaborative atmosphere of the physics group was always an incentive in those days were discouragement seized the spirit. I will never forget the many hours spent at lunch (around 500 hours). I would like to thank specially Andi, Michael, Michi, Olaf and Steven for reading the first draft of this thesis and improving it with their suggestions and comments (obviously I am solely responsible of all errors which may be included in this thesis). At last I would like to thank all the medical doctors with whom I have collaborated, especially Annie Horng.

Although each thesis means a project of life (at least for the years of promotion), this has been accentuated in my case due to the circumstances surrounding my PhD. I left everything in Spain (family, friends, work...) and decided to come to Germany with the firm desire of changing my life and with the expectation of finding a new professional horizon. No matter how difficult sometimes it was, what I have found has greatly exceeded my best expectations. And in this point I do not only mean the professional but also the personal. The valuable friends I have made here, which have

Acknowledgments

accompanied me through all the circumstances of my life in Munich, justify per se the great sacrifices, which suppose to carve a niche for oneself in a foreign country. Especially, I would like to thank Emilio and Berenice for their love and company at the Schellingstr. 96. Mariela, Christian, Anna and Steven have spent with me a lot of enjoyable moments. My friends in Spain (Carlos, Antonio, Rosa, Joaquin (“que veinte años no son nada”)...) gave me examples that for a truly friendship the concepts of distance and time remain alien.

For the last, I have reserved my special thanks to my immediate family. Ana has managed to transform the last months of hard work on this thesis in a very happy time, despite of the distance, my tiredness and my very little free time. To my parents and my little sister I am very grateful for their love and constant support with vitamin J. I would not like to waste the opportunity of recording my great acknowledgment to my parents for all what I am and what they gave me.

Agradecimientos

En primer lugar quiero agradecer al Prof. Maximilian Reiser por darme la oportunidad de desarrollar mi investigación en el *Institut für Klinische Radiologie* y por su constante apoyo a través de las diferentes etapas del desarrollo de esta tesis doctoral. Trabajar en el *Institut für Klinische Radiologie* ha sido siempre una fuente de inspiración y un continuo desafío por la multidisciplinaridad y variedad de los proyectos científicos que se desarrollan en el departamento.

Querría agradecer también al Prof. Peter Jakob de la universidad de Würzburg el haberme permitido desarrollar varios experimentos en el cartílago articular (no incluidos en esta tesis) en el scanner de 17.6 T de la universidad de Würzburg. Estoy agradecido al Prof. Peter Müller del *Orthopädische Klinik und Poliklinik* por permitirme utilizar los datos clínicos de los pacientes de MACT.

Esta tesis doctoral no hubiese sido posible sin el continuo ánimo y apoyo de Priv.-Doz. Christian Glaser, quien me introdujo en la investigación del cartílago articular. La constante interacción científica y la colaboración en diferentes proyectos no sólo ha quedado reflejada en las ideas de esta tesis si no también han resultado en una relación de amistad.

Dr. Olaf Dietrich ha sido mi mentor en el mundo de la resonancia magnética. Su vasto conocimiento de la resonancia magnética, su impresionante competencia laboral y su extraordinaria paciencia con mi deficiente inglés (y alemán) han dejado una huella indeleble en esta tesis doctoral. Más aún, Dr. Olaf Dietrich ha sido un compañero de despacho excelente (bien Olaf, una estimación muy conservadora demuestra que hemos estado sentados cara a cara más de 7 800 horas (325 días)). También quiero agradecer a la Dra. Andrea Baur-Melnyk, cuyo proyecto de investigación sobre la DWI en la médula ósea supuso mi primer contacto con la resonancia magnética.

El trabajo en el departamento no hubiese sido lo mismo sin todas aquellas personas que han formado parte del grupo de física (Andi, Herbert, Lucianna, Michi, Michael, Olaf, Steven and Ulrike). La atmósfera amistosa y de colaboración del grupo de física fue siempre un incentivo en aquellos días que el desánimo se apoderaba del espíritu. Nunca olvidaré las muchas horas pasadas en las comidas (aproximadamente 500 horas). Quiero agradecer especialmente a Andi, Michael, Michi, Olaf y Steven el haber leído el primer borrador de esta tesis y haberla mejorado con sus sugerencias y comentarios (obviamente yo soy el único responsable de todos los errores que puedan contenerse en esta tesis). Por último querría agradecer a todos los médicos que he colaborado durante estos años, especialmente a Annie Horng.

Aunque cada tesis involucra un proyecto de vida (al menos para los años de promoción), ésto se ha visto acentuado en mi caso debido a las circunstancias que han envuelto esta tesis. Hace siete años lo dejé todo en España (familia, amigos, trabajo...) y decidí venir a Alemania con el firme deseo de cambiar mi vida y con la expectativa de encontrar un nuevo horizonte profesional. Por muy difícil que haya resultado a veces, lo que he encontrado supera con creces mis mejores expectativas. Y en

Agradecimientos

este punto no sólo me refiero a lo profesional, sino también a lo personal. Los valiosos amigos que he hecho aquí, que me han acompañado a través de todos los avatares de mi vida en Munich, justifican en sí todos los sacrificios que supone el hacerse un hueco en un país extranjero. Especialmente quiero agradecer a Emilio y Berenice por su amor y compañía en la Schellingstr. 96. Con Mariela, Christian, Anna y Steven he pasado momentos muy agradables. Mis amigos en España (Carlos, Antonio, Rosa, Joaquín (“que veinte años no son nada”)...) me dieron ejemplo de que a una verdadera amistad los conceptos de la distancia y el tiempo le son extraños.

Para lo último reservo mi especial agradecimiento a mi familia más cercana. Ana ha conseguido transformar estos últimos meses de duro trabajo en esta tesis en un tiempo muy feliz, y esto a pesar de la distancia, mi cansancio y mi poco tiempo libre. A mis padres y a mi pequeña hermana les estoy muy agradecidos por su amor y constante suministro de vitamina J. No querría desaprovechar esta oportunidad para dejar constancia escrita de mi gran reconocimiento a mis padres por todo lo que soy y lo que me han dado.

Lebenslauf

Name und Familienname: **José Raya García del Olmo**
Geburtsort und Geburtsdatum: 24.01.1972 in Seville, Spanien
Staatsangehörigkeit: Spanisch

Ausbildung

10.1989 - 10.1992 Studium der Physik an der „Universidad de Sevilla“
10.1992 - 10.1995 Studium der Physik an der „Universidad Autónoma de Madrid“ (UAM). Hauptfach Theoretische Physik.
02.1996 - 07.1997 “Estudios de doctorado” (äquivlanet zum deutschen Diplom Phys.) an der UAM. Hauptfach Theoretische Physik.
02.2002 - 12.2002 Deutsche Sprachprüfung für Hochschulzugang ausländischer Studienbewerber (DSH) an der Ludwig-Maximilians Universität.
10.2003 - 09.2005 Fernstudium „Medizinische Physik und Technik“ an der Universität Kaiserslautern (Kaiserslautern, Deutschland).

Beruf

07.1994 - 09.1994 Sommerstipendium an der „Instituto de Astrofísica de Canarias“ (La Laguna, Tenerife). Aufgabe: Turbulenz Simulator.
11.1994 - 06.1995 Stipendium an der Departamento de Física Teórica der UAM. Thema: Yang-Mills Feldtheorie
12.1995 - 05.1997 Doktorand am „Instituto de Matemáticas y Física Fundamental (IMAFF)“ (Madrid, Spanien). Thema: Quantengravitation
05.1997 - 04.2000 Doktorand Stipendium am „Instituto de Astrofísica de Andalucía“ (Granada, Sapnien). Thema: Quantengravitation
03.2000 - 12.2001 Nachhilfelehrer der Physik und Mathematik (Granada, Spanien)
06.2002 - 07.2003 Mitarbeiter bei City FTB GmbH
seit 08.2003 Doktorand am Institut für Klinische Radiologie Ludwig-Maximillian-Universität München.
02.2006 - 07.2007 Lehrer an der Staatlichen Berufsfachschule für medizinisch-technische Radiologieassistenten (München).